Order Number 9405602

Multielemental analyses of environmental and geological samples by inductively coupled plasma mass spectrometry

Wu, Xiaowen, Ph.D.

City University of New York, 1993

U·M·I
300 N. Zeeb Rd.
Ann Arbor, MI 48106

A

Multielemental Analyses of Environmental and Geological Samples

By

Inductively Coupled Plasma Mass Spectrometry

By

Xiaowen Wu

A dissertation submitted to the Graduate Faculty in
Chemistry in partial fulfillment of the requirements
for the degree of Doctor of Philosophy,
The City University of New York.

1993

This manuscript has been read and accepted for the Graduate Faculty in Chemistry in satisfaction of the dissertation requirement for the degree of Doctor of Philosophy.

31 August 1993
date

Evan T. Williams
Chairman of Examining Committee

August 31, 1993
date

Richard D. Pizer
Executive Officer

Eugene S. Hall
Orest Pizer
David C. Locke
Supervisory Committee

The City University of New York

Abstract

Multielemental Analyses of Environmental and Geological Samples

By

Inductively Coupled Plasma Mass Spectrometry

By

Xiaowen Wu

Advisor: Dean Evan T. Williams and Professor Eugene S. Hall

The technique of inductively coupled plasma-mass spectrometry (ICP-MS) has been applied to determine trace elements in environmental (drinking water and tree rings) and geological (soil) samples. Most of this monograph is focused on analysis in these samples of rare-earth elements and lead, which have lower detection limits in ICP-MS than in other analytical techniques.

A brief history of ICP-MS and discussions of fundamental principles of the instrument, interferences of the method, and common analytical protocols are provided. The application of the technique to four projects is described:

1) Quantitative analysis of rare-earth elements in individual tree rings of fire-scarred trees was performed. The result showed that the concentrations of La, Pr, and Nd are highest in the ring corresponding to the fire year.

2) Lead pollution in drinking water from New York City was investigated by measuring lead concentration and the isotope ratio of $^{206}Pb/^{207}Pb$ in drinking water samples and in the suspected polluting sources. It was found that lead in drinking water mainly comes from lead pipe and plumbing materials containing high concentrations of lead. In addition, optimization of

the operating parameters and enhancement of lead signal were also discussed in the chapter.

3) Lead concentration in soil and in annual-growth rings of trees from streets in Brooklyn, New York were analyzed. The change of lead concentration in the rings from 1952 to 1991 correlates with the consumption of lead in gasoline in the United States during the same period. The study showed that tree rings can be used as an indirect historical indicator of environmental changes during the tree's lifetime.

4) Rare-earth-element ratios in archaeological tree samples were measured to determine the original locations of the samples.

In Appendix I, application of proton induced X-ray emission (PIXE) to analysis of wood samples is briefly discussed.

DEDICATED

TO

MY DAUGHTER CHERYL

Acknowledgments

Six years of studies and work eventually resulted in completing this thesis though I experienced a change of research project due to the shutdown of the Brooklyn College accelerator. I would like to take this opportunity to express my sincere gratitude to the people who helped and supported me.

I greatly acknowledge my mentor Dean Evan T. Williams for his guidance, encouragement, supports, kindness, and responsibility throughout my graduate career. Special thanks to my other mentor Professor Eugene S. Hall who guided me to complete most of my experiments using ICP-MS, and trained me in use of computer programs. In addition, his friendship, kindness, and help in many other ways will always be remembered. I would like to thank Professors David Locke and Orest Popovych for their interest in my project and for serving on my thesis committee.

The partial financial support provided by a grant from the New Jersey Department of Environmental Protection and Energy (NJDEPE) is gratefully acknowledged.

I also wish to express my appreciation to Dr. Dong Yan for their collaboration and computer expertise in PIXE laboratory. Thanks to Mr. Zuopeng Wang for helping me to collect water samples, and to Dr. Jinan Wu for performing data analysis for me.

I never forget uncle Fook H. Eng and aunt Jeanna W. Eng who brought me to the United States and supported me during my graduate study. I am grateful to my cousin Billy Lee who spent a lot of time to plot many graphs used in my thesis. The encouragement and support of other uncles, aunts and cousins of Eng's (Wu's) family especially uncle King Chow Lee and aunt Chin Huan Lee are also appreciated.

Finally, I greatly acknowledge my parents and brothers for their invaluable support through the years.

Table of contents

List of Tables

List of figures

Chapter 1 Introduction to inductively coupled plasma mass spectrometry

1.1 Mass spectrometry

Positively charged electrical particles were discovered by E. Goldstein in 1886 [1], when he observed that an electrical discharge at low pressures caused a slightly divergent discharge to stream through the openings in a perforated cathode. Later, W. Wien [2] showed that the rays of Goldstein were deflected in a magnetic field and then established that these rays carried a positive electrical charge. These observations led J. J. Thomson, Nobel Laureate of 1906 and the father of mass spectroscopy, to obtain the first mass spectrum [3]. Upon introducing $COCl_2$ and hydrocarbons into the discharge tube and using Faraday cup as detector, Thomson [3] measured the currents of positively charged fragments as a function of the mass-to-charge (m/e) ratio. Thomson [4] also discovered that neon consisted of a mixture of two different isotopes, ^{20}Ne and ^{22}Ne, rather than only a single isotope (later studies showed that there are three stable isotopes of neon). Since Thomson's early work many other isotopes have been discovered and studied by mass spectroscopy. Aston became the Nobel Laureate for obtaining mass spectra of isotopes of most elements.

By 1920, the early mass spectrometers were capable of three types of measurements: a) precise mass determinations, b) measurement of relative abundances of ions, and c) electron impact studies. After 1920, the application of the mass spectrometer was extended to separation of isotopes and studies of free radicals. Smythe *et al.* [5] separated and concentrated the anode rays of potassium, obtaining as much as 1 mg of ^{39}K. The very

significant success of the separation and isolation of ^{235}U and ^{238}U in detectable quantities was achieved by A. O. Nier *et al.* [6] in 1940. In 1943, J. A. Hipple and D. P. Stevenson [7] made the first satisfactory direct determination of the ionization potentials of the free radicals.

Although the first mass spectrum was obtained as early as 1912, the technique of mass spectroscopy was not fully realized and taken advantage of in analytical chemistry until 1940 when Hoover and Washburn [8] published the first paper of mass spectrometric hydrocarbon analysis. Nowadays, in the field of analytical chemistry, mass spectroscopy has been used to:

i) identify the structures of organic compounds;

ii) quantitatively analyze organic multi-component mixtures;

iii) qualitatively and quantitatively analyze for multiple elements in inorganic and/or organic samples;

iv) accurately determine isotope ratios of most elements in periodic table.

The development of mass spectrometric instruments experienced several steps. Thomson's parabola mass spectrograph can be thought as the first generation of mass spectrometers though it only had a resolving power of 15. In 1918, Dempster [9] developed the direct-focusing analyzer increasing the resolving power up to 100. Later, Dempster built a double-focusing mass spectrometer with the resolving power of 7000. Other types of analyzers after 1918 included velocity-focusing, RF time-of-flight, pulsed time-of-flight (see reference 10). The mass spectrometers described above were very bulky and expensive because the instruments contained magnets and power supplies for deflection of charged particles. The breakthrough in analyzer type came in 1953 when Paul and coworkers [11,12] developed a quadrupole mass spectrometer. The magnet was eliminated from the quadrupole

analyzer. This allowed not only a significant decrease in weight and size, but also faster scanning of the mass region. Quadrupole mass spectrometry has had a wonderful career since it was initiated by Paul and coworkers. Combined with gas chromatography (GC) or inductively-coupled plasma (ICP) for sample introduction, the GC-MS and ICP-MS systems have become the most powerful analytical tools in organic and inorganic chemistry.

1.2 Inductively coupled plasma (ICP)

The study and development of ICPs dates back to 1942 when G. Baba first succeeded in sustaining induction heated plasmas at atmospheric pressure [13,14]. In 1960, T. B. Reed described some exceptionally effective ways of forming and stabilizing Ar-supported inductively-coupled plasma [15]. The importance of Reed's plasma torch was recognized by Fassel *et al.* in the United States and Greenfield *et al.* in England. They first studied ICP as an analytical emission source independently in 1962, the first results of which were communicated in 1964 [16] and 1965 [17]. The landmark of ICP as a novel analytical tool was established in 1969 when Fassel *et al.* [18] succeeded in lowering the detection limits to the 0.1-10 ng/ml range for many elements, using ICP as excitation source for AES (atomic emission spectroscopy). Instrument manufacturers had become gradually aware of the potentialities of ICP-AES and thus 1974 saw the first modern commercial ICP instrument [19].

The major advantages of ICPs as excitation sources compared to flame for analytical atomic spectroscopy, as described by Fassel, are: a) relatively long-residence time of sample in the plasma; b) higher temperature than

combustion flames; and c) absence of electrode contamination.

1.3 Inductively-coupled plasma mass spectrometry

The idea of analysis of chemicals by "plasma mass spectrometer" was proposed by O'Halloran *et al.* [21] in 1964 when they analyzed both neutral and ionic species in a d.c. plasma jet, using a time-of-flight mass spectrometer. In the conclusions of the 1964 paper, O'Halloran *et al.* suggested to add reactive chemicals to the plasma for analysis of reaction processes by the plasma mass spectrometer, but not as a means of analysis of the added species.

The first evaluation of a small d.c. capillary-arc plasma (CAP) as ion source for a mass spectrometer system to analyze trace elements was made by Gray in 1971 [22]. A small fraction of d.c. plasma along with its ions was extracted through a sampling orifice of diameter from 75-125 μm into a vacuum system containing an electrostatic ion lens, quadrupole mass analyzer, and electron multiplier. Detection limits of 0.02-30 ng/ml were obtained. Although matrix and interelement interferences were severe [23], these results indicated the feasibility of obtaining elemental mass spectra from analytes in solution with a plasma ion source.

In about the same year when Gray's CAP paper was published, the ICP was also developed for trace-element determinations by atomic emission spectrometry (AAS). After surveying the characteristics of the ICP and CAP, Gray *et al.* [26] found that in CAP the ionization temperature was too low to provide adequate ionization of elements whose ionization energy was greater than 8 eV and severe ionization suppression was caused by low ionization energy species. It was therefore proposed to substitute an ICP for the CAP as

an ion source for mass spectrometry. Then Gray *et al.* in United Kingdom and Houk *et al.* at Ames laboratory, Iowa State Uninversity started their developments in ICP-MS independently and then cooperatively [26]. Houk *et al.* obtained the first analytical mass spectra from an ICP in 1978 [20], followed not long after by the successful operation of the updated system in the UK with an ICP [24, 25]. The detection limits of ICP-MS for most elements reported by Gray were 0.02-0.7 ng/ml (3σ) [26].

Since the first commercial ICP-MS instrument (Sciex Ltd) was introduced to the analytical community in 1983 [26], the technique has gained rapid and wide acceptance in many analytical laboratories.

ICP-MS is becoming a valuable instrumental method for elemental analysis because of its attributes [30], including:

a) rapid, simultaneous, multielemental analysis;

b) simple spectra (compared with ICP-AES);

c) low detection limits (part per billion or part per trillion for some elements);

d) wide linear dynamic range (up to 6 orders of magnitude);

e) high precision;

f) isotope-ratio capability.

The most commonly used techniques for elemental analysis include flame atomic absorption spectrometry (FAAS), X-ray fluorescence (XRF), graphite furnace atomic absorption spectrometry (GFAAS), and inductively coupled plasma atomic emission spectrometry (ICP-AES). Neutron activation analysis (NAA) is a high sensitive technique for elemental analysis, but it is not used as so often as the instruments mentioned above. The first, and most widely used technique, flame atomic absorption spectrometry, is basically a single-element technique with μg/g (ppm) sensitivity. It suffers from serious matrix interferences and only when used with graphite-furnace atomization

does it compete with the ng/g (ppb) sensitivity of NAA. The multi-element capability of NAA is offset by the need for sophisticated equipment (reactor) and the long analysis time. Although ICP-AES is capable of multi-elemental analysis, it lacks heavy-element sensitivity. The shortcomings of the above techniques can be overcome by ICP-MS.

Comparison of some capabilities and detection limits among ICP-MS, ICP-AES, and GFAAS are shown in Table 1.1 and Table 1.2, respectively.

According to Table 1.2, the detection limits of ICP-MS are comparable to those of GFAAS; for heavy mass elements, the detection limits of ICP-MS are 2 to 3 orders of magnitude superior to those of ICP-AES.

Since the main advantages of ICP-MS as a method for elemental analysis are its multi-element and isotope-ratio capabilities, sensitivity, and speed, this technique was best suited for my research which focused on the determination of trace-element concentrations and isotope ratios in the following environmental samples: 1) annual-growth rings of trees, 2) soils, and 3) drinking water.

Table 1.1 General figures of merit for ICP-MS, ICP-AES, and GFAAS.

	ICP-MS	ICP-AES	GFAAS
sample introduction	solution, solid[a]	solution	solution
sample size	10 ml[b]	10 ml[b]	20μl
multielement analysis	yes	yes	limited
isotope-ratio capability	yes	no	no
precision	0.5%-5%	1%-5%	1%-5%
matrix interferences	severe	less severe	less severe

a --- with laser ablation as sample introduction system.

b --- pneumatic nebulizer.

Table 1.2 Comparison of detection limits (3σ blank, pg/g, parts per trillion).

Atomic number	Element	ICP-MS[a]	ICP-AES[b]	GFAAS[b]
12	Mg	540	100	10
13	Al	150	1500	250
23	V	15	2000	1100
24	Cr	140	4000	75
25	Mn	19	300	30
26	Fe	1890	1500	60
27	Co	31	5000	210
28	Ni	100	5500	240
29	Cu	61	2000	300
30	Zn	94	900	8
31	Ga	7	6500	230
33	As	74	12000	500
34	Se	2410	37000	700
37	Rb	11	3000	50
38	Sr	4	20	100
48	Cd	19	1500	10
49	In	100	18000	350
56	Ba	5	70	850
57	La	1	20	----
58	Ce	2	7500	----
59	Pr	3	800	----
60	Nd	6	2000	----
62	Sm	9	7000	----
63	Eu	2	300	----
64	Gd	6	2500	----
65	Tb	2	5000	180
66	Dy	4	300	2300
67	Ho	2	500	----
68	Er	5	700	5000
69	Tm	2	1500	----
70	Yb	3	300	150
71	Lu	2	50	----
81	Tl	3	16000	750
82	Pb	20	14000	280
90	Th	6	17000	----
92	U	5	18000	----

a --- values were from our laboratory.

b --- these values were from Varian Guide to ICP/AAS Analytical Values.

Chapter 2 Theories of ionization and mass analysis in ICP-MS

The basics of the ICP-MS technique are that the sample to be analyzed is ionized in an inductively-coupled plasma and the ions formed in the plasma are extracted into a quadrupole mass analyzer by an ion lens bearing negative voltage and then detected by a electron multiplier sequentially.

2.1 The ICP as an ion source

There are various plasma sources used for elemental analysis [31]. Among these sources, the ICP appears to be the primary source for that purpose. One of the reasons for the choice of ICP as ion source is that the temperature in ICP is very high (up to 10,000 K) and because of that, most elements are ionized completely.

In the plasma, analyte species experience dissociation, atomization, excitation and ionization. The last step is a very important step which affects the sensitivity of the technique. The possible ionization processes in ICP are shown in Table 2.1. The major ionization mode in ICP is likely to be electron impact since electron density in ICP is about 3×10^{15} cm^{-3} [32]. Charge transfer may also play a significant role in the ionization of neutral elements. The effect of charge transfer will be discussed in Chapter 7.

The ionization efficiency of the analyte species depends on the temperature in the plasma and the ionization energy of the species. It can be estimated from the Saha equation [31] shown below:

$$\frac{N_{ij} \times N_e}{N_{aj}} = \frac{(2\pi M_e k T)^{3/2}}{h^3} \times \frac{2 Z_{ij}}{Z_{aj}} e^{-\varepsilon_j/kT} \qquad (2.1)$$

where : N_{ij} is the ion concentration of species j;

N_{aj} is the atom concentration of species j;

N_e is the free electron concentration;

k is Boltzman's constant;

h is Planck's constant;

M_e is rest mass of electron;

Z_{ij} is the partition function of ions of species j;

Z_{aj} is the partition function of atoms of species j;

T is the ionization temperature;

ε is ionization energy of atoms of species j.

The degree of ionization (α) of a species is defined by the ratio of the ion population N_{ij} to the total population of the species:

$$\alpha_j = \frac{N_{ij}}{N_{ij} + N_{aj}} \qquad (2.2)$$

Substituting equation (2.2) into equation (2.1) and rearranging it, we obtain

$$\frac{\alpha_j}{1 - \alpha_j} = \frac{(2\pi M_e kT)^{3/2}}{N_e h^3} \times \frac{2Z_{ij}}{Z_{aj}} e^{-\varepsilon_j/kT} \qquad (2.3)$$

The electronic partition function $Z_j(T)$ is calculated from the expression [33]:

Table 2.1 Ionization Processes in the ICP.

I. Primary Ionization Processes#

A. Electron impact

$$M^0 + e^- \longrightarrow M^+ + 2e^-$$

B. Penning ionization

$$M^0 + Ar^* \longrightarrow M^+ + Ar^0 + e^-$$

II. Secondary Ionization Processes

A. Charge transfer

1. Nonsymmetric

$$Ar^+ + M^0 \longrightarrow M^+ + Ar^0$$

$$ArO^+ + M^0 \longrightarrow M^+ + ArO^0$$

$$NO^+ + M^0 \longrightarrow M^+ + NO^0$$

2. Dissociative

$$Ar^* + MO \longrightarrow M^+ + O + Ar^0$$

B. Associative Ionization

$$Ar^* + M \longrightarrow ArM^+ + e^-$$

C. Photoionization

$$M^* + h\upsilon \longrightarrow M^+ + e^-$$

M^0 = neutral element; $*$ = excited state.

$$Z_j(T) = a + b(T/10^3) + c(T/10^3)^2 + d(T/10^3)^3 + e(T/10^3)^4 + f(T/10^3)^5 \qquad (2.4)$$

where a, b, c, d, e, and f are values of polynomial coefficients for atoms and ions.

It has been reported that the value of N_e is about 3×10^{15} cm^{-3} at 10 mm beyond the load coil [32], and the value of T is about 8000 K for a 1200 W ICP ion source [34]. In our laboratory, the sampling cone is 12mm beyond the load coil and the forward RF power (see Chapter 3) is 1350 W. So the values of α_j can be calculated assuming that $N_e = 1\times10^{15}$ cm^{-3} and T = 7500 K. Other parameters in equations (2.3) and (2.4) are available in the literature [33, 35]. The results of the calculations along with ionization energy of some elements are shown in Table 2.2. From this compilation it is apparent that formation of singly charged ions is very efficient in the ICP. Some 40 elements are expected to be ionized with an efficiency of 90% or more. Actually, more than 54 elements in the periodic table have ionization efficiencies greater than 90%. Since the coefficients in equation (2.4) for Th, U, and rare earth elements are not available to the writer, the degrees of ionization for these elements are not listed in Table 2.2. The degree of ionization for Th, U, and rare earth elements at T = 7500 K and $N_e=1\times10^{15}$ cm^{-3} are between 90% and 100% (see ref. 36). Theoretically, most elements from Li to U can be analyzed by ICP-MS except those elements which have very low ionization efficiency in the ICP and those which are short-lived radioisotopes. Moreover, carbon, oxygen, and nitrogen cannot be analyzed by ICP-MS because either aqueous solutions or the atmosphere contain these elements thus making the background signals of those elements very high.

Equation (2.3) shows that the degree of ionization for a element is a function of ionization energy of the element. The general form of the dependence of the degree of ionization on ionization energy for singly charged

Table 2.2 First and second ionization energy[a] (eV) of 67 elements and calculated degree of ionization (α, %) of M^+ at T_i = 7500 K, $N_e = 1\times10^{15}cm^{-3}$.

Z	element	1st ionization energy	2nd ionization energy	α
2	He	24.59	54.52	2E-8
3	Li	5.39	75.64	99.7
4	Be	9.32	18.21	75.0
5	B	8.30	25.15	58.0
6	C	11.26	24.38	5.0
7	N	14.53	29.60	0.1
8	O	13.62	35.12	0.1
9	F	17.42	34.97	9E-4
10	Ne	21.56	40.96	6E-6
11	Na	5.140	47.29	99.8
12	Mg	7.65	15.04	97.6
13	Al	5.99	18.83	98.0
14	Si	8.15	16.35	85.4
15	P	10.49	19.73	33.1
16	S	10.36	23.33	14.3
17	Cl	12.97	23.81	0.9
18	Ar	15.76	27.63	0.05
19	K	4.34	31.63	99.9
20	Ca	6.11	11.87	99.7
21	Sc	6.54	12.80	99.2
22	Ti	6.82	13.58	99.1
23	V	6.74	14.65	98.8
24	Cr	6.77	16.50	98.2
25	Mn	7.44	15.64	95.3
26	Fe	7.87	16.18	95.7
27	Co	7.86	17.06	93.4
28	Ni	7.64	18.17	90.8
29	Cu	7.73	20.29	89.2
30	Zn	9.39	17.96	75.3
31	Ga	6.00	20.51	98.2
32	Ge	7.90	15.93	89.5
33	As	9.81	18.63	51.6
34	Se	9.75	21.19	33.3
35	Br	11.81	21.80	5.3

a — The values of ionization energies are from reference 35.

Table 2.2 First and second ionization energy (eV) of 67 elements and calculated degree of ionization (α, %) of M^+ at T_i=7500 K, $N_e=1\times10^{15}$ cm^{-3} (continued).

Z	element	1st ionization energy	2nd ionization energy	α
36	Kr	14.00	24.36	0.6
37	Rb	4.18	27.28	99.9
38	Sr	5.70	11.03	99.8
39	Y	6.38	12.24	97.7
40	Zr	6.84	13.13	98.8
41	Nb	6.88	14.32	98.4
42	Mo	7.10	16.15	97.8
43	Tc	7.28	15.26	96.3
44	Ru	7.37	16.76	95.7
45	Rh	7.46	18.08	94.5
46	Pd	8.34	19.43	92.6
47	Ag	7.58	21.49	92.6
48	Cd	8.99	16.91	85.0
49	In	5.79	18.87	98.9
50	Sn	7.34	14.63	95.4
51	Sb	8.64	16.53	80.0
52	Te	9.01	18.60	66.4
53	I	10.45	19.13	29.8
54	Xe	12.13	21.21	8.6
55	Cs	3.89	25.10	99.9
56	Ba	5.21	10.00	99.9
57	La	5.58	11.06	99.8
72	Hf	7.00	14.90	98.4
73	Ta	7.89	-----	94.8
74	W	7.98	-----	93.6
75	Re	7.88	-----	92.7
76	Os	8.7	-----	77.9
78	Pt	9	18.56	63.4
79	Au	9.23	20.50	50.7
80	Hg	10.44	18.76	37.8
81	Tl	6.11	20.43	98.8
82	Pb	7.42	15.03	96.9
83	Bi	7.29	16.69	92.3

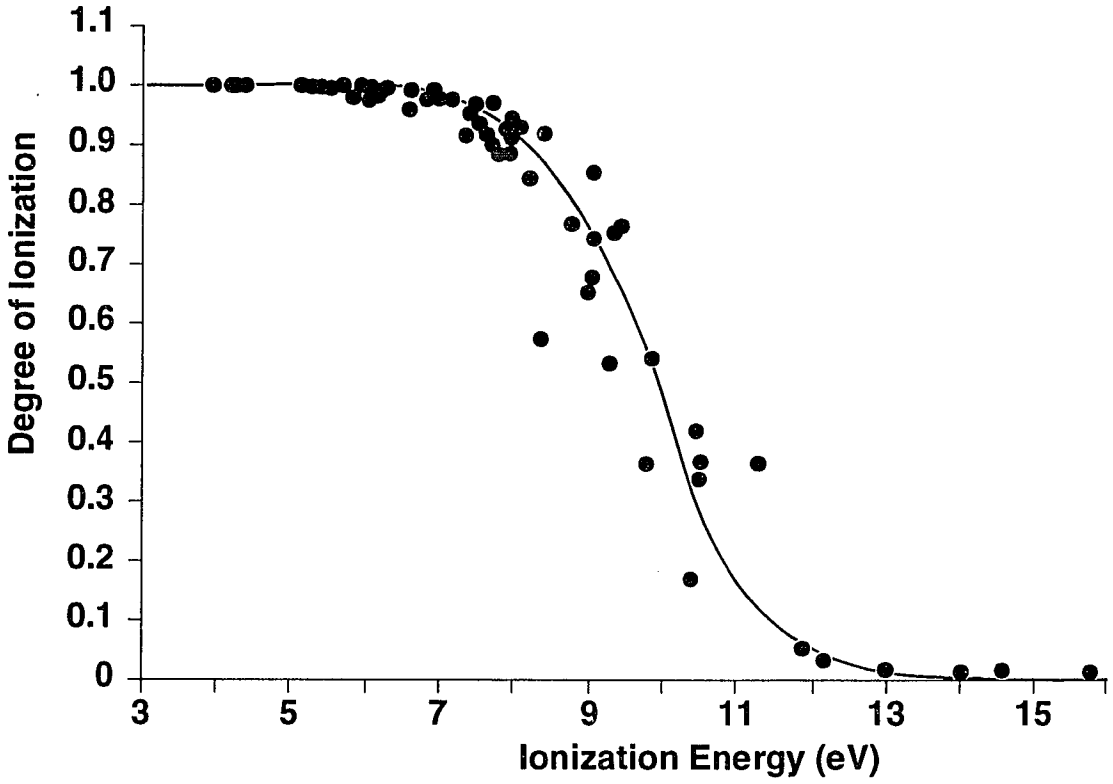

Figure 2.1 Degree of ionization versus ionization energy for singly charged ions in the ICP (from reference 40).

ions is shown in Figure 2.1, from which it may be seen that the response falls away rapidly above 9 eV. As will be seen from Table 2.2 most elements have first ionization energies below 10 eV, corresponding to greater than 50% ionization while there are none whose second ionization energies fall below 10 eV. Thus, although there are a number of elements such Ba and rare earths which undergo some double charge ionization, the majority do not and doubly charged ions (α is only 2% to 10% for M^{2+}) do not present serious problems.

2.2 Quadrupole mass spectrometer

A mass spectrometer operates by causing ions of different mass-to-charge ratio (m/z) to follow different spatial trajectories by the application of electromagnetic fields. There are several methods which can be employed to perform this operation [37]. Often, a magnetic field is used to deflect ions by an amount proportional to their m/z ratio or, more correctly, to their momentum.

The heart of the mass spectrometer is the mass analyzer. Many modern mass spectrometers commercially available employ a quadrupole mass analyzer as mass filter [38]. A diagram of a typical quadrupole mass analyzer is shown in Figure 2.2. Four straight metal rods or metallised surfaces are suspended parallel to and equidistant from the axis. Ideally, the geometry of the rods should be hyperbolic in cross section, but in practice, for ease of manufacture, round cylindrical rods are employed, with the spacing optimized to approximate the ideal electric field [39]. Opposite pairs are connected together. Direct current (DC) and radio frequency (RF) voltages of amplitude U and V, respectively, are applied to each pair. As shown in

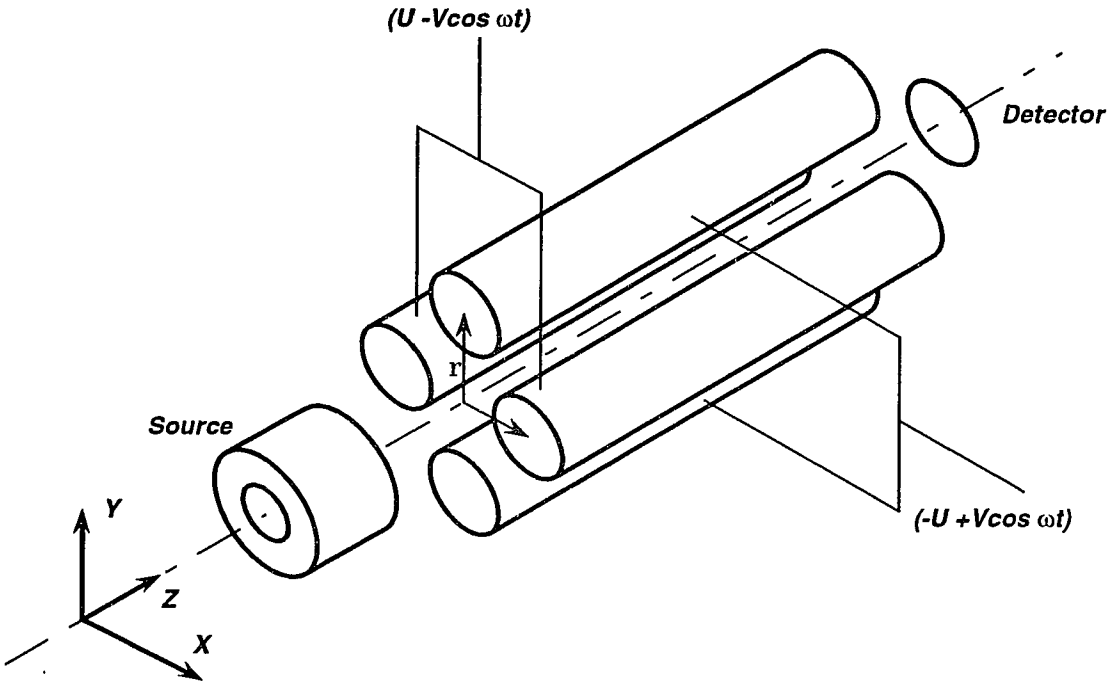

Figure 2.2 Schematic arrangement of the quadrupole mass filter.

Figure 2.2, the DC voltage is positive for one pair and negative for the other pair. The RF voltages on each pair have the same amplitude but are opposite in sign, i.e. they are 180^0 out of phase.

The potential ϕ at any point (x, y, z) in the field is expressed by [38]:

$$\phi = \frac{x^2 - y^2}{r_o} \times (U - V\cos\omega t) \tag{2.5}$$

where r_0 is the inscribed radius between rods and ω is the angular frequency of RF voltage.

Ions are injected from the plasma into the electric field in the z direction. According to Dawson [38] the motions of the ions are described by the following equation:

$$\frac{d^2x}{dt^2} + \frac{2e}{mr_o} \times (U - V\cos\omega t)x = 0 \tag{2.6}$$

$$\frac{d^2y}{dt^2} - \frac{2e}{mr_o} \times (U - V\cos\omega t)y = 0 \tag{2.7}$$

$$\frac{d^2z}{dt^2} = 0 \tag{2.8}$$

The differential equations (2.6) and (2.7) are of a form known as Mathieu equations. The solutions are usually divergent. This corresponds to rejection of ions from the filter. Stable solutions, corresponding to transmission of ions by the filter are obtained only for certain values of m, $r_{o,}$, f, U, V. Equation

(2.8) indicates that there is no acceleration along the z axis, and so the axial velocity is constant.

By making the substitutions:

$$a = \frac{8eU}{m\omega^2 r_o^2} \tag{2.9}$$

$$q = \frac{4eV}{m\omega^2 r_o^2} \tag{2.10}$$

$$\xi = 2\pi ft \tag{2.11}$$

the equations (2.6) and (2.7) can be written in the form :

$$\frac{d^2u}{d\xi^2} + (a - 2q\cos(2\xi))u = 0 \tag{2.12}$$

The solutions of equation (2.12) are stable only if a and q lie within the area depicted in Figure 2.3. For most values of (a, q), the RF and DC fields displace the ion outside the rod boundaries, where it is lost. Such trajectories are termed unstable ones, because ions on these trajectories have unstable paths. Ions with stable paths are those that stay within the rods; these ions have (a, q) values that fall within the pyramidal enclosure of the stability diagram.

To separate the ions with different m/z values, the scan line shown in Figure 2.4 is superimposed upon the stability diagram. At particular values of U and V, a given point on the scan line corresponds to one particular value of m/z. Thus, as the power supply changes U and V during the scan, a and q

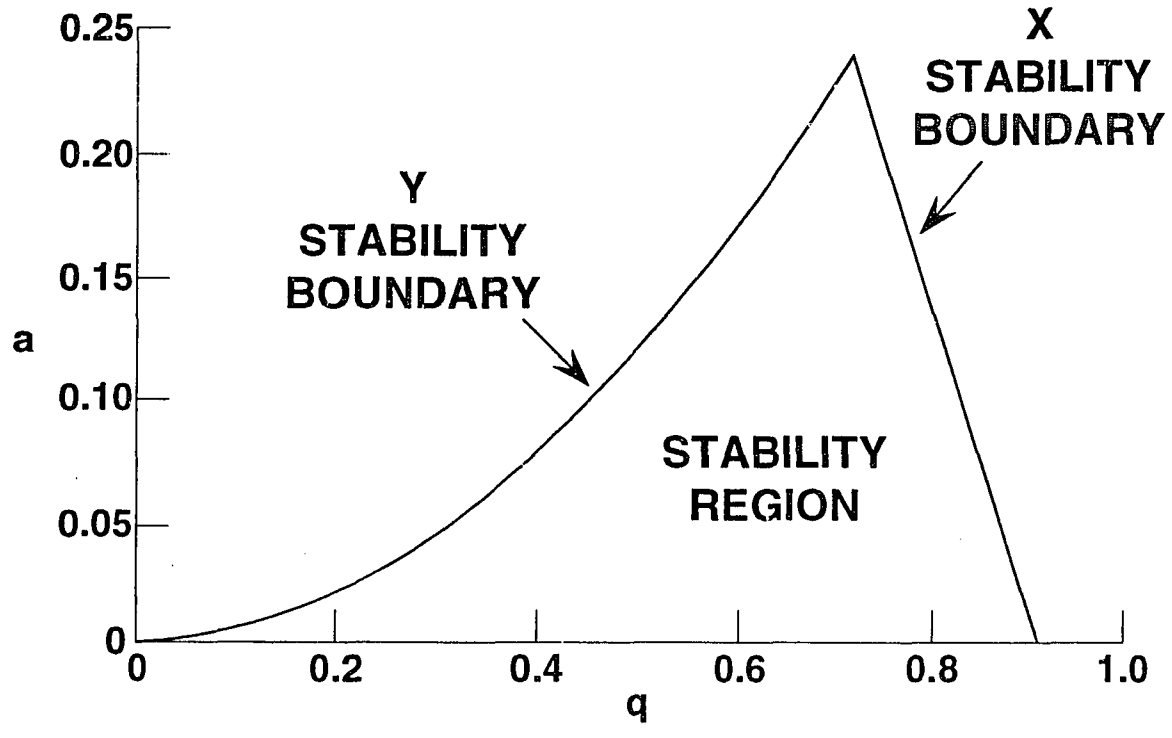

Figure 2.3 Stability diagram (a, q).

change as well, which corresponds to moving from one m/z to another along the scan line. With the scan line present the only ions that have stable paths are those that fall on the scan line and inside the segments which intersect the stability diagram. As shown in Figure 2.4, an ion with m/z = M will have a stable path through the rods if U and V are selected so that the corresponding value (a, q) on the scan line stays under the tip of the stability diagram. At the same values of U and V, neighboring ions at M+1 and M-1 have different (a, q) values that are outside the stable region, so these ions are rejected from the filter and neutralized by the negative charges on the rods. In practice, the ratio of U to V is kept constant while the values of them change with time. As U and V are changed, the operating points for ions of different m/z will move into the stable region, and a mass spectrum can be obtained by varying U and V.

The slope of a scan line affects the resolution and the sensitivity. The scan line "cuts" the stability diagram so as to produce an aperture of sorts. If the ratio U/V is increased, the scan line has a higher slope and passes closer to the tip of the stability diagram. The nearer to the tip the diagram is cut, the smaller the aperture; thus the conditions for ion transmission become more stringent and fewer ions traverse the filter, resulting in higher resolution and lower sensitivity. Conversely, the lower the cut (decrease the slope), the larger the aperture, and many more ions are able to strike the detector; this results in a larger signal at the cost of less stringent criteria for transmission, i.e. lower resolution. The usual compromise between resolution and sensitivity holds for quadrupole mass spectrometers.

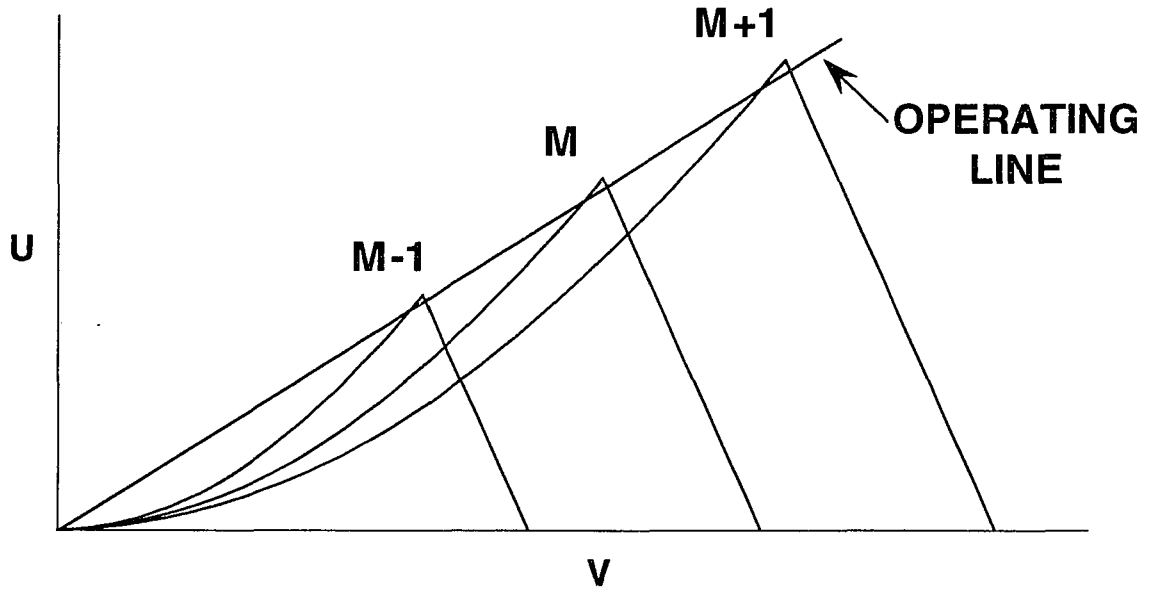

Figure 2.4 Stability diagram for transmission of ions with different m/z values.

Chapter 3 Instrumentation

The ICP-MS instrument used was a VG PlasmaQuad PQ2 Plus (VG-Isotopes, Winsford, UK). The instrument includes: 1) sample introduction system; 2) ionization system; 3) interface between ICP and MS; 4) quadrupole mass analyzer; 5) detection system; and 6) data processing system. Figure 3.1 is the overall systematic diagram of the VG PlasmaQuad.

3.1 Sample introduction

For analysis by ICP-MS, the sample must be in such a form that it can be carried in a stream of gas. In the standard instrument configuration, this involves the generation of a fine aerosol from the sample in solution using a nebulizer and spray chamber mounted within the ICP torch box. The components of the sample introduction system used in our laboratory are the peristaltic pump (Gilson, M312), the nebulizer, and the spray chamber (see Figure 3.2).

The peristaltic pump is used to pump the analyte solution into the spray chamber through the nebulizer, and to remove the waste solution from the spray chamber. The nebulizer used in our instrument is the glass Meinhard dual concentric type. After it is pumped into the nebulizer, the stream of sample solution is disrupted by the high velocity gas flow (Ar carrier gas) to produce a spray of droplets with diameter less than 10 μm. The solution uptake rate can be controlled by adjustment of the pump speed and through choice of pump tubing diameter. It was reported [41] that a decrease in the sample uptake rate at the expense of the sensitivity increases the temperature of the plasma and so decreases the formation of oxides.

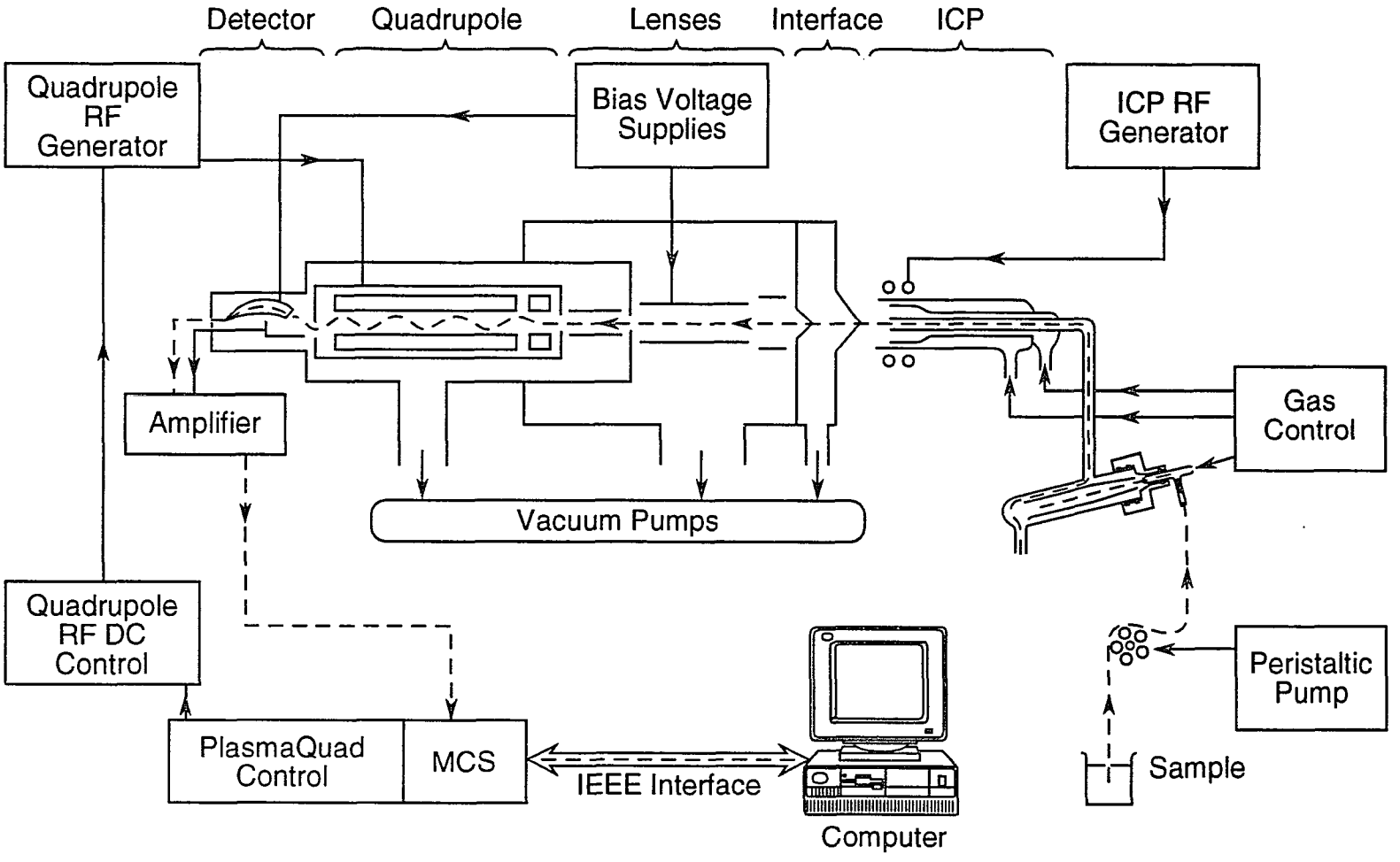

Figure 3.1 The overall systematic diagram of the VG Plasma Quad (from VG PlasmaQuad Operating Manual 1992).

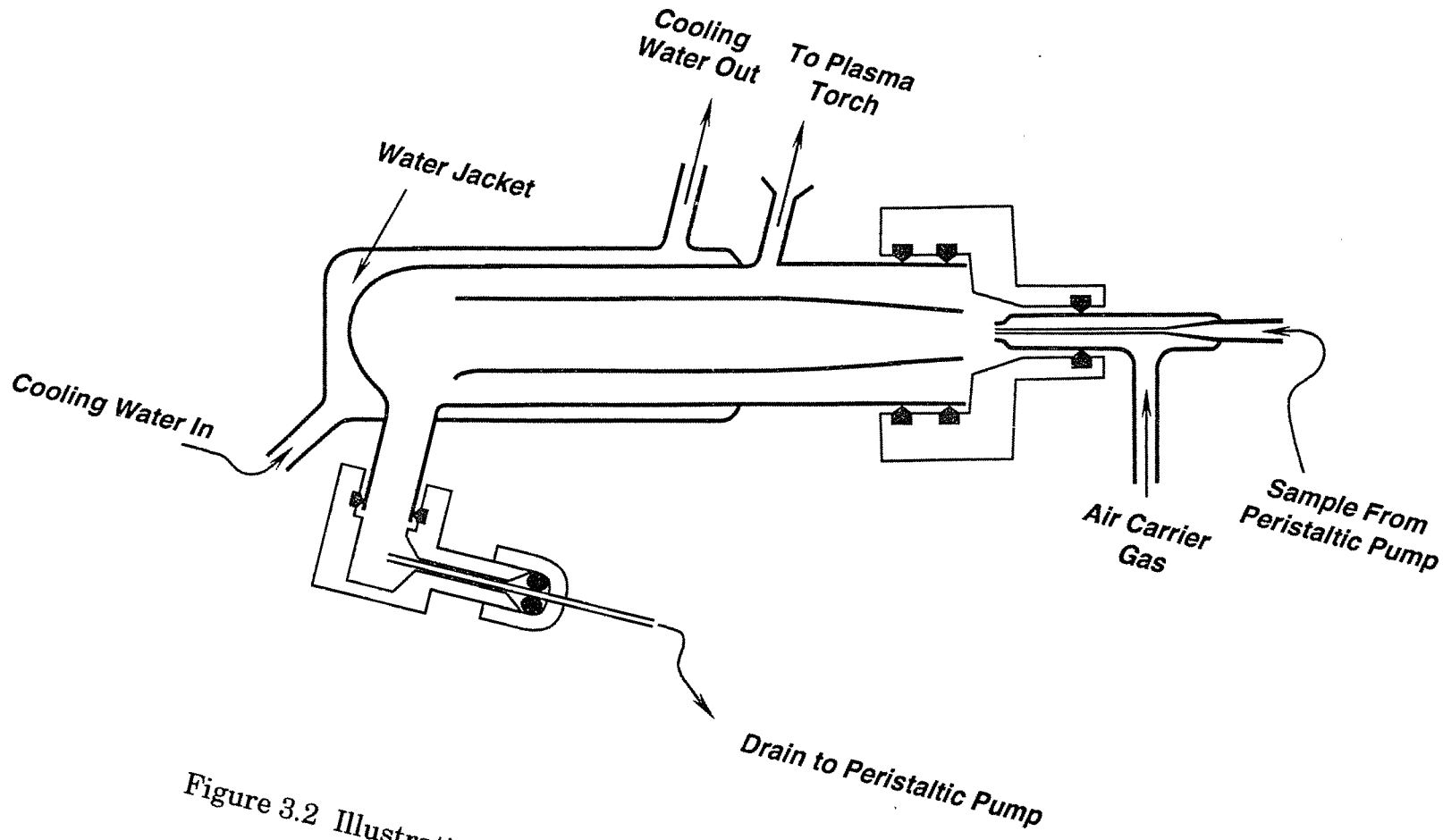

Figure 3.2 Illustration of the spray chamber and the nebulizer.

The spray chamber is a double bypass Scott type made of borosilicate glass. Its purpose is to ensure that only the smallest solution droplets reach the plasma, keeping the loading of the plasma even and preventing the cooling of the plasma. However, the cost of this process is low efficiency, with only around one percent of the sprayed solution being transported to the ICP. Large quantities of oxygen in the plasma, introduced as water in normal solution analysis can form oxides with argon gas, acid solvent, and some analytes, thus causing detrimental effects such as spectral interferences (see Chapter 4 for detail). In order to lower the water loading and so reduce these effects, a cooling water jacket is provided on the spray chamber. When the ICP-MS is operating, the temperature in the spray chamber is kept below 1°C.

Our laboratory employs the pneumatic nebulizer for sample introduction. Other sample introduction methods such as ultrasonic nebulization [42], electrothermal volatilization [43], flow injection [20], laser ablation [44], and direct injection nebulization [27, 28] have been used in ICP-MS.

3.2 The inductively coupled plasma

The ICP is the source of the ions that are subsequently mass analyzed in the PlasmaQuad. A key advantage of the ICP-MS method over other forms of mass spectrometry is that this ion source operates outside the vacuum system, enormously simplifying sample introduction.

The main body of the ICP torch consists of a concentric quartz tube (o.d. = 18 mm in the PlasmaQuad). The tip of the quartz tube is located inside a coaxial water-cooled load coil of three turns, which is connected to a high-frequency generator as illustrated in Figure 3.3. The RF generator is

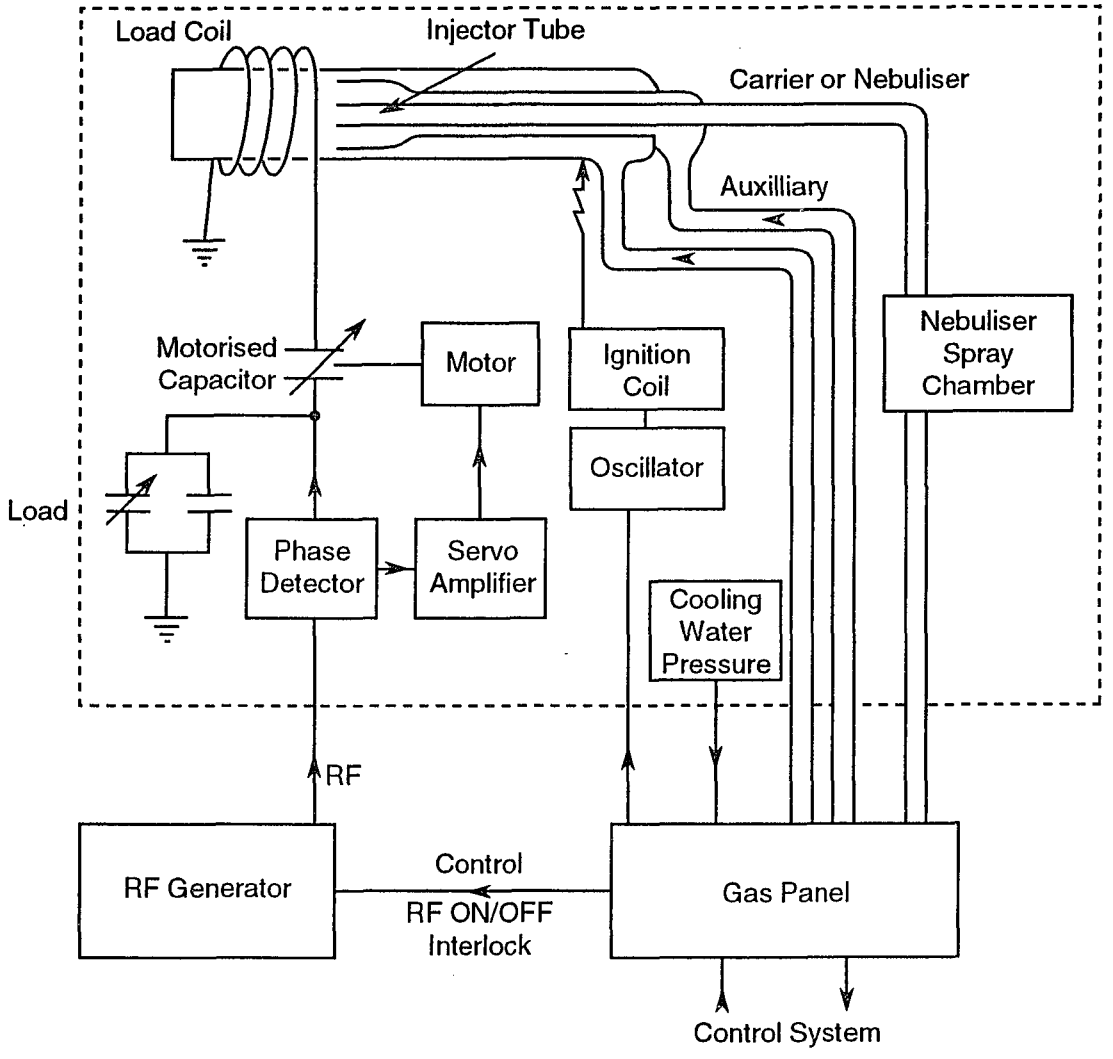

Figure 3.3 The ICP torch (from VG PlasmaQuad Operating Manual 1992).

operated at frequency of 27.12 MHz and at output power up to 2000 W (1350 W commonly used in our experiments). The flow of argon gas acts as the support gas for the plasma and as the coolant for the tube.

To form the plasma, a spark from a Tesla coil is used to produce "seed" electrons and ions in the region of the load coil. The high frequency alternating currents in the load coil generate magnetic fields with their lines of force located parallel to the tube. The seed ions and electrons are accelerated in a circular flow or eddy current (see Figure 3.4). When the AC current in the load coil reverses direction, the magnetic field also reverses. The accelerated ions and electrons collide with argon atoms and cause additional ionization along with intense ohmic heating. Once the Ar conducts, the plasma forms spontaneously if the flow patterns are proper inside the tube.

The frequency of RF generator has a crucial effect on the ionization of samples. If the plasma is operated at low frequencies, e.g. 5 MHz, a plasma shape much like a teardrop is obtained, as shown in Figure 3.5a. The sample particles do not penetrate the high-temperature region (shown by the crosshatching), where the flow resistance due to gas expansion is the highest. Such a shape thus results in inefficient heating of the sample. When operated at high frequencies (about 27 MHz), the plasma assumes an annular or toroidal shape (see Figure 3.5b). Sample particles thus travel through a narrow axial channel surrounded by the high-temperature core. Obviously, the annular plasma obtained at higher frequencies (about 27 MHz), gives rise to efficient desolvation, volatilization, excitation, and ionization of the sample. It is worth noting that the ICP-mass spectrometers made by Perkin Elmer operate at high frequency of 40 MHz.

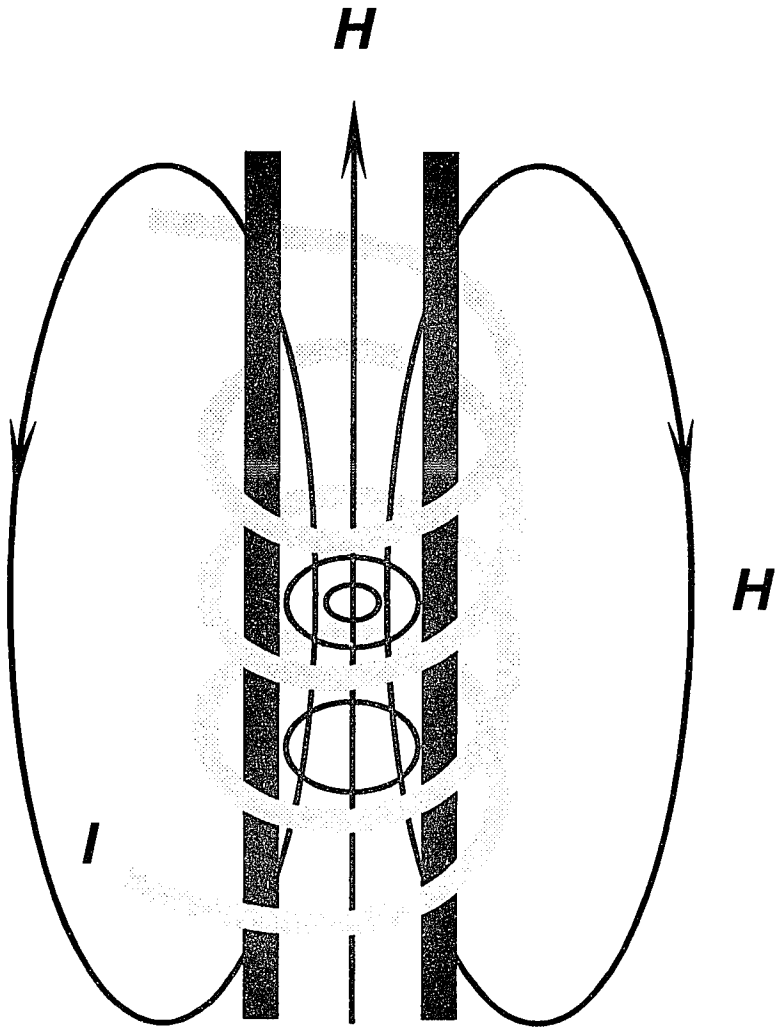

Figure 3.4 The Magnetic fields (H) and eddy currents (I) inside the torch tube (from Reference 31).

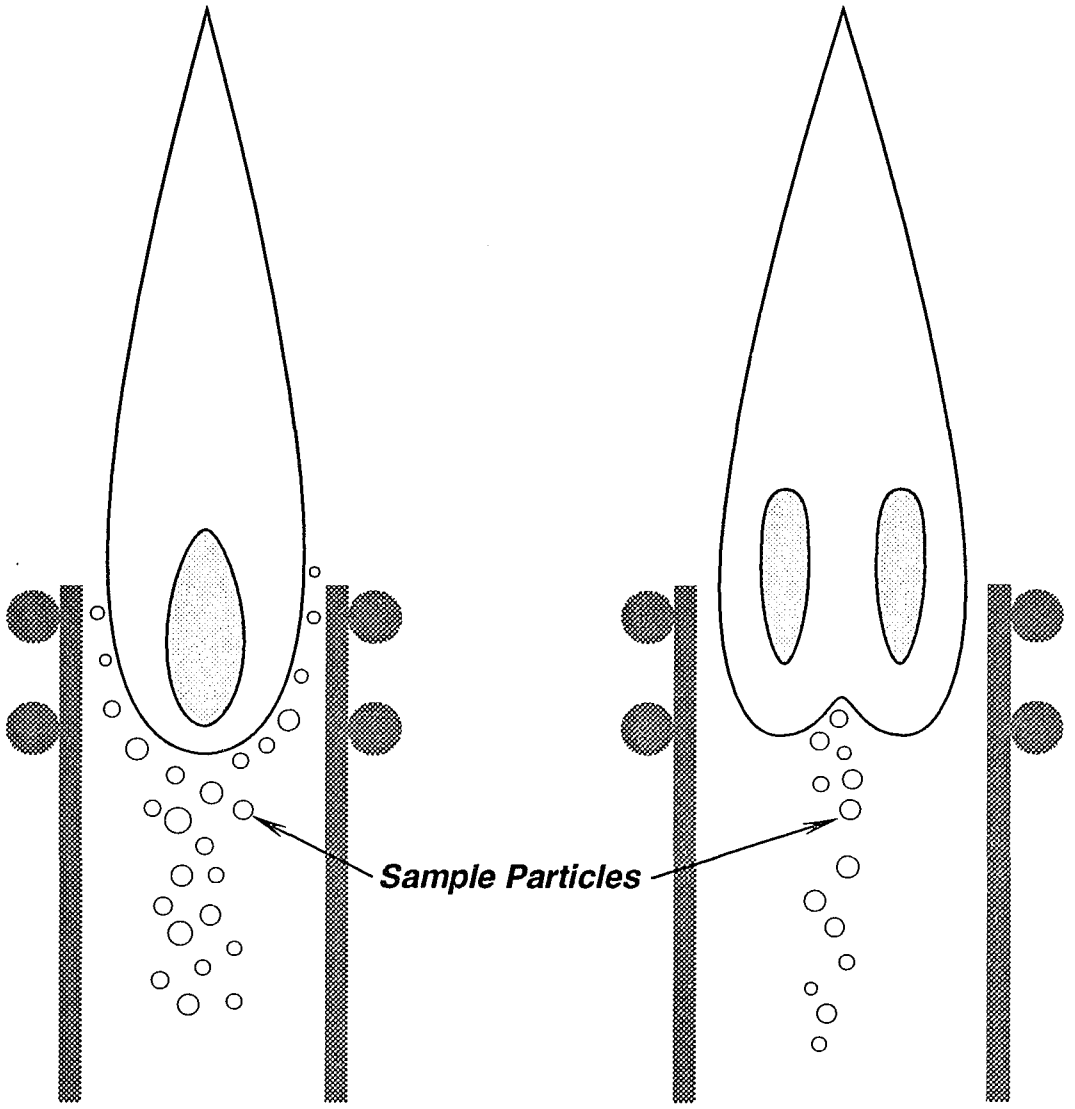

Figure 3.5 Plasma shapes at 5MHz (a) and 27 MHz (from Reference 31).

The operating power or "forward power" of the plasma has an important effect on the signals of analyte and background ions. When the forward power increases, the background signals of ArN^+, ArO^+, and Ar^+ are found to decrease [45]. However, the optimum forward power is mass dependent. For example, according to reference [45], the optimum power for $^{138}Ba^+$ is above 1800 W, while the optimum power for $^{9}Be^+$ is 1300 W. Higher masses require higher power for maximum signal.

The Ar gas used in the ICP has three different functions. Thus, three different Ar flows are used. The cooling flow, generally 13 L/min, must be sufficient to prevent the outer tube of the torch from overheating. The auxiliary flow tends to push the plasma forward. The nebulizer flow (through the inner tube) rate has greatest effect on the analytical performance. It has been reported that the signals of analyte, doubly charged ion, oxide, and background plasma species are affected by the nebulizer flow rate [45, 46, 47]. When the ICP-MS was tuned, we always tried to obtain the optimum operating conditions. Table 3.1 summarizes the operating conditions for plasma torch.

Table 3.1 Operating conditions for plasma torch

Frequency	27.12 MHz
Forward RF Power	1.35 kW
Reflected RF Power	< 2 W
Sampling Depth	12 mm beyond load coil
Coolant Flow(Ar)	13 L/min.
Auxiliary Flow	0.9 L/min.
Nebulizer Flow	0.83 L/min.
Sampling Uptake Rate	0.7 ml /min.

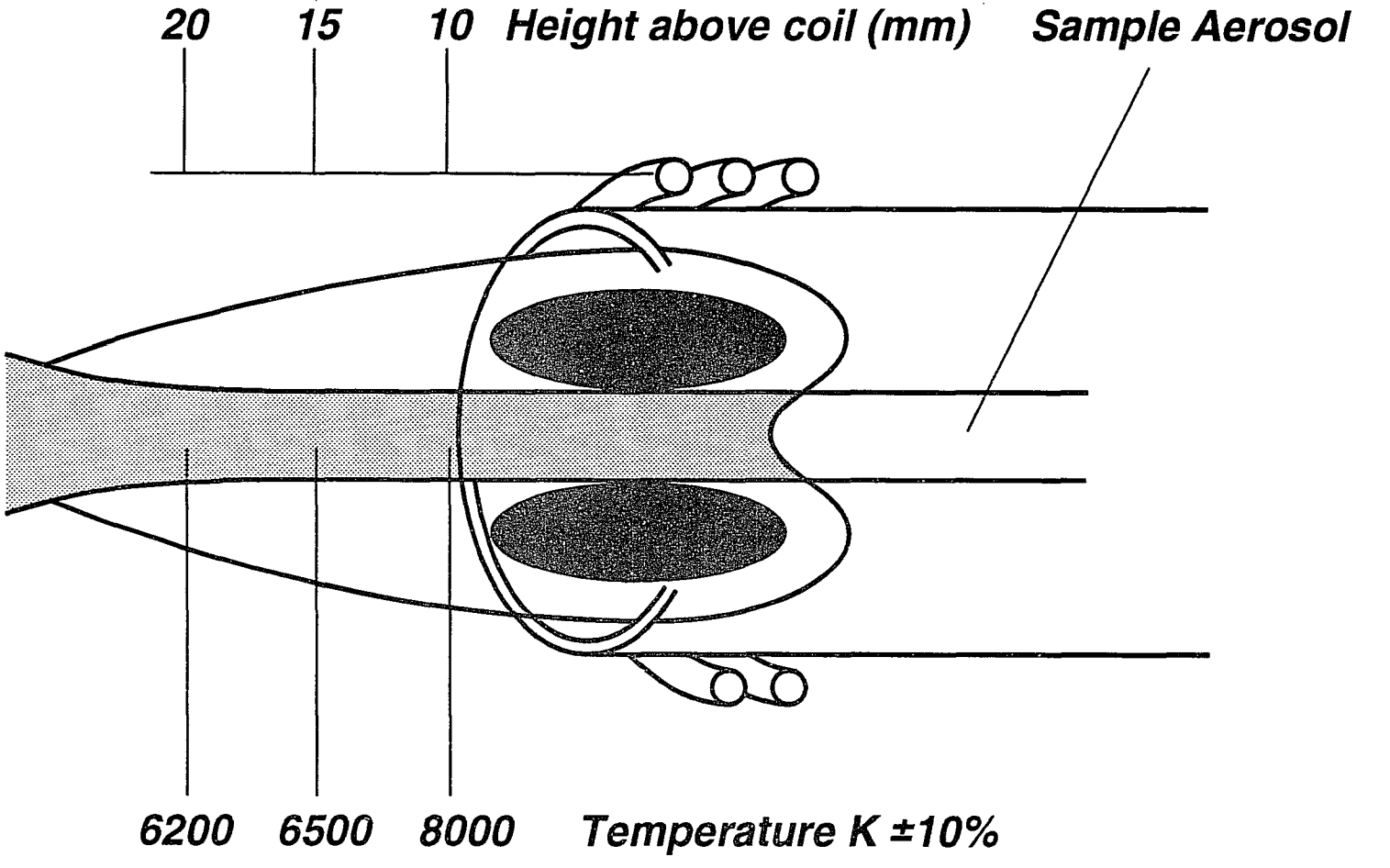

Figure 3.6 Approximate tempertures within plasma (from VG PlasmaQuad Operating Manual 1992).

The temperature in the plasma can be as high as up to 10000 K, depending on the position in the plasma. Figure 3.6 shows some approximate temperatures at various positions in the plasma. The degree to which various elements are ionized is roughly described by the Saha equation (see Chapter 2.1).

3.3 The plasma sampling interface and ion focusing

The function of the plasma sampling interface is to transfer a representative sample of the plasma ion population to the high vacuum chamber where ion focusing lenses can function. The interface and ion focusing lens geometry are shown in Figure 3.7.

The interface consists of two cones: a sample cone with 1.0 mm aperture and skimmer cone with 0.75 mm aperture. The distance between two cones is 7 mm. Both cones are machined from pure nickel, a metal which has good thermal conductivity and mechanical robustness, and reasonable resistance to the commonly used acids. The geometry and aperture of sampling cone are designed such that it can ensure continuum flow through the aperture, eliminate electrical discharges at the orifice, reduce nickel background, and reduce any sample condensation problem. The conditions of the skimmer cone tip has direct bearing on the sensitivity of the instrument and the formation of some polyatomic species.

The plasma operates at atmospheric pressure, while the quadrupole ion analyzer operates at high vacuum. Therefore, a low pressure condition must be met within the interface. This is performed by pumping the interface (expansion) using a rotary pump. The lens stage (intermediate) and analyzer are evacuated by diffusion pumps. When the instrument is operating, the

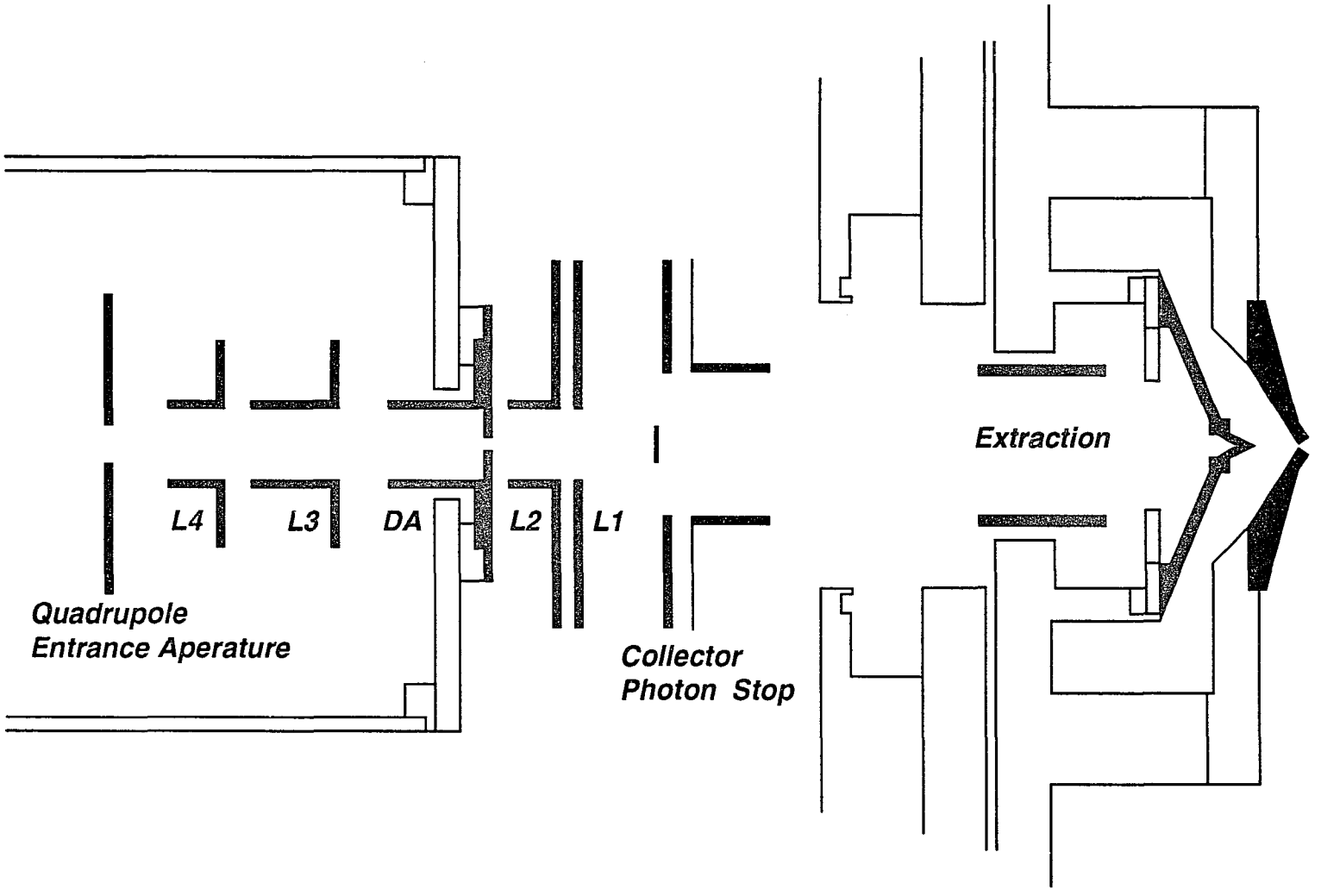

Figure 3.7 The ICP interface and ion focusing lens (from VG PlasmaQuad Operating Manual 1992).

pressures within different stages are: expansion, 1 mbar; intermediate, less than 1×10^{-4} mbar; and analyzer, less than 2×10^{-6} mbar.

Charged species in the region behind the tip of the skimmer cone are separated from neutral species, focused through a differential pumping aperture, and then attracted into the quadrupole entrance aperture, by the ion optic system. The system consists of a number of axially symmetric lens elements on the system axis and the lens supply unit (see Figure 3.7).

The negative voltage on the extraction electrode extracts positive ions from interface and directs them towards the lens stack. Negatively charged species are repelled and neutral atoms and molecules diffuse away from the system axis towards the intermediate diffusion pump. After passing through the slide valve aperture, located in front of the collector, the ions are entrained by the collector electrode. Mounted on the collector is the on-axis photon stop. This prevents light from passing down the otherwise unobstructed system axis and being detected by the electron multiplier. Ions appearing around the photon stop are focused through the differential pumping aperture by lens elements L1 and L2. The final lens elements serve to refocus the ions emerging from the differential aperture into the entrance aperture of the quadrupole.

3.4 The quadrupole mass analyzer

The ions produced in the plasma and passing through the lens stack are detected by an electron multiplier sequentially. The sequence of ions reaching the detector is controlled by the quadrupole mass filter or mass analyzer, which can select ions of a specific small range of mass-to-charge ratio, rejecting all others. The quadrupole mass filter supplied with the

instrument is a VG Quadrupole SXP 300. It consists of four 12-mm diameter, 230-mm long, molybdenum rods held in a square array (see Figure 2.2) which produces a field between the rods that is a good approximation to the ideal hyperbolic quadrupole field. The principle of the operation has been stated in Chapter 2.

3.5 The ion detector and signal handling

The ion detector used on the VG PlasmaQuad is an electron multiplier, which can produce signals proportional to the ion flux transmitted by the quadrupole. The electron multiplier comprises a narrow (about 1 mm internal diameter) curved glass tube around 70 mm long with a resistive coating of typically 10^8 ohms down the whole length.

As the sample ions leave the quadrupole they are attracted by a high voltage applied to the multiplier, which is off the axis of the instrument to reduce the chance of detecting stray photons as shown in Figure 3.8. A positive ion striking the funnel causes the ejection of one or more secondary electrons from the surface, which are accelerated down the tube. These secondary electrons are released and an exponential avalanche builds up down the funnel. The electron gain is dependent on the voltage applied to the multiplier.

The electron multiplier detection system on the VG PlasmaQuad can be operated in pulse-counting mode or analog (extended dynamic range) mode, or the combination of the two modes called dual mode.

The pulse-counting mode with gain of 10^7 to 10^8 electrons per ion is a highly sensitive mode used to measure the ultra-trace (10^{-4} to 10^{-7} ppm) and trace (10^2 to 10^{-4} ppm) level of elements present in a sample. The applied

voltage (HT) in the pulse counting mode ranges from -3000 V to -3500 V. Because the avalanche reaches saturation due to space charge in the pulse counting mode, output pulses for ions are of relatively constant height and can be counted individually.

The overall gain in the analog mode ranges from 10^3 to 10^4 with the applied voltage (HT) -1300 V to -1800 V. This mode is mainly used to measure the minor and major constituents of a sample. The avalanche does not reach saturation in the analog mode so pulses are integrated and the average current is measured.

Dual mode combines the pulse-counting mode and analog mode automatically. It allows an extended dynamic range covering 8 orders of magnitude to be detected. In dual mode, major, minor, trace and ultra-trace elements in the same solution can be detected in one acquisition, without the need for dilution. During the dual-mode acquisition, if the response for any isotope is high i.e. $> 2\times10^6$ counts per second, then the detector will ensure that these elements are not analyzed in pulse-counting mode. The detector is protected from high ion fluxes thus increasing its lifetime.

The detection limits of the instrument for specific elements will be discussed in Chapter 5.

As shown in Figure 3.1, the amplified signal from the electron multiplier is transferred to a external 486 (25 MHz) personal computer (ACMA). The computer is equipped with PQ Vison (Version 4.05) software which runs under the OS/2 operating system.

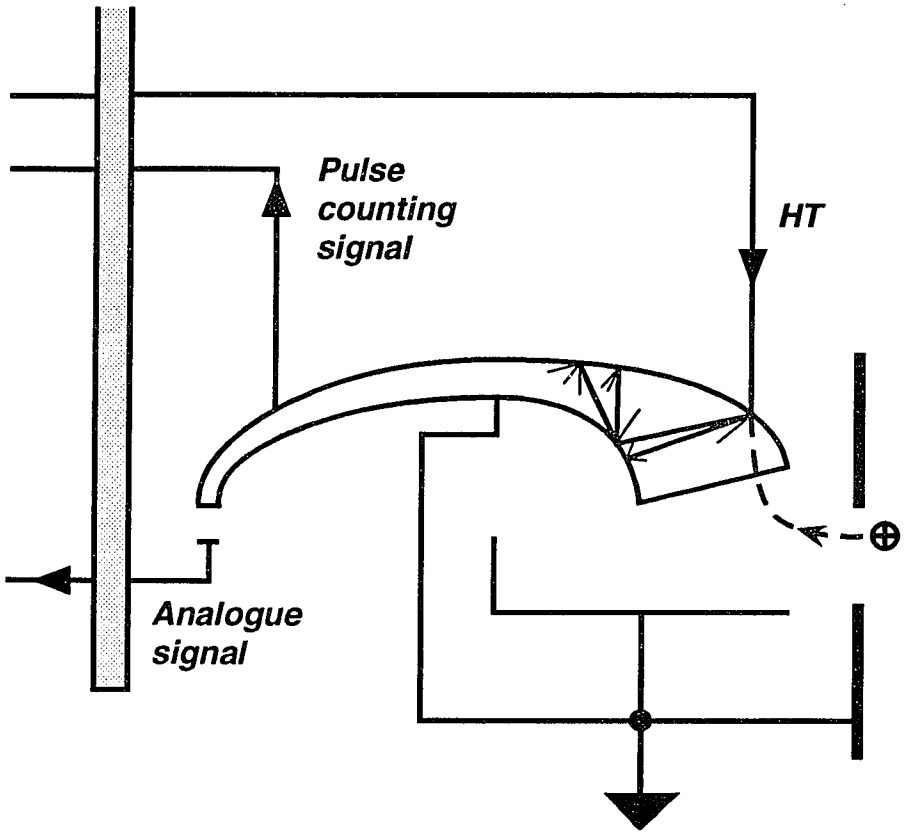

Figure 3.8 Ion detection system.

Chapter 4 Interferences in ICP-MS

One impediment to high accuracy determinations using ICP-MS is interferences. The interferences are usually referred to as spectral interference and nonspectral interference. A spectral interference is caused by an overlap of the analyte signal with the signals having the same mass-to-charge ratio as the analyte species. This type of interference includes isobaric and polyatomic ion interferences. A nonspectral interference is caused by suppression or enhancement of analyte signal by the presence of matrix elements.

4.1 Isobaric interferences

Since most elements have more than one isotope and isotopes of different elements could have the same atomic mass (isobars), the signals of these isotopes will overlap if they are present in the same analyte solutions. For example, the most abundant neodymium isotope, ^{142}Nd (27.09%), suffers from an interference from ^{142}Ce (11.07%). Most of such interferences can be avoided by choosing to analyze other isotopes of the same element, e.g. ^{146}Nd (17.26%) is chosen to avoid interference from ^{142}Ce. When we select isotopes to analyze, we can select at least one stable isotope, except indium, which is not overlapped by isotopes of any other elements. Sometimes, in order to improve the accuracy of the analysis, we have to select isotopes with low abundances at the expense of detection limits.

The alternative method to correct for an interference is to measure another isotope of the interferent and subtract the interfering peak intensity

(interference corrections) from that of the analyte if the concentration of the isotope of interest is high enough.

4.2 Polyatomic ion interferences

Polyatomics are generated by interactions with the plasma gas, through atmospheric entrainment, from the solvent employed in the sample solution, and from the sample matrix. The plasma contains neutral and ionic species of carrier gas and matrix which are present at concentrations as much as 10^6 to 10^8 times those of a trace analyte present in the sample solution at level of 1 μg/ml. The majority of interferences are from:

1) argon as a plasma gas;
2) water and mineral acids such as HNO_3, HCl, H_2SO_4 used as analyte solvents;
3) major elements which are present in an analyte solution;
4) the impurities in Ar gas such as Xe and Kr.

Any reactions, even at quite low rate, between such major populations will produce some ions which could cause interference with elements to be analyzed. The common interfering ions are oxides, nitrides, hydroxides, chlorides, carbides, argides and dimolecular ions. Table 4.1 shows some background interferences from HNO_3 solution. Some of these interfering peaks can be seen in Figure 4.1. The interferences from nitric acid solution cause few problems. The worst cases are $^{40}Ar^+$ interfering with $^{40}Ca^+$, the major isotope of calcium (the peaks at 39, 40, and 41 amu are not seen because the count rate of the ions are so high and acquisition of these ions may damage the detector), and $^{40}Ar^{16}O^+$ interfering with $^{56}Fe^+$, the major isotope of iron. In addition, the interfering peaks of $^{38}Ar^1H^+$ and $^{40}Ar^1H^+$

Table 4.1 Common background polyatomic ions.

Probable ion	m/z	Interferes with	Abundance of interfered element
$^{14}N_2^+$	28	$^{28}Si^+$	92.18[a]
$^{14}N_2{}^1H^+$	29	$^{29}Si^+$	4.71
$^{14}N^{16}O^+$	30	$^{30}Si^+$	3.12
$^{14}N^{16}O^1H^+$	31	$^{31}P^+$	100.00[b]
$^{16}O_2^+$	32	$^{32}S^+$	95.02[a]
$^{16}O_2{}^1H^+$	33	$^{33}S^+$	0.75
$^{36}Ar^+$	36	$^{36}S^+$	0.11
$^{36}Ar^1H^+$	37	$^{37}Cl^+$	24.6
$^{38}Ar^1H^+$	39	$^{39}K^+$	93.08[a]
$^{40}Ar^+$	40	$^{40}Ca^+$	96.92[a]
$^{40}Ar^1H^+$	41	$^{41}K^+$	6.91
$^{12}C^{16}O_2^+$	44	$^{44}Ca^+$	2.13
$^{40}Ar^{12}C^+$	52	$^{52}Cr^+$	83.76[a]
$^{40}Ar^{14}N^+$	54	$^{54}Fe^+$	5.90
$^{40}Ar^{14}N^1H^+$	55	$^{55}Mn^+$	100.00[b]
$^{40}Ar^{16}O^+$	56	$^{56}Fe^+$	91.52[a]
$^{40}Ar^{16}O^1H^+$	57	$^{57}Fe^+$	2.25
$^{36}Ar^{40}Ar^+$	76	$^{76}Se^+$	9.12
$^{38}Ar^{40}Ar^+$	78	$^{78}Se^+$	23.61
$^{40}Ar_2^+$	80	$^{80}Se^+$	49.96[a]

a --- most abundant isotope.

b --- monoisotope.

Table 4.2 Additional interferences from some mineral acids in matrix.

Probable ion	m/z	Interference with
$^{35}Cl^{16}O^{+}$	51	$^{51}V^{+}$
$^{35}Cl^{16}O^{1}H^{+}$	52	$^{52}Cr^{+}$
$^{37}Cl^{16}O^{+}$	53	$^{53}Cr^{+}$
$^{37}Cl^{16}O^{1}H^{+}$	54	$^{53}Cr^{+}$ and $^{54}Fe^{+}$
$^{40}Ar^{35}Cl^{+}$	75	$^{75}As^{+}$
$^{40}Ar^{37}Cl^{+}$	77	$^{77}Se^{+}$
$^{35}Cl_2^{+}$	70	$^{70}Ge^{+}$
$^{37}Cl_2^{+}$	74	$^{74}Ge^{+}$
$^{32}S^{16}O^{+}$	48	$^{48}Ti^{+}$
$^{32}S^{16}O^{1}H^{+}$	49	$^{49}V^{+}$
$^{32}S^{18}O^{+}$	50	$^{50}V^{+}$ and $^{50}Ti^{+}$
$^{32}S^{18}O^{1}H^{+}$	51	$^{51}V^{+}$
$^{32}S_2^{+}$ or $^{32}S^{16}O_2^{+}$	64	$^{64}Zn^{+}$
$^{40}Ar^{32}S^{+}$	72	$^{72}Ge^{+}$
$^{40}Ar^{34}S^{+}$	74	$^{74}Ge^{+}$
$^{31}P^{16}O^{+}$	47	$^{47}Ti^{+}$
$^{31}P^{16}O^{1}H^{+}$	48	$^{48}Ti^{+}$
$^{31}P^{16}O_2^{+}$	63	$^{63}Cu^{+}$
$^{40}Ar^{31}P^{+}$	71	$^{71}Ge^{+}$

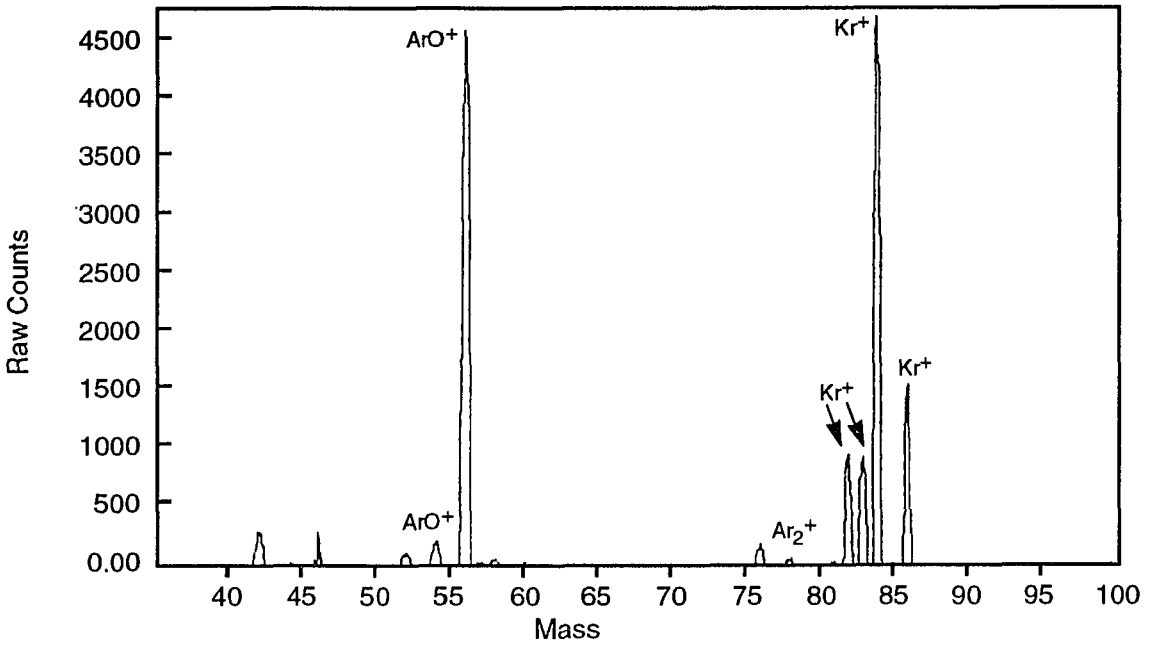

Figure 4.1 ICP-MS Spectrum of 2% HNO_3 Solution.

are so intense that potassium, a rather abundant element in nature, can not be analyzed. Other acids such as hydrochloric acid, sulfuric acid, or phosphoric acid cause more serious interferences (see Table 4.2). A typical ICP-MS background spectrum contains a large number of peaks over the mass range of 0 to 80 amu, but few above that range (the appearance of Kr peaks in Figure 4.1 could have be avoided if pure Ar gas had been used). Since we only employed HNO_3 and HF to digest samples, the background ions caused from HCl, H_2SO_4, or H_3PO_4 may be neglected as long as the samples do not contain large amount of elements Cl, S, and P.

Figure 4.1 shows that argon atoms prefer to form argides with light elements. However, oxygen atoms react with both light and heavy elements in the plasma to form oxides. So, the polyatomic interferences arising from oxide formation cover a wide range of the ICP-MS spectrum. The common oxide interferences are found in determination of rare earth elements (REE) in geological materials [47, 48, 49]. Due to their high monoxide dissociation energy, barium and light REE oxides interfere with determination of the heavy REEs. To check the extent to which barium and light REE oxide interfere with heavy REE analyses we ran approximately 50 ppm solutions of Ba and Sm. The spectra are shown in Figure 4.2 and Figure 4.3, respectively. Barium has seven isotopes. The peaks in the spectrum shown in Figure 4.2 represent oxides of ^{134}Ba (2.4%), ^{135}Ba (6.59%), ^{136}Ba (7.81%), ^{137}Ba (11.32%), and ^{138}Ba (71.66%). The peak at 155 amu is probably formed by ^{138}Ba hydroxide. The rare earth elements suffering from BaO^+ interferences are Eu, Sm, and Gd (see Figure 4.2). Samarium also has seven isotopes. Its oxide and hydroxide peaks cover the range of 160 to 171 amu in which Gd, Dy, Ho, and Er are interfered (see Figure 4.3). The concentrations of $^{147}Sm^{16}O$, $^{149}Sm^{16}O$, and $^{152}Sm^{16}O$ are equivalent to 19.2 ppb of ^{163}Dy,

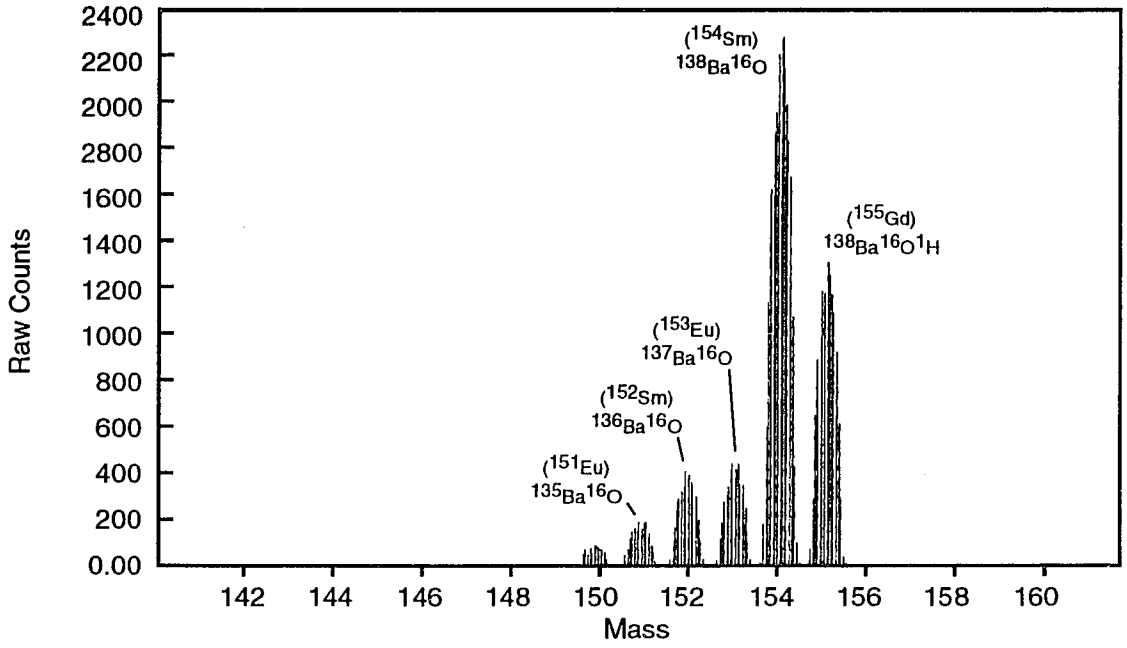

Figure 4.2 Spectrum for 48 ppm Ba solution.
Operating conditions:
RF power = 1.35 kw, spray chamber temperature = 0.5°C.
The isotopes in parenthesis indicate the interferred isotopes.

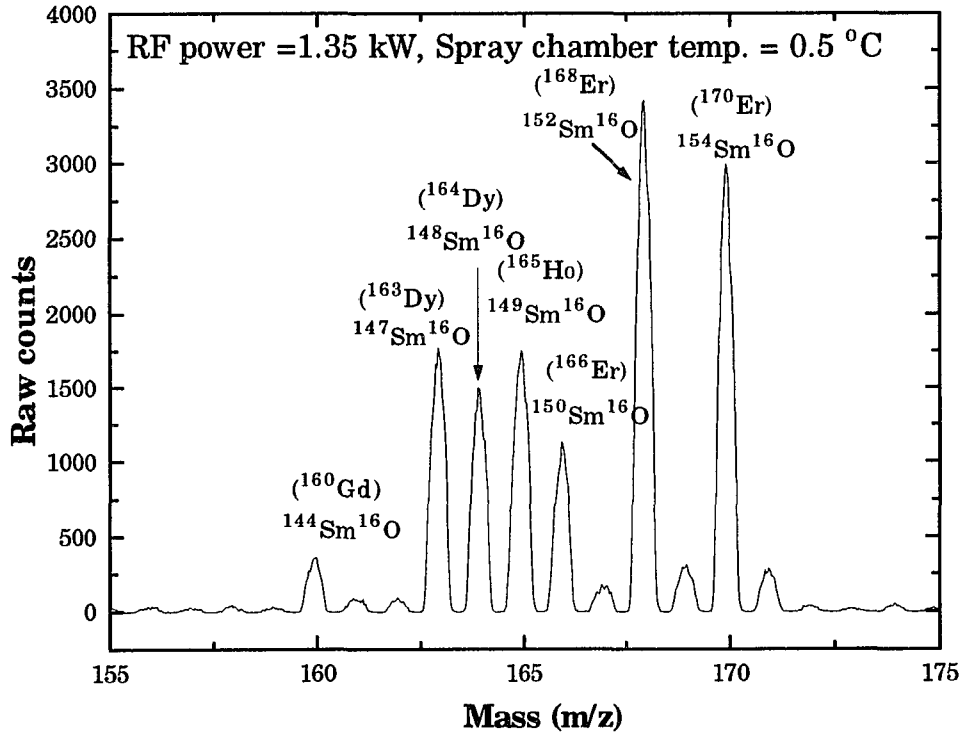

Figure 4.3 Spectrum for 49 ppm Sm (The isotopes in parenthesis indicate the interfered ions). The concentrations of $^{147}Sm^{16}O$, $^{149}Sm^{16}O$, and $^{152}Sm^{16}O$ are equivalent to 19.2 ppb of ^{163}Dy, 4.9 ppb of ^{165}Ho, and 32.0 ppb of ^{168}Er, respectively.

4.9 ppb of ^{165}Ho, and 32.0 ppb of ^{168}Er, respectively. The MO^+/M^+ ratios obtained by our experiment were about 2×10^{-3}, which were close to the ratios reported by Longerich *et al.* [49].

The formation of polyatomic ions in the plasma results directly in a decrease in sensitivity and an increase in analytical error. Many methods have been employed to reduce and/or correct for polyatomic problems.

The plasma conditions play an important role in reduction of MO^+ formation. Lichte *et al.* [47] reported that an increase in RF power and a decrease in nebulizer flow rate could decrease the MO^+/M^+ ratio. These effects are easily understood. In the former case, the bond in MO is broken more efficiently at high temperatures. In the latter case, less oxygen from the aqueous solvent is available to react with metal elements to form oxides.

The majority of oxygen atoms are from water solvent. Therefore, control of the water content may have a considerable influence on the formation of oxides. In practical operation, control of the water loading can be realized by two techniques: simply by cooling the spray chamber or by a desolvation system.

A decrease in temperature in the spray chamber results in less water vapor or aerosol water droplets. The sample aerosol droplets can be separated from water vapor before they enter the plasma. The effect of temperature in the spray chamber on BaO formation is shown in Figure 4.4. We ran different concentrations of Ba solutions at two spray chamber temperatures. At 0.5 ^oC BaO^+ produced from 50 ppm Ba is equivalent to 0.8 ppb Eu, and at 10.0 ^oC the corresponding oxide is equivalent to 1.7 ppb Eu. It is interesting to note that the plot of equivalent Eu concentration against the concentration of Ba is linear.

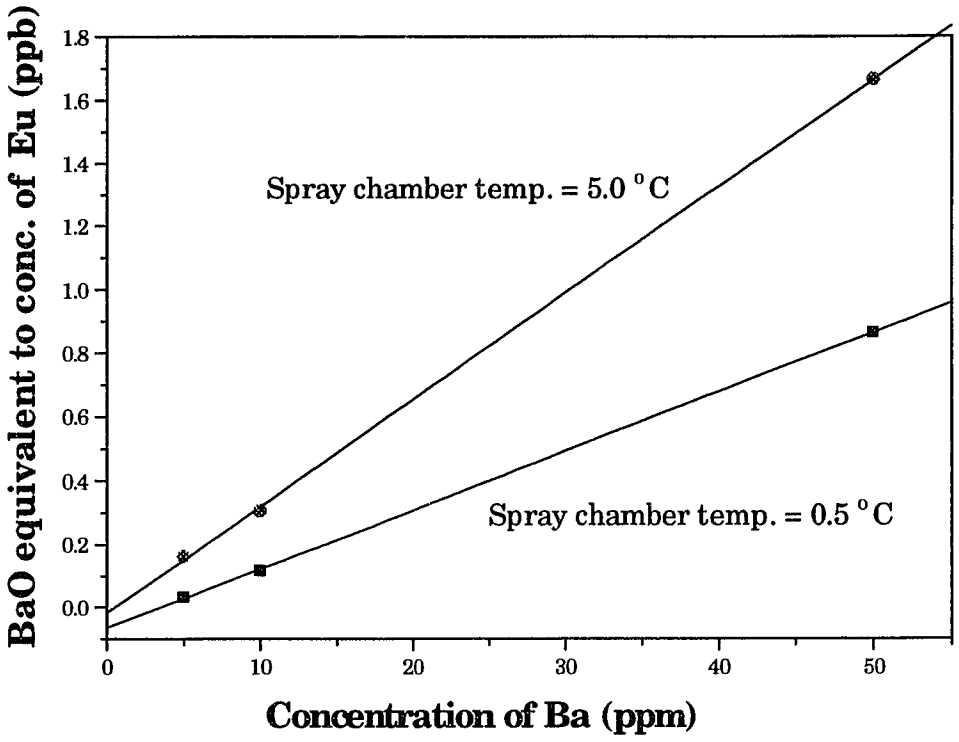

Figure 4.4 Effect of temperature in spray chamber on BaO formation.

Many systematic investigations have been reported for the application of desolvation to ICP-MS. An ultrasonic nebuliser can improve the detection limits by a factor of 10 compared with pneumatic nebuliser [75]. Jakubowski *et al.* [50] introduced a new nebulization technique, the hydraulic high pressure nebulization (HHPN) to ICP-MS. Up to 80% of solvent could be extracted from the drain of the desolvation system. In comparison to conventional pneumatic nebulization, an intensity gain by a factor of 31 was observed with HHPN for 22 elements [51]. Another powerful desolvation system, electrothermal vaporization (ETV), has been investigated in the past few years by Gray and Date [43], Gregoire [52], Park and Hall [53], Tsukahara and Kubota [54], Shibata [55]. In the reference 55, the authors reported that by use of the ETV nebulizer, the MO^+/M^+ ratio for 11 rare earth elements were in the range of 10^{-3} to 10^{-5}, 2 or 3 orders of magnitude smaller than those obtained by the conventional nebulization technique.

A more straightforward modification of polyatomic ions is the introduction of molecular gases into the argon gas flow of a conventional plasma. Houk *et al.* [56] added xenon to the aerosol gas flow of an argon ICP-MS to reduce polyatomic ions such as N_2^+, HN_2^+, NO^+, ArH^+, ClO^+, ArC^+, $ClOH^+$, ArN^+ and ArO^+. They found that the addition of Xe to nebulizer gas facilitates the measurement of ^{28}Si, ^{29}Si, ^{39}K, ^{41}K, ^{51}V, ^{52}Cr, ^{53}Cr, ^{54}Cr, ^{54}Fe, ^{56}Fe. Evans and Ebdon [57] introduced an organic solvent (e.g. propanol) or O_2 and N_2 into the nebulizer gas flow of the ICP to reduce $ArCl^+$ and Ar_2^+ for determination of ^{75}As, ^{76}Se, ^{77}Se, and ^{78}Se in matrices with a high chloride content. In addition, introduction of N_2 into the outer gas flow of an Ar ICP to attenuate a number of background ions (ArO^+, $ArOH^+$, Ar_2^+, ClO^+, and $ArCl^+$) has been studied by other researchers [46, 58, 59].

An alternative approach to correct the oxide and hydroxide overlap problem is to employ the factor analysis method to separate the overlapping oxides from singly charged species. Vaughan and Horlick reported that factor analysis can be used to determine some elements in the presence of high concentrations of interfering oxide formers [60].

4.3 Doubly charged ions

Doubly-charged ions are another type of spectral interference. An isotope with mass M may interfere with the isotope with mass M/2. Only the elements with lower second ionization potentials have great tendency to form doubly-charged ions. The expression of doubly charged ion level has been stated in Chapter 2. The highest level of doubly-charged ion formation expected for any element is only approximately 10% of the total analyte ion density. These levels of M^{2+} are expected only for Ba and several rare earths which have second ionization potentials of 10 eV to 11 eV (see Table 2.1). In our experiment, 47.8 ppm of Ba solution generated about 1 ppm $^{138}Ba^{2+}$ ions.

As with oxides, the doubly-charged ion response varies with plasma parameters, particularly with injector flow rate. With the PlasmaQuad ICP-MS, the doubly-charged ion concentrations increase at higher injector flow rate [61].

4.4 Non-spectral interferences

Signal suppression or enhancement of the analyte ions by the concentration of concomitant elements was observed as early as 1980 [20].

Non-spectral interferences or matrix effects has long been a very important analytical problem in the determination of trace elements in solutions containing high concomitant elements, e.g. in human serum (total cation concentration equivalent to 9 g/l NaCl) or in sea water (35 g/l NaCl). Gray and Date [43] reported 30% and 15% suppressions for cobalt and bismuth, respectively, by 1 g/l sodium, whereas Douglas and Houk [62] observed 10% signal suppressions for copper and zinc by 1 g/l sodium. More serious signal suppressions for chromium, gallium, and zinc were claimed by Horlick *et al.* [63]. A typical ICP-MS spectrum describing suppression of analyte signal caused by concomitant ions is shown in Figure 4.5.

As shown in Figure 4.5, the matrix effect increases with decreasing first ionization energy of the matrix element. Olivares and Houk [64] proposed that the matrix effects from matrix elements are due to suppression of the ionization of the analyte element caused by the extra electrons from ionization of the matrix element forcing the ionization reaction of the analyte back to the neutral atom side as indicated by the following equilibrium:

$$M \rightleftharpoons M^+ + e^-$$

However, Vandecasteele *et al.* [65] disagreed with this conclusion. A possible explanation for the matrix effect is that the total number of ions in the plasma increases when easily ionized elements are injected into the plasma. At high salt concentrations, the matrix ion comprises a significant fraction of the total number of ions. The total number of ions in the plasma, and thus also the number of extracted ions and the space-charge effect, are then expected to increase in going from the matrix ions with higher first ionization potentials to those with lower first ionization potentials. If the

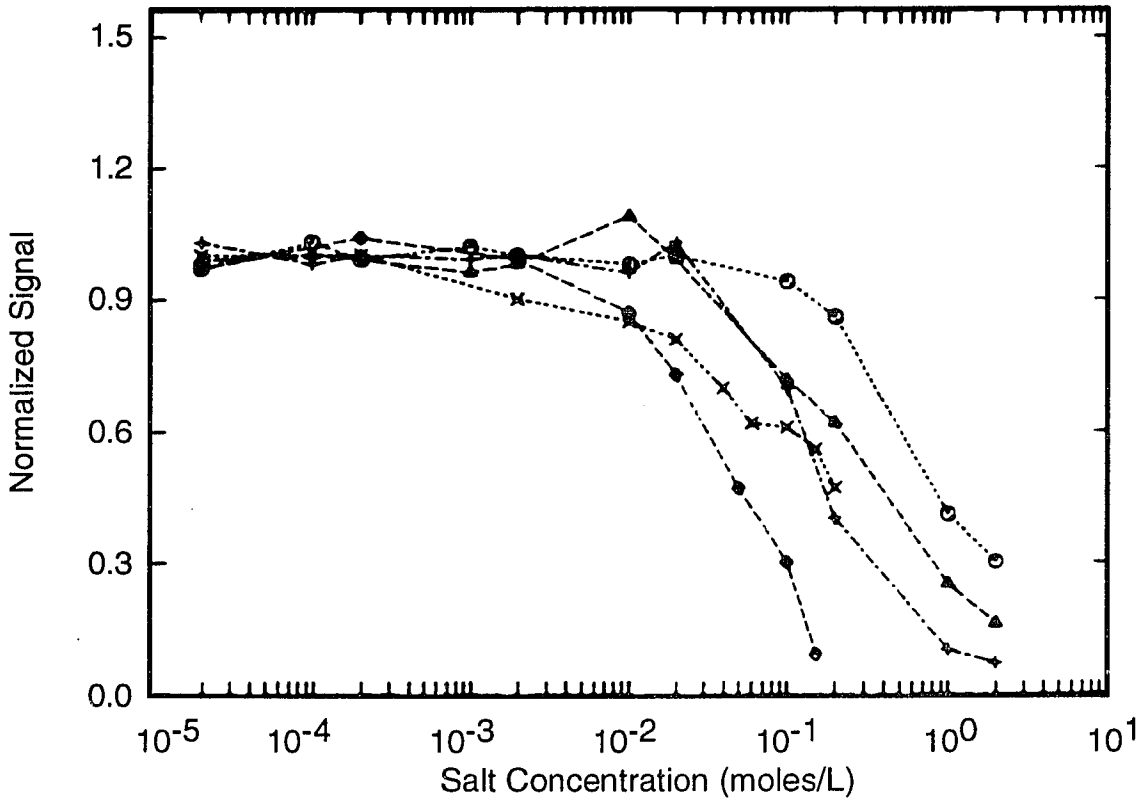

Figure 4.5 Experimentally determined suppression of cobalt ion signal vs. concomitant salt concentration. The matrix salts used are NaCl (◊), $MgCl_2$ (×), NH_4I (+), NH_4Br (Δ), and NH_4Cl (O) (from reference 64).

total number of ions flowing through the sampling cone and skimmer interface is large enough (about 2×10^9 ions/s) [66], focusing can be affected through space charge effects: repulsion of positive ions, resulting in a mass-dependent change in the fraction of ions that reach the mass spectrometer's detector.

Another potential source of ICP-MS matrix effects is the deposition of solid material on the sampling orifices and on the ion optics of the mass spectrometer. If the sampling orifice size changes, the throughput of sample into the spectrometer changes. A change in sample type (such as from sample containing high salt concentrations to standard solution without matrix elements) may produce an abrupt change in signal intensities as deposited material is removed.

Almost any element present at a high concentration (> 100 ppm) can cause errors in ICP-MS. But heavy elements produce larger matrix effects than do light elements. Because heavy ions are transmitted through the sampling cone and skimmer interface more efficiently than are light ions, the matrix suppression effect increases with the mass of the matrix ion.

There are five possible approaches to circumvent non-spectral interferences: (1) the internal standardization method, (2) the standard addition method; (3) the use of isotope dilution, (4) the isolation of the analyte, and (5) optimization of plasma parameters.

In method 5, the matrix effects are minimized by reducing the nebulizer gas flow rate, but at the expense of sensitivity. Matrix composition has no effect on isotope dilution determinations (method 3), because the isotope ratios for the sample and the blend are affected in the same fashion. The commonly used techniques to separating matrix elements from analytes in

determination of trace elements by ICP-MS are solvent extraction [67, 68] and chromatography [69].

Among the methods mentioned above, standard addition and isolation of the analytes are time consuming and isotope dilution is not applicable to monoisotopic elements. Significant improvements in the accuracy and precision obtainable by ICP-MS are achievable through internal standardization, if we can select an internal standard element that is appropriate for the particular analyte(s) and matrix element(s) under consideration.

Chapter 5 Analytical methods

Like most instrumental methods of analysis, ICP-MS cannot give an absolute value for the concentration of an element or isotope, because it is a comparative technique. The quantitative analysis is achieved by comparison of the measured counts from an unknown sample with those from a standard containing a known amount of the element or isotope of interest. Calibration strategies of ICP-MS include external standardization, internal standardization, standard addition, and isotope dilution. The choice of these calibration systems depends on the characteristics (matrix, content, *etc.*) of the sample to be analyzed.

5.1 Signal Drift and Internal Standard

Signal drift is a phenomenon where the signals of analytes fluctuate with time. This phenomenon has been described by many previous investigators [20, 64, 70, 71], as being due to a clogging of the sample introduction system including the nebulizer and/or partial clogging of the sampling cone. The problem will become serious when a high-salt solution is run. Because the sampling cone is water cooled, a solution with a high matrix content may condense on both the back and the front of the cooled sampling cone. Solids deposition will therefore reduce the area of the orifice of the cone, leading to a decrease in the flow of ions from the ICP. In addition to clogging, temperature has some effect on stability of the instrument.

To test the stability of the instrument, we ran a digested volcanic rock solution which had 50 ppb Mo and Bi. There was no rinse between each replicate. The intensity fluctuation of these elements' signals are shown

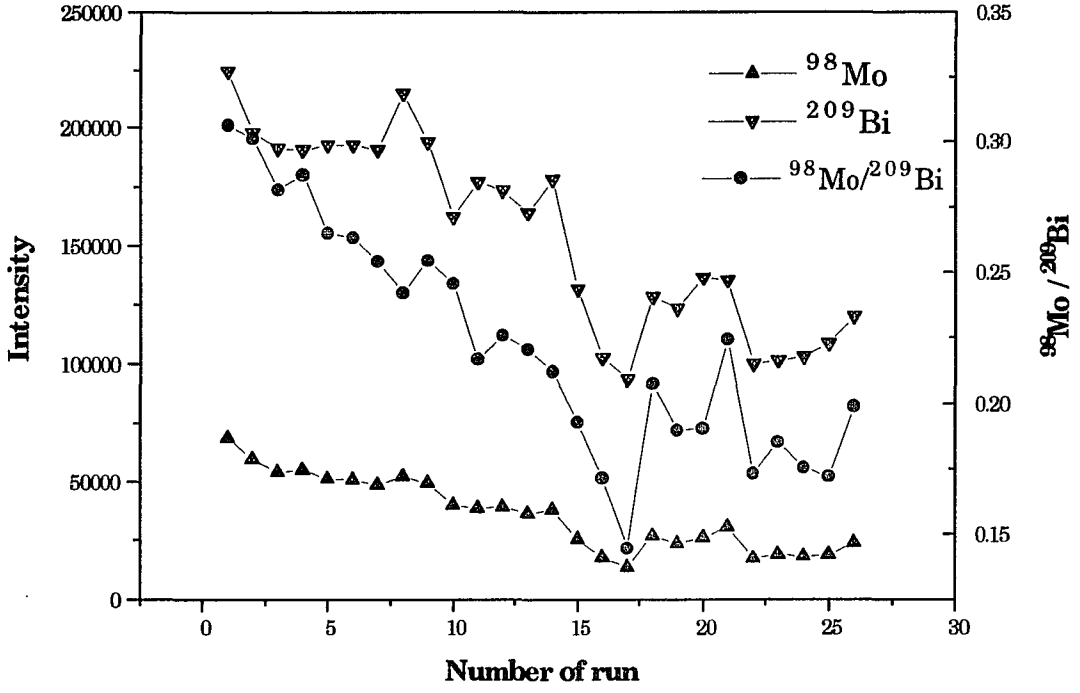

Figure 5.1 Test of signal drift. A volcanic rock solution was run 26 times without washing. Total running time was 90 min. The plot of intensity ratio of $^{98}Mo/^{209}Bi$ versus number of run shows that Mo is not a good internal standard for Bi (The data were provided by Miss Lina Patino, one of the ICP-MS users in our laboratory).

graphically in Figure 5.1. During the 90 minute test, the signals of the metals from the same solution were reduced about 30% by the 18th run, indicating serious drift under no-wash condition when high matrix solution was analyzed.

As with matrix effect, signal drift results in reduction of the signal intensity, thus making accuracy and sensitivity poor. To solve the problem caused by signal drift, at least three methods are used: 1) repeat running standard solution(s) after every 3-5 sample runs to monitor the extent of drift; 2) increase rinse time to wash out the solid depositing on the sampling cone; and 3) spike internal standard(s) to sample and standard solutions. The first method is time-consuming especially when a large number of samples are analyzed. The second method is necessary but not effective enough because each rinse may not produce an identical "cleaning effect". Internal standardization is the most common method used to correct the analytical error produced by signal drift. This method is based on the fact that the signal of a properly chosen internal standard increases or decreases in the same proportion as the signal of analyte.

The requirements for an internal standard are:

1) not present in samples;

2) represents the mass range of interest;

3) has isotopes with m/z values that do not interfere with other components in the sample;

4) rinses adequately;

5) ionization potential is close to those of analytes.

In our experiments, we used ^{115}In as an internal standard for multielement analyses and ^{205}Tl for Pb determinations.

To investigate the validity of using internal standards to correct for signal drift, we ran a 50 ppb rare-earth-element solution (ICP-MS SPEX1) to which the same concentration of In was added. The running conditions were: uptake time 45 seconds, acquisition time 60 seconds, and rinse time 45 seconds. The intensities of 50 ppb REEs and In are listed in Table 5.1. Even if there are no matrix elements (SPEX1 contains REE only), signal drift still can be observed. The signals of 50 ppb REE decreased gradually. The REE signal ratios of the last run to the first run are 0.8 and relative standard deviations within 20 runs are 15% to 18%. If we choose ^{115}In as an internal standard, the REE signal drifts are improved greatly as shown in Table 5.2. Relative standard deviation for 50 ppb REE signals decrease to 2%.

The experiment showed that REEs' signal drift can be corrected by normalizing their signals by the internal standard. In is a suitable internal standard for this purpose. The extent to which In signal decreased is the same as that of rare earth elements (run 20/run 1 $\approx$ 0.8). As shown in Figure 5.2, nine out of fourteen REEs' signal curves are close to straight line when they are normalized by In. The normalized signals of Tb, Tm, Ho, Yb, and Pr do not vary too much with the run number. This experiment confirms the validity of using In as an internal standard for rare earth elements.

5.2 Calibration

There are two categories of calibrations: instrument calibrations and quantitative analysis calibrations. The first category of calibrations include mass calibration, detector calibration, and response calibration, while external-standard calibration and semiquantitative calibration belong to quantitative calibration.

Table 5.1 Test of signal drift using 50 ppb rare-earth-element solution.

replicate	In	La	Ce	Pr	Nd	Sm	Eu	Gd
1	1.39E5	1.73E5	1.67E5	2.08E5	3.77E4	3.22E4	1.08E5	3.50E4
2	1.32E5	1.65E5	1.57E5	1.98E5	3.55E4	3.03E4	1.02E5	3.30E4
3	1.27E5	1.60E5	1.51E5	1.91E5	3.40E4	2.94E4	9.95E4	3.17E4
4	1.20E5	1.49E5	1.42E5	1.79E5	3.27E4	2.75E4	9.35E4	3.04E4
5	1.19E5	1.52E5	1.43E5	1.83E5	3.27E4	2.85E4	9.37E4	3.07E4
6	1.25E5	1.55E5	1.48E5	1.84E5	3.36E4	2.87E4	9.53E4	3.09E4
7	1.29E5	1.62E5	1.52E5	1.93E5	3.48E4	2.98E4	9.80E4	3.18E4
8	1.20E5	1.51E5	1.43E5	1.82E5	3.25E4	2.83E4	9.34E4	3.00E4
9	1.23E5	1.53E5	1.46E5	1.84E5	3.32E4	2.87E4	9.32E4	3.05E4
10	1.20E5	1.47E5	1.42E5	1.77E5	3.22E4	2.73E4	9.09E4	2.97E4
11	1.19E5	1.49E5	1.41E5	1.77E5	3.23E4	2.76E4	9.03E4	2.99E4
12	1.18E5	1.50E5	1.42E5	1.78E5	3.23E4	2.77E4	9.07E4	2.98E4
13	1.22E5	1.53E5	1.44E5	1.83E5	3.31E4	2.83E4	9.45E4	3.08E4
14	1.20E5	1.51E5	1.45E5	1.82E5	3.24E4	2.86E4	9.20E4	3.06E4
15	1.24E5	1.55E5	1.48E5	1.85E5	3.43E4	2.93E4	9.63E4	3.15E4
16	1.22E5	1.53E5	1.45E5	1.85E5	3.31E4	2.91E4	9.31E4	3.15E4
17	1.16E5	1.43E5	1.37E5	1.73E5	3.11E4	2.68E4	8.90E4	2.92E4
18	1.14E5	1.44E5	1.39E5	1.73E5	3.17E4	2.74E4	8.97E4	2.86E4
19	1.18E5	1.49E5	1.41E5	1.80E5	3.22E4	2.78E4	9.12E4	2.94E4
20	1.11E5	1.40E5	1.36E5	1.70E5	3.07E4	2.62E4	8.83E4	2.87E4
average	1.14E5	1.44E5	1.39E5	1.73E5	3.17E4	2.74E4	8.97E4	2.86E4
s. d.	1.98E4	2.35E4	2.23E4	2.70E4	4.91E3	4.24E3	1.39E4	4.41E3
rsd(%)	17	16	16	16	15	15	15	15
run20/run1	0.80	0.81	0.81	0.82	0.82	0.81	0.82	0.82

Table 5.1 (continued).

replicate	Tb	Dy	Ho	Er	Tm	Yb	Lu
1	2.31E5	5.59E4	2.23E5	5.03E4	2.27E5	4.84E4	2.17E5
2	2.17E5	5.24E4	2.11E5	4.89E4	2.16E5	4.56E4	2.02E5
3	2.09E5	5.06E4	2.04E5	4.58E4	2.06E5	4.45E4	1.94E5
4	1.98E5	4.75E4	1.91E5	4.32E4	1.92E5	4.15E4	1.84E5
5	2.01E5	4.90E4	1.92E5	4.45E4	1.96E5	4.28E4	1.86E5
6	2.04E5	4.87E4	1.96E5	4.47E4	1.99E5	4.25E4	1.87E5
7	2.12E5	5.03E4	2.01E5	4.63E4	2.05E5	4.47E4	1.96E5
8	2.00E5	4.87E4	1.94E5	4.46E4	1.95E5	4.23E4	1.84E5
9	2.04E5	4.92E4	1.93E5	4.44E4	1.95E5	4.20E4	1.86E5
10	1.94E5	4.74E4	1.86E5	4.32E4	1.92E5	4.05E4	1.80E5
11	1.95E5	4.74E4	1.86E5	4.31E4	1.91E5	4.08E4	1.81E5
12	1.96E5	4.76E4	1.90E5	4.35E4	1.94E5	4.15E4	1.82E5
13	2.03E5	4.93E4	1.94E5	4.45E4	1.97E5	4.23E4	1.87E5
14	2.02E5	4.87E4	1.92E5	4.48E4	1.97E5	4.25E4	1.85E5
15	2.04E5	5.03E4	2.01E5	4.63E4	2.01E5	4.30E4	1.91E5
16	2.03E5	4.94E4	1.97E5	4.44E4	1.98E5	4.29E4	1.88E5
17	1.91E5	4.57E4	1.82E5	4.11E4	1.83E5	3.98E4	1.78E5
18	1.91E5	4.65E4	1.86E5	4.22E4	1.90E5	3.97E4	1.79E5
19	1.97E5	4.79E4	1.91E5	4.36E4	1.91E5	4.16E4	1.81E5
20	1.86E5	4.54E4	1.80E5	4.11E4	1.84E5	3.90E4	1.72E5
average	1.91E5	4.65E4	1.86E5	4.22E4	1.90E5	3.97E4	1.79E5
standard dev.	3.19E4	7.37E3	3.08E4	6.54E3	3.07E4	6.69E3	3.16E4
rsd(%)	17	16	17	15	16	17	18
run20/run1	0.8	0.81	0.81	0.82	0.81	0.8	0.79

Table 5.2 Normalization of signal drifts of 50 ppb REEs to the In signal.

replicate	La/In	Ce/In	Pr/In	Nd/In	Sm/In	Eu/In	Gd/In
1	1.24	1.20	1.50	0.271	0.232	0.775	0.251
2	1.26	1.20	1.50	0.270	0.230	0.777	0.251
3	1.26	1.19	1.50	0.268	0.231	0.784	0.249
4	1.24	1.19	1.50	0.273	0.229	0.779	0.253
5	1.28	1.20	1.53	0.274	0.239	0.785	0.258
6	1.24	1.18	1.48	0.269	0.230	0.764	0.248
7	1.26	1.18	1.50	0.270	0.231	0.761	0.247
8	1.25	1.19	1.51	0.270	0.235	0.775	0.249
9	1.25	1.19	1.50	0.270	0.234	0.760	0.249
10	1.23	1.18	1.48	0.268	0.228	0.759	0.248
11	1.25	1.18	1.49	0.271	0.232	0.758	0.251
12	1.27	1.20	1.51	0.274	0.234	0.768	0.252
13	1.25	1.18	1.50	0.271	0.232	0.774	0.252
14	1.26	1.21	1.52	0.270	0.238	0.767	0.255
15	1.25	1.20	1.49	0.276	0.236	0.776	0.254
16	1.26	1.19	1.52	0.272	0.239	0.765	0.259
17	1.24	1.18	1.50	0.268	0.232	0.768	0.252
18	1.26	1.22	1.52	0.278	0.240	0.786	0.250
19	1.26	1.20	1.53	0.273	0.236	0.774	0.250
20	1.26	1.22	1.53	0.276	0.236	0.794	0.258
average	1.25	1.19	1.50	0.272	0.234	0.772	0.252
s.d.	0.01	0.01	0.02	0.01	0.01	0.01	0.01
rsd(%)	1	1	1	1	2	1	1

Table 5.2 (Continued).

replicate	Tb/In	Dy/In	Ho/In	Er/In	Tm/In	Yb/In	Lu/In
1	1.66	0.401	1.60	0.362	1.63	1.56	0.535
2	1.65	0.398	1.61	0.372	1.64	1.54	0.559
3	1.65	0.398	1.60	0.361	1.62	1.53	0.560
4	1.65	0.396	1.59	0.360	1.60	1.53	0.552
5	1.68	0.411	1.61	0.373	1.65	1.56	0.568
6	1.63	0.391	1.57	0.358	1.59	1.50	0.553
7	1.65	0.390	1.56	0.359	1.59	1.52	0.548
8	1.66	0.405	1.61	0.370	1.62	1.53	0.552
9	1.66	0.401	1.57	0.362	1.59	1.52	0.549
10	1.62	0.396	1.55	0.360	1.60	1.50	0.529
11	1.63	0.398	1.56	0.362	1.60	1.52	0.538
12	1.66	0.403	1.61	0.369	1.64	1.54	0.555
13	1.66	0.404	1.59	0.364	1.61	1.53	0.541
14	1.68	0.406	1.60	0.373	1.64	1.54	0.557
15	1.65	0.406	1.62	0.373	1.62	1.54	0.542
16	1.67	0.407	1.62	0.365	1.62	1.55	0.556
17	1.65	0.395	1.57	0.355	1.58	1.54	0.533
18	1.68	0.407	1.63	0.370	1.66	1.56	0.549
19	1.68	0.407	1.62	0.370	1.62	1.54	0.529
20	1.67	0.409	1.62	0.369	1.65	1.55	0.545
average	1.66	0.401	1.61	0.365	1.62	1.53	0.547
s.d.	0.02	0.01	0.02	0.01	0.02	0.02	0.01
rsd(%)	1	1	1	2	1	1	2

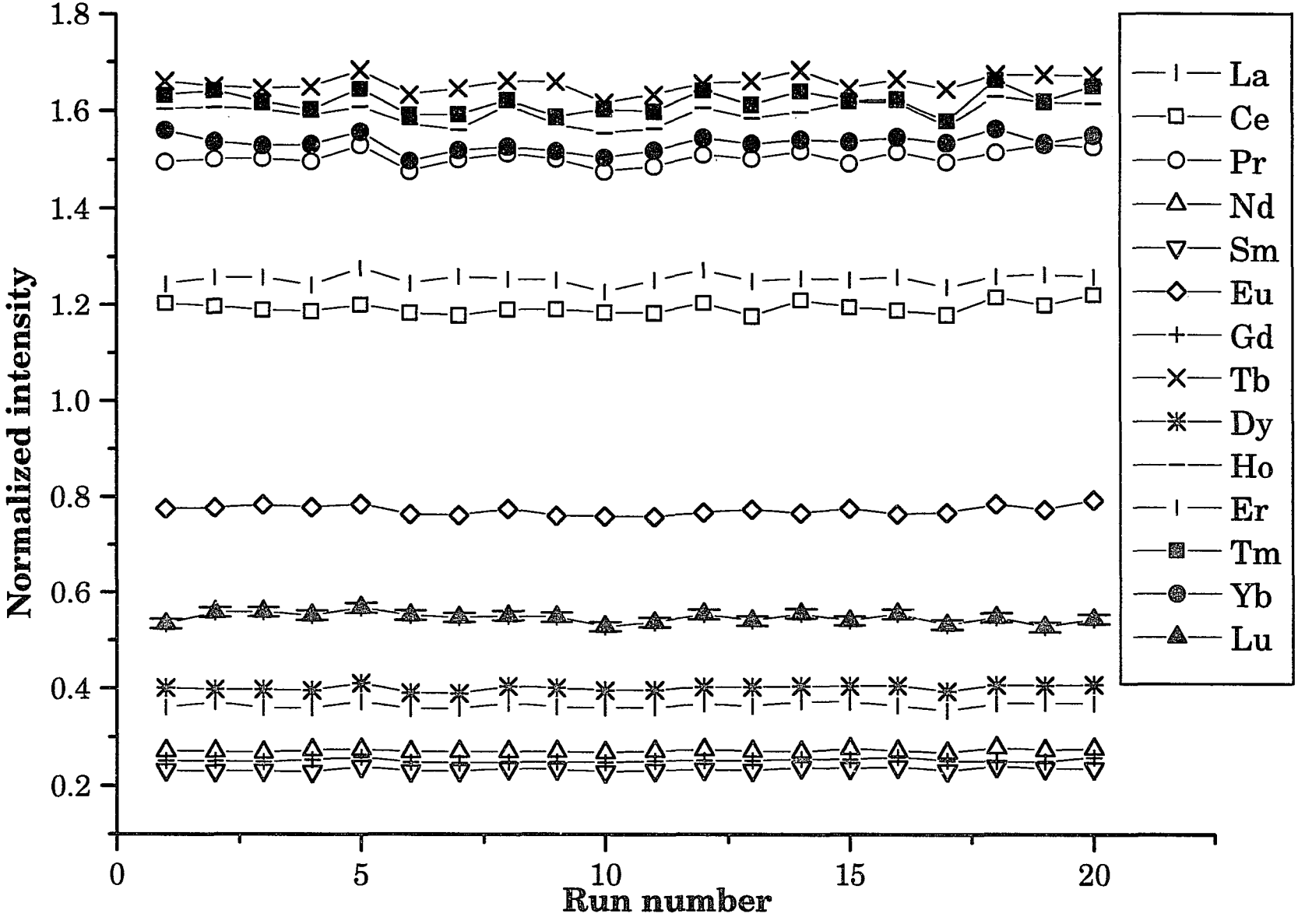

Figure 5.2 Signal intensities of 50 ppb REEs normalized to In. Note abence of drift. Error bars are shown for Lu only.

5.2.1 Mass calibration

Among these instrument calibrations, mass calibration is performed most frequently (once a month or every other week). Mass spectrum calibration examines whether peaks of isotopes are located in the right mass scale in the spectrum. If slightly out of calibration, peak-jump data may have fewer counts and scan data will be marginally affected; e.g. wrong isotope ratios are obtained. The mass scale is normally calibrated across the entire mass range using a 25 ppb standard solution containing multiple and high-abundance elements such as Be, Co, In, Ho and Bi.

5.2.2 External-standard calibration

External-standard calibration is a technique for quantitative analysis (the other techniques are standard addition and isotope dilution which will be described later). This technique can be used in either single-element or multielement mode.

In ICP-MS, the external-standard calibration is similar to those employed in ICP-AES and AAS. Usually the calibration curve contains two or more points of standard data. In our experiment, sometimes even a one point calibration can provide good results because of the wide linear dynamic range of the instrument. Typical calibration curves for selected elements are shown in Figure 5.3. The seven data points of REEs in the figure correspond to the solutions of 0.045, 0.505, 5.39, 25.75, 50.74, 99.96, 196.8, and 500.0 ppb.

The calibration curves are linear over 5 orders of magnitude, from 0.045 ppb to 500 ppb with average linear regression value R equal to 0.99959, thereby allowing analysis to be performed without the requirement for dilution or preconcentration. It is worth pointing out that the detection

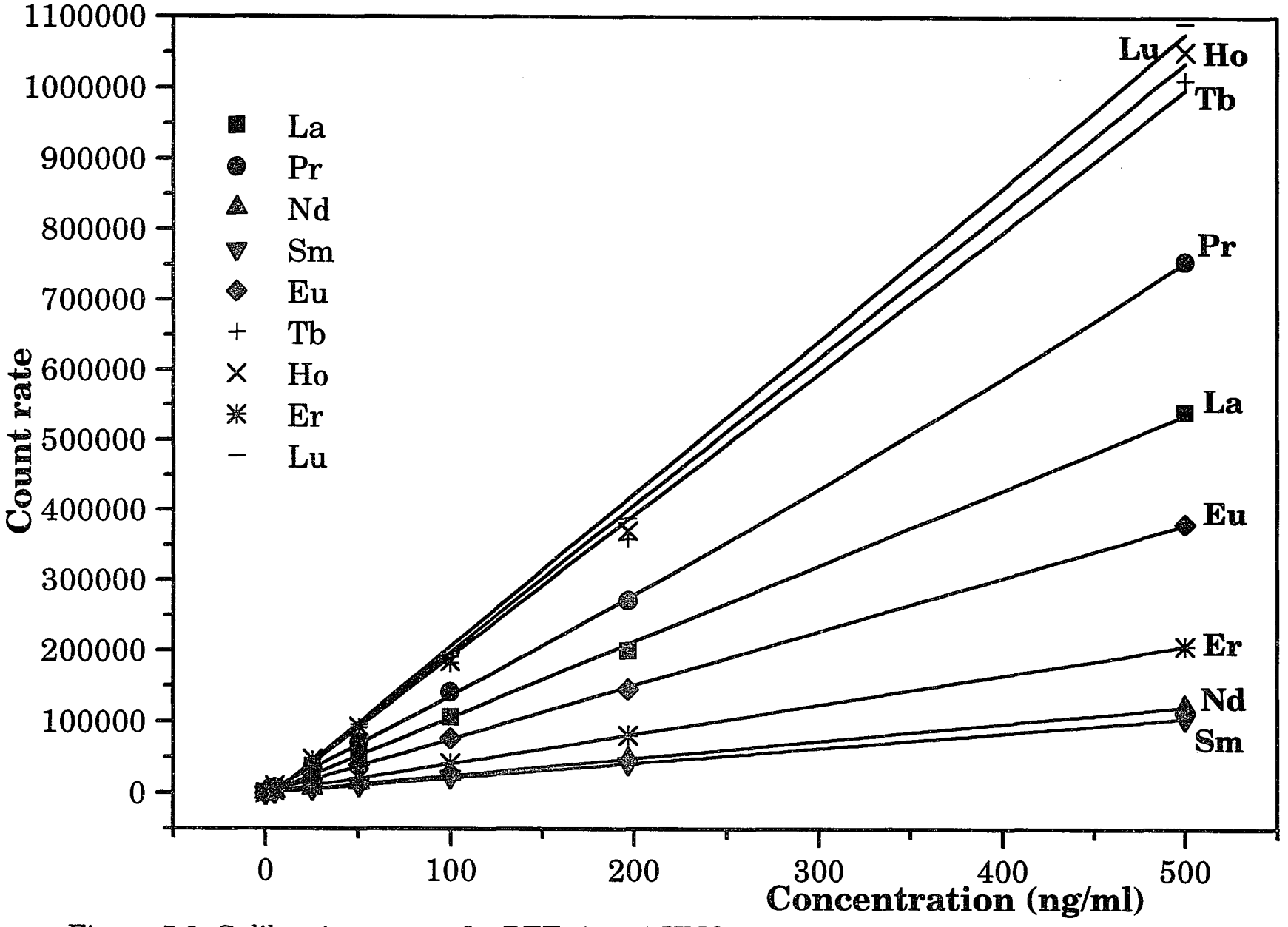

Figure 5.3 Calibration curves for REEs in 2% HNO_3

modes of analog and pulse counting were not mutually calibrated. Otherwise, the dynamic range could be up to 7 orders of magnitude.

With the external calibration curves we can calculate concentrations of analytes using the following equation:

$$C_{un} = \frac{I_{un}}{I_{std}} \times \frac{Ab_{un}}{Ab_{std}} \times \frac{C_{un(In)}}{C_{std(In)}} \times C_{std} \times \frac{I_{std(In)}}{I_{un(In)}} \times D$$

where I_{un} is the intensity of selected isotope of unknown;

I_{std} is the intensity of the same isotope of standard;

Ab_{un} is the abundance of the selected isotope of unknown;

Ab_{std} is the abundance of the same isotope of standard;

C_{std} is the concentration of standard;

$C_{un(In)}$ is the concentration of internal standard spiked in unknown;

$C_{std(In)}$ is the concentration of internal standard spiked in standard;

$I_{std(In)}$ is the intensity of internal standard spiked in standard;

$I_{un(In)}$ is the intensity of internal standard spiked in unknown;

D is unknown dilution factor.

The above equation is suitable for a one-point calibration. For more than a one point calibration, a similar equation can be derived.

5.3 Detection limits

The detection limits here are defined as the minimum detectable element concentrations equivalent to three times standard deviations (3σ) of intensities of the peaks of the elements in a blank solution. They depend on ionization energy of analyzed element, isotope abundance, background

intensity, sample preparation procedure, and instrument tuning. For a given element, the first three factors are fixed, and the last two factors play important roles in detection limits. Therefore, the instrument was tuned with 25 ppb In (or other elements, depending on scan range) to obtain maximum ^{115}In count rate before each analysis.

The detection limits of some elements for our ICP-MS are listed in Table 1.2. They were determined by analyzing the procedural blank 10 times as an unknown sample and multiplying the resulting standard deviation by 3. The 3σ count rates were then converted to concentrations by comparing the count rates of 25 ppb standard solution (mixture of SPEX1 and SPEX2 ICP-MS standard) run under the same conditions.

The detection limits of most elements shown in Table 1.2 are in the parts per trillion range except for Fe and Se, because they suffer from background interferences of ArO^+ and Ar^+, respectively.

5.4 Precision and accuracy

Precision, usually expressed as a percent relative standard deviation, indicates the reproducibility of repetitive measurements of equivalent analyte solutions. The accuracy of a measurement is how close the measured value agrees with the true value or certified value. In the ICP-MS technique, the precision and accuracy of isotope ratio measurements are better than those of concentration measurements because the signal drift and matrix interference have little effect on isotope ratio. We found that the accuracy of isotope ratio measurement depends on mass calibration and resolution of the instrument.

To validate the sample preparation method and the ICP-MS analysis, standard reference materials from the National Institute of Standards and Technology (NIST) were analyzed through the same procedure as unknown samples. The NIST standard samples used to check the accuracy of analysis of Pb isotope ratios, water samples, and wood samples were NIST SRM 981 (Common lead), NIST SRM 1643c (Trace elements in H_2O), and NIST SRM 1575 (Pine needles), respectively. The results of analysis of these standard materials are presented in Table 5.3, Table 5.4, and Table 5.5, respectively.

The accuracy of the determination of Pb isotope ratios of NIST SRM 981 was typically better than 2.0%. The ten-run precision was below 0.4%. The isotope ratio test also showed that the standard deviations of any three runs of NIST 981 solution were less than 0.5%. Therefore, in determination of lead isotope ratios in the subsequent samples, each sample was run three times. In analysis of NIST 1643c, most measured values were within the NIST certified ranges. The lower result for Zn may have been produced by an experimental error. When we analyzed the standard sample again, the measured value of Zn was close to the NIST certified value (see Table 7.6). Se has a higher value due to the interference of $^{38}Ar^{40}Ar^{+}$ ion. The accuracy of determination of NIST SRM 1643c, generally below 5%, was better than that of NIST SRM 1575. The reason for negative errors in determination of pine needles is that sample may have been lost in the course of digestion and dilution. But no sample preparation was needed for water samples. The sample preparation procedure for pine needles will be described in Chapter 6.

Table 5.3 Analysis of Pb isotope ratios in 25 ppb NIST SRM 981.

Ratio	^{207}Pb / ^{208}Pb	^{206}Pb / ^{208}Pb	^{206}Pb / ^{207}Pb
Run 1	0.4264	0.4748	1.113
Run 2	0.4264	0.4739	1.111
Run 3	0.4254	0.4705	1.106
Run 4	0.4256	0.4733	1.112
Run 5	0.4221	0.4711	1.116
Run 6	0.4281	0.4740	1.107
Run 7	0.4267	0.4731	1.109
Run 8	0.4257	0.4725	1.110
Run 9	0.4243	0.4733	1.116
Run 10	0.4253	0.4726	1.111
Mean	0.4256	0.4729	1.111
Std Dev	0.0016	0.0013	0.003
% RSD	0.38	0.28	0.30
certified ratios	0.4219	0.4612	1.0933
error(%)	0.88	2.5	1.6

Table 5.4 Determination of trace elements in NIST SRM 1643C (Trace elements in H_2O).

Element	Mass (m/z)	measured (ppb)	NIST certified (ppb)	%error
Al	27	118.2±4.6	114.6±5.1	3.1
V	51	29.9±1.2	31.4±2.8	-4.8
Cr	52	18.4±5.6	19.0±0.6	-3.2
Mn	55	35.1±0.6	35.1±2.2	0.0
Ni	58	58.1±1.8	60.6±7.3	-4.1
Co	59	23.4±0.9	23.5±0.8	-0.4
Cu	65	22.3±0.8	22.3±2.8	0.0
Zn	66	63.7±3.5	73.9±0.9	-13
As	75	78.1±1.0	82.1±1.2	-4.9
Se	78	17.2±0.6	12.7±0.7	35
Rb	85	13.0±0.4	11.4±0.4	14
Sr	88	253.7±9.3	263.6±2.6	-3.8
Cd	114	13.5±1.2	12.2±1.0	11
Ba	138	44.0±1.4	49.6±3.1	-11
Tl	205	6.5±0.4	7.9*	---
Pb	208	37.5±5.8	35.3±0.9	6.2
Bi	209	17.7±3.3	12*	---

* — These values are not certified.

Table 5.5 Determination of trace elements in NIST SRM1575, pine needls.

elment	mass (m/z)	our results (ppm)	NIST certified (ppm)
V	51	0.38±0.03	0.39±0.07
Cr	52	2.9±0.2	2.6±0.2
Ni	58	2.4±0.1	3.5
Co	59	0.096±0.002	0.10*
Cu	65	3.0±0.1	3.0±0.3
Zn	66	56±2	67±9
As	75	0.89±0.03	0.21±0.04
Rb	85	13±1	11.7±0.1
Cd	114	0.21±0.01	< 0.5*
Ba	138	8.6±0.1	7.2±0.9
Tl	205	0.068±0.002	0.05*
Pb	208	12±1	10.8±0.5
U	238	0.023±0.002	0.020±0.004

* — these value are not certified.

5.5 Standard additions

Standard addition techniques are employed in a similar fashion to other analytical procedures. The calibration is performed by taking aliquots of the sample to be analyzed, and adding to each, increasing quantities of a standard reagent containing the element(s) of interest. The increments are normally equal and the number of aliquots taken is at least three, preferably more. The calibration set therefore consists of a number of spiked samples plus the unspiked original sample, all of which have an almost identical matrix. In data analysis, count rates of the isotope of interest versus the concentrations of the element added are plotted in a graph. The intercept of the calibration line on the x axis (a negative number) gives the concentration in the unspiked sample.

We employed the standard addition method to determine concentration of Tl in NIST SRM 1643c water sample. Different amounts of 1.00 ppm Tl solutions were spiked into four 10.0 ml samples of NIST SRM 1643c solution, respectively. Pure water (Millipore) was added to each spiked sample to adjust the volume to give the same dilution factor. The spiked samples were analyzed by ICP-MS in scan mode with scan range 200 to 210 amu. The water sample contains known Pb concentration, which was used as internal standard to monitor a signal drift.

The average count rates of ^{205}Tl and ^{206}Pb are shown in Table 5.6, and count rates of ^{205}Tl normalized by ^{206}Pb versus the concentrations of Tl added are plotted in Figure 5.4. From the intercept of the calibration line on x axis, -7.5 and the uncertainty of the line, 0.3, we obtained the measured concentration of Tl, 8.0 ± 0.3 ppb, which is close to the uncertified value of 7.9

Table 5.6 Data for determination of Tl in NIST 1643c.

Pb conc. (ppb)	32.9	32.9	32.9	32.9
^{206}Pb count rate	51783	49267	46362	44693
correction factor	1	0.9514	0.8953	0.8631
^{205}Tl count rate	81974	140277	224502	295427
corr. ^{205}Tl count rate	81974	147439	250752	342293
Tl added (ppb)	10.11	24.84	46.89	66.90

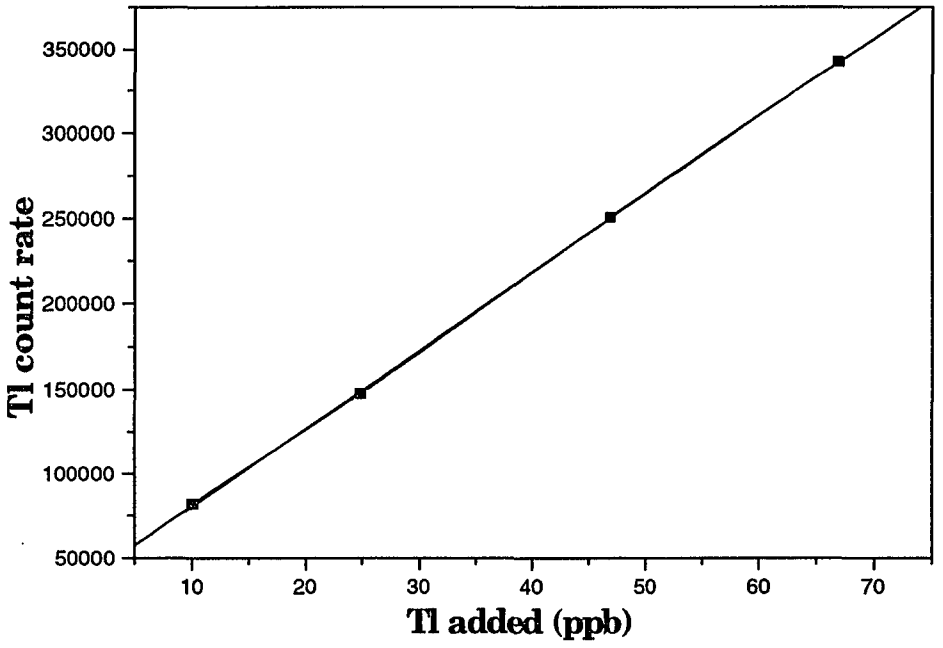

Figure 5.4 Standard addition calibration curve for NIST 1643c.

ppb in NIST 1643c. Note that the absolute value of the intercept has been multiplied by a dilution factor of 1.07.

5.6 Isotope dilution

Isotope-dilution inductively-coupled-plasma mass spectrometry (ID-ICP-MS) is a powerful strategy for elemental analyses which has been used for the accurate and precise determination of elemental concentrations in high matrix samples at ppb or subppb level [72, 73, 74]. The basis of the method is the measurement of the change in the ratio of signal intensities for two selected isotopes of an element of interest after the addition of a known quantity of a spike which is enriched in one of these isotopes. This measurement makes it possible to calculate the concentration of the element in the sample. The method can be applied for any element with at least two stable isotopes, or even for mono-isotopic elements with a suitable long-lived radioisotope.

The isotope dilution technique was applied to determine lead in NIST SRM 1643c (pure water) and NIST SRM 1575 (pine needles).

Fourteen grams (accurately weighed) of NIST 1643c, pure water, was spiked with 100 μl of 1.77 ppm NIST 983 radiogenic lead standard solution. The spiked 1643c water sample was injected into the ICP-MS for determination of ^{208}Pb / ^{206}Pb ratio. A non-spiked sample, prepared in the same manner, and 25 ppb NIST 983 solution were also run to measure their abundances of ^{206}Pb and ^{208}Pb.

The relative abundances of Pb isotopes in NIST 1643c are 1.4% (^{204}Pb), 24.9% (^{206}Pb), 21.2% (^{207}Pb), and 52.4% (^{208}Pb). The spectrum in Figure 5.5(a) shows the characteristic isotopic signature for the four stable isotopes

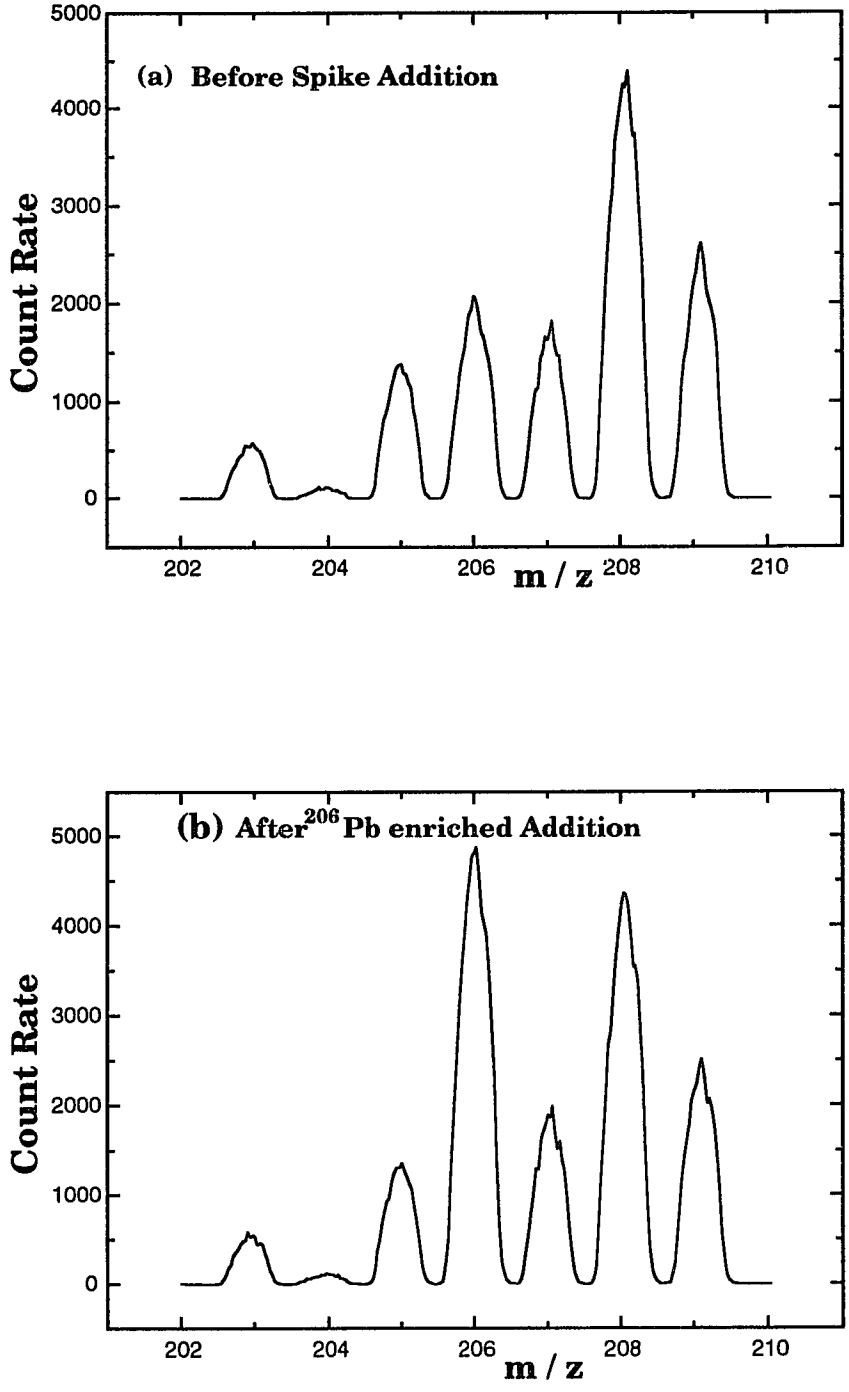

Figure 5.5 Determination of Pb in NIST 1643c, pure water, by isotope dilution.

of Pb in the sample. After being spiked with ^{206}Pb-enriched NIST 983 (the abundance of ^{206}Pb is 91.9%), the abundance of ^{206}Pb in the spiked sample increased as shown in Figure 5.5(b). By measuring the ^{208}Pb / ^{206}Pb ratio of the sample after spike additions, the concentration C of Pb in NIST SRM 1643c can be calculated according to the following formula [75]:

$$C = \frac{M_S \times K (A_S - B_S R)}{W (BR - A)}$$

where

M_S is the mass of the spike expressed in ng or mg,

W is the weight of the sample,

K is the ratio of the natural atomic weight and the atomic weight of the ^{206}Pb-enriched material,

A is the natural abundance of ^{208}Pb (the 'reference' isotope),

B is the natural abundance of ^{206}Pb (the 'spike' isotope),

A_S is the abundance of ^{208}Pb in the ^{206}Pb-enriched spike,

B_S is the abundance of ^{206}Pb in the ^{206}Pb-enriched spike,

R is the measured ^{208}Pb / ^{206}Pb ratio.

The measured concentration of Pb with this method was 34.22±0.01 ppb (number of samples was 2) which was close to the range of the certified value, 35.3±0.9 ppb. The percent error relative to the certified value was 3%.

If a sample is solid and needs to be digested before measurement, it is important to add an isotopic standard to the sample before digestion. In this way, sample losses can be compensated by the loss of spiked standard since both the sample and the spiked standard are lost in the same proportion

Table 5.7 Comparison of results of Pb concentration (μg/g) in pine needles (NIST 1575) by isotope dilution and by regular (external standard) methods. The Student t-test (significance level $\alpha = 0.05$) showed that the means from method (a) and method (b) are not significantly different, but the mean from regular method is significantly different from those from isotope dilution method.

run date	regular method	method(a)	method(b)	NIST certified
1/7/92	12.45, 12.29			
2/6/92	11.02			
2/20/92	11.71, 12.21			
3/5/92	11.18			
3/6/92	12.31, 12.52			
4/16/92	12.02			
4/17/92	11.16			
8/17/92			10.04, 9.41	
10/7/92		10.18, 10.61		
average	11.89	10.40	9.73	10.8
std. dev.	0.58	0.30	0.40	0.5

method(a) --- sample was spiked with Tl before digestion.

method(b) --- sample was spiked with Tl after digestion.

relative to their original masses. Table 5.7 shows the results of a determination of Pb in NIST 1575 pine needles by isotope dilution and by regular method (external standard). The measured concentration of Pb in the sample was closer to the certified value if the sample was spiked before digestion. Also, the result obtained by isotope dilution (method a) is better than that by regular method.

The advantages of isotope dilution method are that accuracy and precision of determination are not affected by instrumental fluctuations, sample losses, and changes in concentration that result from evaporation.

5.7 Semi-quantitative analysis

The semi-quantitative technique provides a method that is suitable for rapidly obtaining information about the composition of an unknown sample thus allowing a more accurate and precise subsequent determination to be performed by other approaches such as external calibration, standard addition, or isotope dilution.

The calibration curve of semi-quantitative mode is obtained by scanning the mixed aqueous standards of known concentration in full mass range (4 m/z to 240 m/z, skipping some intensive background ranges), and plotting the relative intensities of the elements in mixed standards against their atomic numbers or the m/z values. The mixed standard solution contains 6 to 8 elements suitably spread across the mass range. The ideal isotopes of these elements should be monoisotopic and free from interference from background intensity. ^{115}In or ^{103}Rh is normally chosen as an internal standard in standard and sample solutions. A simulated semi-quantitative calibration curve is described in Figure 5.6. Once the calibration curve is established, the

concentration of all elements can be determined in an unknown sample by reference to the curve.

To perform semi-quantitative analysis, samples spiked with internal standard are run under the same operating conditions as the standard solution, e.g. the same mass range and dwell time. The concentrations of elements are calculated in terms of the following equation:

$$C_m = \frac{I_m\,(smpl) / I_{in}\,(smpl)}{I_m\,(std) / I_{in}\,(std)} \times C_{in}\,(smpl)$$

where

C_m is the concentration of an element in a sample,

I_m (smpl) is the intensity of the element (per ppb) in the sample,

I_{in} (smpl) is the intensity of In (per ppb) in the sample,

I_m (std) / I_{in} (std) is the intensity (per ppb) ratio of the element to In in standard,

C_{in} (smpl) is concentration of In spiked in the sample.

Unlike quantitative analysis, it is not necessary to run standards each time when unknown samples are analyzed. The accuracy of the data produced by this method is within 20%; however, it is variable and highly dependent on the element sought and the sample matrix.

Among the calibration methods mentioned above, internal standard and external standard were used most in our experiments since they provided good enough accuracy for analysis of our samples.

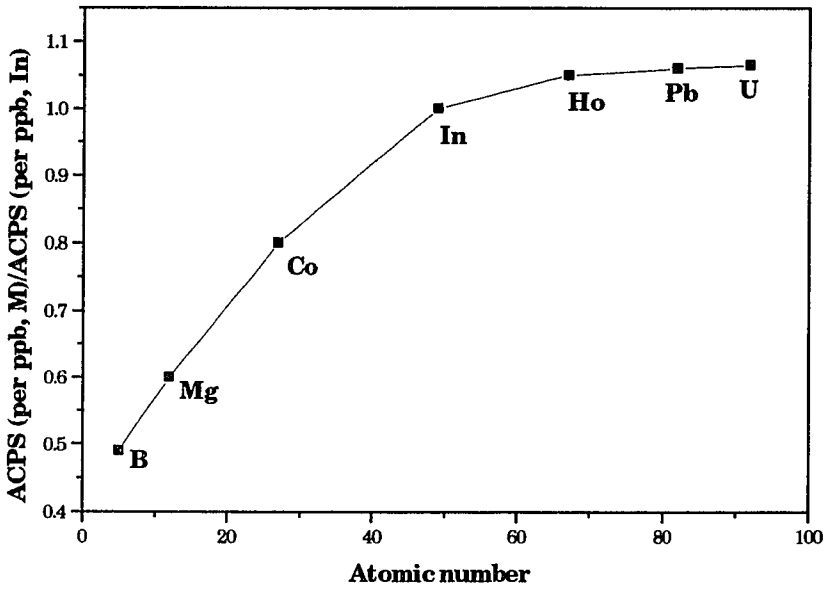

Figure 5.6 Simulated semi-quantitative calibration curve.

Chapter 6 Determination of elemental signatures in annual-growth rings of trees from forest fire

Trees, towering above other vegetation in forests, have interesting elemental chronologies locked away in their annual-growth rings. Trees can be considered indicators that record environmental disturbances in that they capture elements in their annual-growth rings, and, in contrast to lake-core sediments, that these rings are not contaminated naturally by outside sources. There are three pathways for trees to take up elements: (1) uptake from the soil via the roots, with subsequent transport into woody tissue via the transpiration stream; (2) foliar uptake, with subsequent export from the leaf through the phloem, followed by lateral movement from this tissue into the xylem; (3) direct deposition onto stem surfaces followed by lateral movement across the bark and into the wood. Most of the elemental deposits occur via the root system while the remainder is deposited through the foliage and stem surfaces. Throughout the growing season, trees are subjected to different growing conditions such as temperature and precipitation. Other factors that can affect growth are environmental pollution caused by industries and nature, e.g. volcanic eruptions and forest fires.

Many researchers have studied the effect of fire on element transfer from vegetation to the atmosphere [76], and on the soil chemistry in the forest [77]. Fire can have a marked effect on nutrient balance and cycling in ecosystems [78]. One significant impact of fire is the transfer to the atmosphere of a proportion of the elements contained in combusted fuel or strongly heated surface soil. Element transfer to the atmosphere may result from volatilization, particulate (ash) movement or both of these mechanisms.

Particulate matter may be redeposited on the burnt site or adjacent areas either as dry fallout or in rainfall. The concentration of elements in the trees (not necessarily burned) growing on the burnt site and/or on adjacent areas may increase depending on the tree-growth climate conditions, and acidity and chemical properties of the soil.

Tree rings can be considered an ion-exchange column with many binding and exchange sites. Elements form complexes with many amino acids in the wood and in the sap. The stability constants of the complexes vary with the elements and with the acidity of the sap. Some elements will be more stable in the rings than others. The complexes with lower stability constants are easy to translocate from ring to ring and up and down within the tree. Previous experiments [79] showed that the alkali and alkaline earth elements are more prone to translocation in pine trees. This phenomenon makes it difficult to date a fire in terms of these element concentration changes in the trees since these elements in the ring corresponding to the fire year would migrate to older tree rings. Fortunately, the degree of translocation for other elements is not the same and the concentration change of some elements may be used to interpret the tree-growing environment change.

The objective of this experiment was to study the chronological change in elements in tree rings and to determine if elemental signatures exist in the tree rings that reflect the fire history.

6.1 Sample preparation

Samples were obtained from two trees that grew in different places. California Giant Sequoia (*Sequoiadendron giganteum*) was collected from

Sequoia National Park, Sierra Nevada Mountain, at 7000 feet (1960 m) elevation. The other tree, ponderosa pine (*Pinus Ponderosa Lawson*) was sampled from Bandelier National Monument, New Mexico. The samples (two wedges of trees) were dated and fire histories reconstructed based on fire scars by the Laboratory of Tree-Ring Research, University of Arizona, using standard dendrochronological methods [80]. Figure 6.1 shows the wedge of Giant Sequoia.

The samples were dried in the Laboratory of Tree Ring Research before they were shipped to our laboratory. In our laboratory, the wedges of wood were cut across the rings by an electric saw and further separated using a stainless-steel razor to get approximately 200 mg of individual rings covering the range from ten years before to ten years after the fire date. An attempt was made to remove surface contamination from the wood by scraping with a stainless-steel scraper. Subsequently the separated wood was accurately weighed to the nearest 0.01 mg on an analytical balance and transferred to Teflon cups, to which was added 2 ml of J. T. Baker Ultrex HNO_3 and 2 ml of 18 MΩ ultra-pure water from a Millipore water purification system. A cap was placed on the vessels and the apparatus was subjected to microwave heating using a CEM MD-81 microwave digestion system. With 12 bombs heated simultaneously, a power of 80% was used for 20 minutes. The samples were completely digested and the solutions were clear. The digested tree solutions were quantitatively transferred to acid-washed Wheaton polyethylene bottles and diluted to 20 g with 18 MΩ ultra-pure water. Indium was spiked into the sample solutions to use as an internal standard for multielemental analysis. The final solutions were weighed accurately to obtain dilution factors and transferred to 18 mm (i.d.) polypropylene tubes.

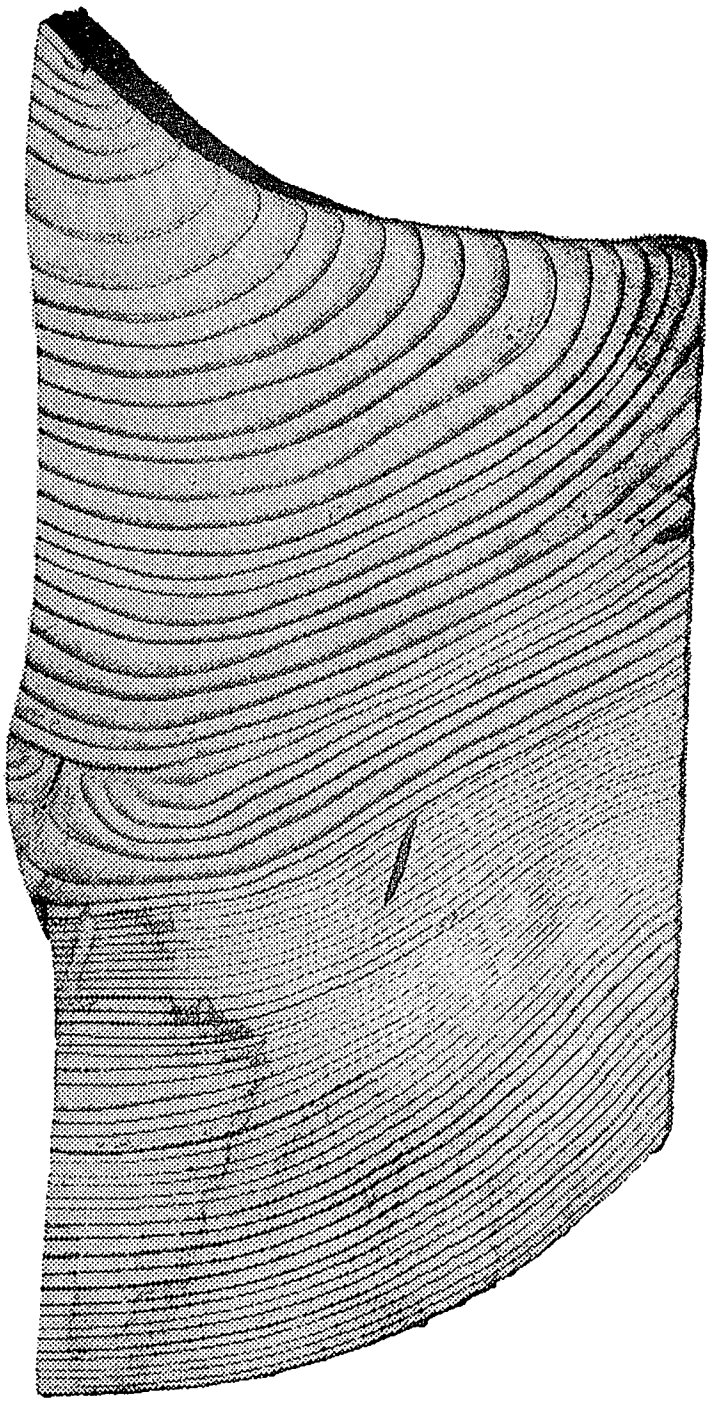

Figure 6.1 Wedge of California Giant Sequoia.

Upon dilution, white precipitates formed from digested ponderosa pine solutions. The problem may come from an uncompleted digestion of colophony or rosin in the pine tree. Colophony contains 80%-90% of abietic acid that is water insoluble. The precipitate would cause a lower analytical result and clog the nebulizer tubing. One effective method to avoid forming a precipitate after digestion was to increase the digestion time and reduce the amount of wood to be digested. Therefore, less than 80 mg of each ring from the pine tree was sampled.

Nitric acid is the optimum solvent to digest tree rings. However, there is some caution that must be addressed about the amount of the acid to use. It was no problem in digesting 200-300 mg of wood using 4 ml of HNO_3. But the concentration of HNO_3 in the final solution was so high that the sampling cone would be attacked by HNO_3. Increasing the dilution factor of each sample could decrease the concentration of HNO_3. But the concentrations of some elements such as rare earths were then too low to be detected. Therefore, the amount of HNO_3 must be minimized. The suitable amount of HNO_3 was derived from simple chemical stoichiometry. During digestion in the microwave system, the chemical reaction of HNO_3 with cellulose, the major component of wood, can be expressed by the following chemical equation:

$$\underset{\text{(cellulose)}}{C_6H_{10}O_5} + 8\,HNO_3 \longrightarrow 6\,CO_2 + 8\,NO + 9\,H_2O$$

If 200 mg of wood is digested with 2 ml of HNO_3 (70% assay, 1.432 g/ml density) and diluted to 20 g with pure water, 0.0093 mole of HNO_3 is consumed to react with wood and 0.022 mole of HNO_3 remains unchanged if

decomposition of the acid is not considered. The residue of nitric acid in the final solution is equivalent to 4.9% HNO_3. Actually, concentrated nitric acid decomposes in the Teflon cup based on the following reaction when it is heated in the microwave oven:

$$4\ HNO_3 \longrightarrow 2\ H_2O + 4NO + 3O_2$$

The decomposition of nitric acid was proven by heating 2 ml of HNO_3 in Teflon cup using the microwave oven and measuring the pH value of the dilute solution. About 27% of HNO_3 changed into NO and O_2. The actual concentration of nitric acid in the final solution was therefore less than two percent.

Our experiment showed that it is necessary to add pure water to the Teflon cup before digestion. Water in the cup speeds up the reaction between nitric acid and wood, and functions as a solvent to dissolve the digested species.

6.2 Standard preparation

Multielemental standard solutions of 10 ng/ml, 50 ng/ml, and 100 ng/ml were prepared by diluting 10 μg/ml SPEX2 solution with 2% HNO_3. SPEX2 contains B, Ba, Ca, Sr, Al, Mg, Rb, As, Se, Pb, In, Bi, Cd, Tl, U, and some transition elements. Dilution was made gravimetrically instead of volumetrically since the former method is more accurate and faster.

Our preliminary analysis showed that wood sample solutions, based on a dilution factor of 100, contained 10 μg/ml K, 4 μg/ml Mg, and 200 μg/ml Ca.

To compensate for matrix effects, the standards were spiked with high purity K, Mg, and Ca to simulate the digested tree-ring matrix.

Ten ng/ml of REEs standard solution was prepared from 10 μg/ml SPEX1 solution in the same manner as SPEX2 standard solutions.

Two certified standards, NIST SRM-1575 (pine needles) and NIST SRM-1571(orchard leaves) were prepared using the procedure stated below:

An accurately weighed 0.25 g sample of the certified standard was transferred to the Teflon cup to which 2 ml of concentrated HNO_3 and 1 ml of HF was added. The cup with polymer jacket was subjected to microwave digestion. Six samples were digested simultaneously and completely at 70% full power for 12 minutes. After digestion, samples were cooled to room temperature. Nitric oxide and oxygen were vented to release the pressure in the cups by unscrewing the air vent slowly. The bomb contents were then transferred to acid-washed polyethylene bottles and diluted with ultra-pure water, followed by adding 100 μl of 10 μg/ml In solution (internal standard). It was necessary to add HF to the Teflon cups to digest the samples completely otherwise a small amount of black precipitate was formed in digested solutions.

6.3 Data acquisition

The prepared samples and standard solutions were aspirated into the ICP-MS and analyzed under the operating conditions summarized in Table 6.1.

The instrument was used in pulse counting mode to scan the analyzed solution in the mass range of 6 to 240 amu. The mass ranges of 11-23, 28- 45, and 55-56 and the mass of 80 were skipped since they corresponded to atomic

Table 6.1 PlasmaQuad operating parameters for analysis of wood samples.

Plasma	
Forward rf power	1350 W
Reflected rf power	< 2 W
Coolant flow (Ar)	13 L / min.
Nebulizer flow (Ar)	0.83 L / min.
Auxiliary flow (Ar)	0.9 L / min
Spray chamber temperature	controlled at 0.0±0.1 ^{o}C
Nebulizer, TR-30-A3	Meinhard concentric
Sample uptake rate	0.7 ml /min^{-1}.
Sampling depth	12 mm beyond the load coil
Mass spectrometer	
Sampler, Ni	1.0 mm orifice (Nicone)
Skimmer, Ni	0.75 mm orifice (Nicone)
Interface operating pressure	1.9 mbar
Analyzer pressure	2.5×10^{-6} mbar
Data acquisition	
Mass range (amu)	6-240
Skip mass or mass range (amu)	11-23, 28-45, 55-56, 80
Number of channels / amu	20
Number of scan sweeps	67
Dwell time (μs)	320
Acquisition time (s)	60.0
Collector type	Pulse
Integration method	valley

mass units of matrix elements and background ions. Temperature in the spray chamber was controlled at 0 ^{o}C by a water chiller to reduce the formation of oxide ions.

Prior to running samples, the instrument was warmed up for 20 minutes and then tuned with In at 115 amu to get maximum count rate. Many important parameters such as extraction potential, collector potential and sample uptake rate affect the count rate significantly. They were adjusted many times to obtain the best sensitivity of the instrument.

Some signal drift with time was observed for the instrument (see Chapter 5). Calibration was therefore carried out by alternating samples with standards and calculating the results by interpolation. The scheme used for the instrument was as follows: reagent blank (3 runs); 10 samples (2 runs); three external standards from low concentration to high concentration (3 runs); certified standards (3 runs); another 10 samples (2 runs); external standards (3 runs); certified standards (3 runs); etc. The uptake time for all solutions was 45 seconds, and rinsing and acquisition time were all 60 seconds. The injection of analyzed solutions was controlled by a Gilson 222 auto sampler.

6.4 Results and discussion

ICP-MS data for REEs NIST 1571 (orchard leaves) is shown in Table 6.2. With our experimental error, most REEs were within or very close to the range of the certified values.

Matrix effects were observed when NIST 1575 was analyzed. Two types of REE standards, with and without matrix elements added, were used to calibrate the concentrations of REEs in that certified sample. The measured

Table 6.2 Determination of REEs in NIST 1571 orchard leaves.

element	measured (n=2, ng/g)	certified (ng/g)
La	970±13	1170±110
Ce	821±24	990±120
Pr	161±2	84±26
Nd	606±40	510±130
Sm	96±11	114±20
Eu	22±1	24±3
Gd	101±6	88±48
Tb	11±1	13±3
Dy	53±3	82±23
Ho	11±2	16±5
Er	23±3	29.7±1.5
Tm	7±2	7±3
Yb	16±1	25±5
Lu	2±1	5.1±2.5

values of REEs in NIST 1575 are presented in Table 6.3. The concentrations of REEs (second column of the table) obtained from the matrix-containing standard are closer to the certified values than those (first column of the table) from the matrix-free standard. Without the matrix-matched standards, an average negative error, -16%, was produced in concentrations of REEs in NIST 1575. These negative errors were derived from the signal suppressions of REEs. If matched amounts of matrix elements are added to the standard, signals of REEs in sample and in standard are suppressed to the same degree thus eliminating or reducing the errors. This result is shown in Figure 6.2. The slope of the calibration curve from matrix-free standard is greater than that of matrix-matched standard. Lower concentration is thus obtained from the matrix-free calibration curve for any measured element in the sample.

Microwave digestion is an effective and efficient method for transforming solid biological samples into solution. Using the correct sample-to-acid(s) ratio, the dilution factor can be kept to a minimum and ICP-MS detection limits optimized. Detection limits based on a dilution factor of 40 were in the 40-100 ng/L range for the rare-earth elements.

Concentration results for Giant Sequoia and ponderosa pine (Tables 6.4 and 6.5, respectively) were obtained by matrix matched calibration. The concentrations of these elements against the years in which the wood was formed are plotted in Figures 6.3, 6.4 and 6.5.

The REEs showed the most dramatic change in concentration during 1828 in the ponderosa pine and 1592 in the Giant Sequoia as demonstrated by REE's chronology (Figures 6.4 and 6.3). We assume that these peaks represent a major change in environment such as a fire. These results are consistent with the concentration change of REEs measured in trees from

Table 6.3 ICP-MS and reference values (ng/g) for rare earths in pine needles (NIST 1575).

	measured by ICP-MS		Ref. [81]	Certified
	mean ± s.d. (n=5)		mean ± s.d.	mean ± s.d. (n)
	no matrix	with matrix		
La	95.7±2.6	110.0±1.9	116±4	160±40 (5)
Ce	192.4±6.2	213.2±1.0	166±22	210±50 (3)
Pr	23.3±1.0	26.3±1.0	26±6	< 70
Nd	87.9±5.1	100.3±2.8	118±13	164 (2)
Sm	17.9±1.0	20.0±1.7	23±4	20±2 (3)
Eu	3.5±0.2	4.7±0.4	ND	5.5±1.3 (3)
Gd	15.4±0.8	19.0±0.9	ND	28 (1)
Tb	2.2±0.1	2.6±0.3	ND	31 (2)
Dy	13.6±0.6	14.6±0.7	12±3	ND
Ho	2.4±0.4	2.8±0.2	5±2	ND
Er	6.6±0.5	8.3±0.6	15±6	ND
Tm	0.8±0.1	1.0±0.1	2±1	ND
Yb	5.3±0.4	6.6±0.3	18	17.5 (2)
Lu	0.7±0.1	1.0±0.1	2	1.6±0.6 (3)

ND — not detected

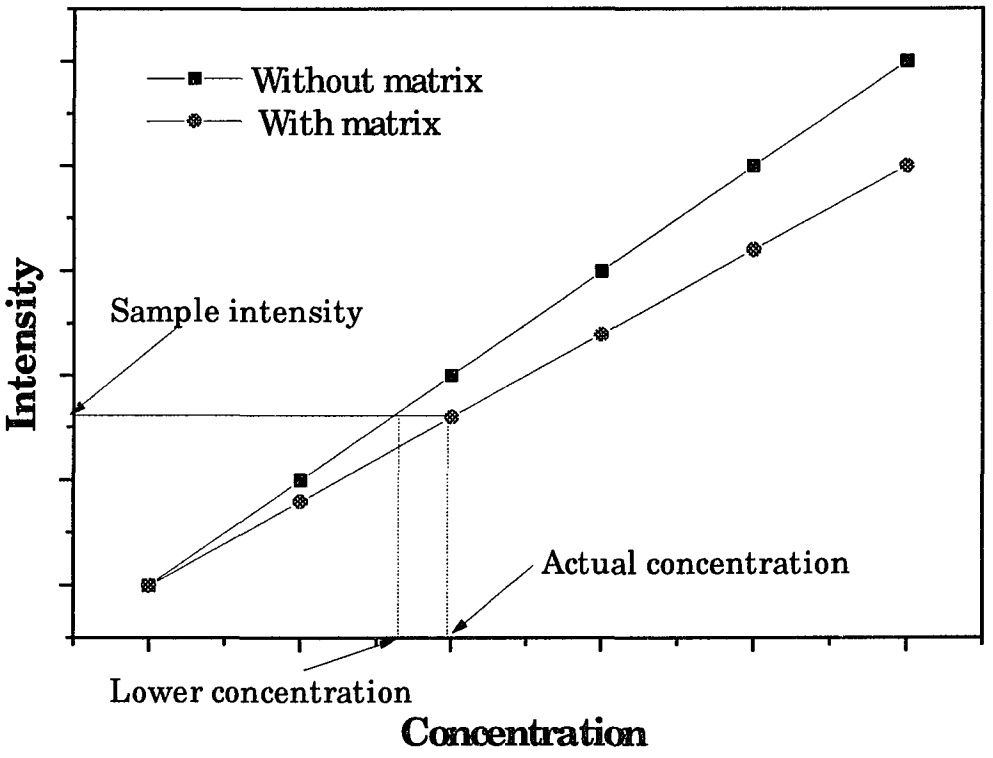

Figure 6.2 Simulated calibration curves from matrix matched and matrix free standards.

Table 6.4 Concentrations (μg/g) of some elements in tree rings of Giant Sequoia.

Year	La	Pr	Nd	Ba	Cu	Zn	Pb
1582	0.0832	0.0077	0.0257	32.7	0.679	1.82	0.157
1583	0.0814	0.0079	0.0227	33.1	0.873	2.25	0.186
1584	0.0870	0.0099	0.0288	31.9	0.919	2.03	0.247
1585	0.0816	0.0081	0.0230	31.1	0.89	2.99	0.183
1586	0.0904	0.0087	0.0255	34.4	0.901	2.53	0.166
1587	0.0805	0.0073	0.0244	33.0	1.94	2.80	0.284
1588	0.0920	0.0084	0.0246	34.8	0.818	2.11	0.148
1589	0.0819	0.0081	0.0231	33.0	0.796	2.42	0.243
1590	0.0849	0.0069	0.0191	32.7	0.765	2.51	0.112
1591	0.0739	0.0070	0.0206	29.0	0.606	1.81	0.178
1592	0.2640	0.0299	0.101	49.3	1.95	4.54	1.06
1593	0.0956	0.0116	0.0368	38.5	1.02	2.81	0.131
1594	0.0881	0.0090	0.0251	39.0	0.995	2.74	0.123
1595	0.0999	0.0115	0.0371	44.4	1.23	3.48	0.204
1596	0.101	0.0105	0.0331	42.6	1.04	3.00	0.493
1597	0.109	0.0129	0.0408	44.6	1.14	3.58	0.359
1598	0.125	0.0148	0.0483	47.4	1.4	3.78	0.120
1599	0.124	0.0130	0.0400	43.5	1.33	4.09	0.189
1600	0.105	0.0121	0.0358	42.2	1.19	3.90	0.130
1601	0.109	0.0145	0.0411	43.8	1.35	3.85	0.170
1602	0.133	0.0154	0.0458	47.9	1.59	4.53	0.203

Table 6.5 Concentrations of some elements in tree rings of ponderosa pine (concentration unit: bold style value, μg/g; regular style value ng/g).

year	La	Ce	Pr	Nd	Zn	Cu	Ba	Sr
1817	37.4	67.3	7.9	36.7	**1.33**	**0.79**	**1.60**	**1.77**
1818	35.6	52.1	6.9	30.5	**0.90**	**0.51**	**1.53**	**1.63**
1819	15.4	25.2	3.0	12.5	**1.10**	**0.37**	**1.56**	**1.59**
1820	17.6	34.2	3.5	12.9	**0.84**	**0.33**	**1.35**	**1.44**
1821	24.5	44.2	5.7	24.5	**0.99**	**0.29**	**1.26**	**1.54**
1822	11.7	20.7	2.0	8.9	**0.86**	**0.52**	**1.45**	**1.37**
1823	5.9	7.3	0.7	4.4	**0.95**	**0.42**	**1.36**	**1.36**
1824	17.9	31.2	5.0	15.3	**0.87**	**0.39**	**1.14**	**1.58**
1825	23.3	43.4	4.3	17.7	**1.13**	**0.96**	**1.40**	**1.51**
1826	16.7	30.2	3.4	14.8	**1.34**	**1.10**	**2.06**	**1.89**
1827	20.1	34.3	1.7	20.1	**0.85**	**0.73**	**1.52**	**1.48**
1828	**0.90**	**1.83**	**0.21**	**0.81**	**2.03**	**1.42**	**2.71**	**7.17**
1829	10.6	14.3	1.4	7.4	**1.11**	**0.66**	**1.34**	**1.30**
1830	7.0	9.1	1.7	0.7	**1.14**	**0.45**	**1.22**	**1.27**
1831	25.1	43.3	4.3	16.2	**1.03**	**0.65**	**1.26**	**1.48**
1832	9.4	9.0	0.9	3.6	**1.12**	**0.68**	**1.25**	**1.36**
1833	10.8	14.8	1.5	4.2	**1.60**	**0.77**	**1.38**	**1.55**
1834	8.2	6.9	0.8	4.4	**2.55**	**0.89**	**1.22**	**1.51**
1835	14.1	26.0	2.0	9.6	**1.80**	**1.18**	**1.17**	**1.44**
1836	11.8	16.2	2.0	6.2	**1.12**	**0.55**	**1.20**	**1.52**
1837	31.9	55.3	7.5	16.3	**3.19**	**1.78**	**1.22**	**1.52**
1838	14.8	21.9	2.1	6.9	**1.45**	**1.11**	**1.16**	**1.19**

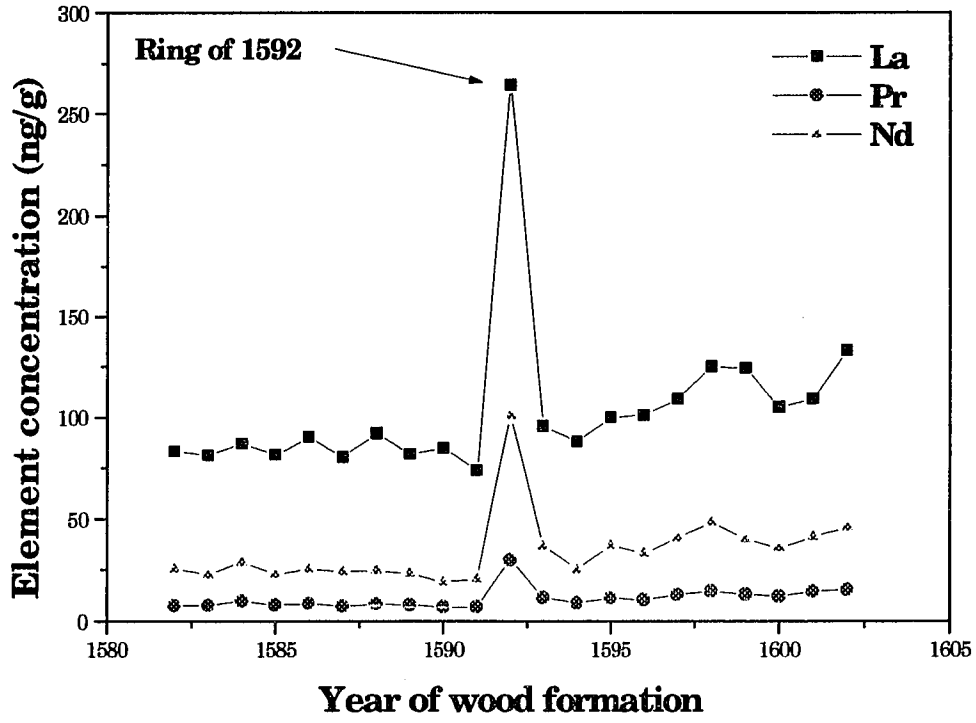

Figure 6.3 Variation of REE concentration in Giant Sequoia tree rings. The Tree-Ring Laboratory reported that the date of fire year was 1592, which is consistent with our result: high concentrations of REEs found in the ring of 1592.

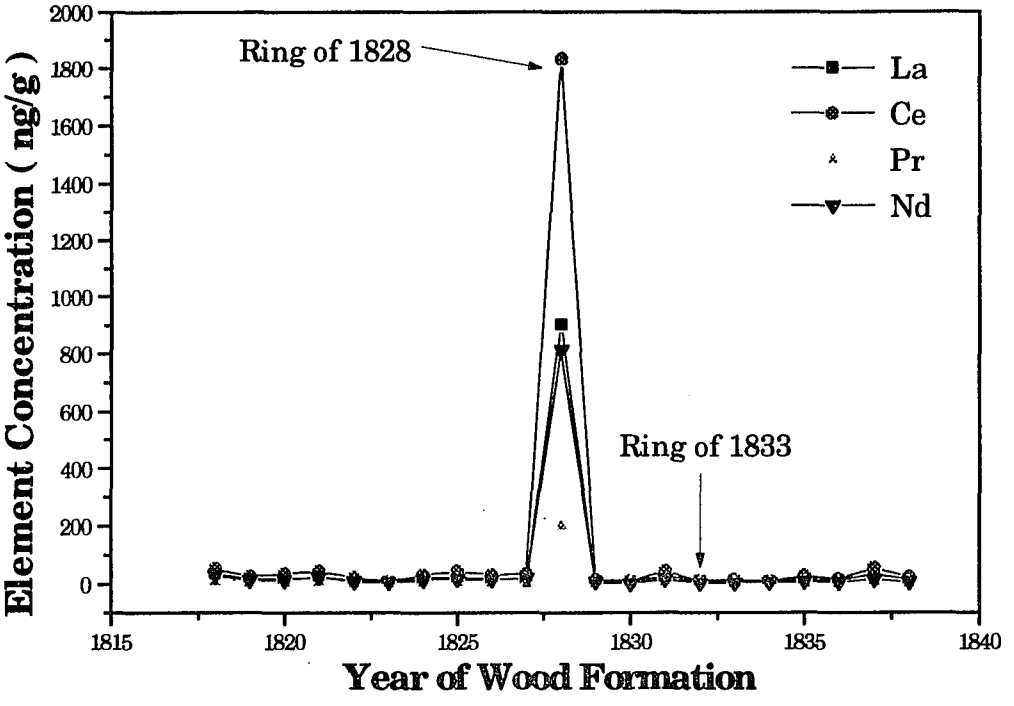

Figure 6.4 Variation of REE concentration in ponderosa pine tree rings. The Tree-Ring Laboratory reported that the fire year was 1833. But the peaks of the REE concentrations indicate the fire year of 1828.

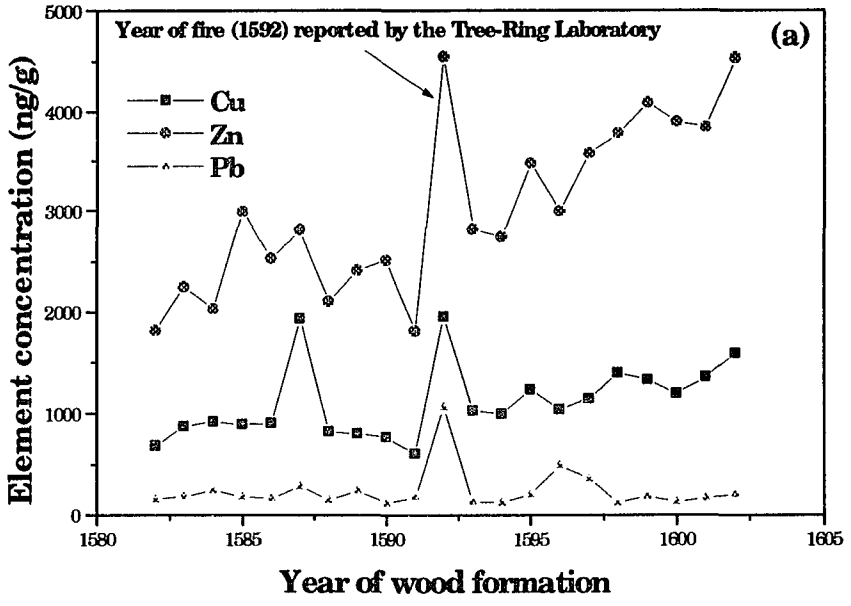

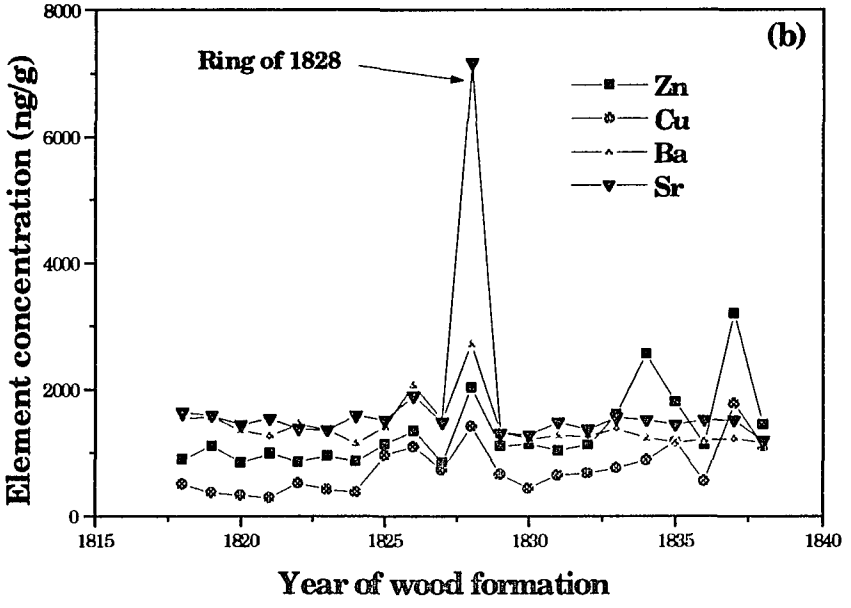

Figure 6.5 Concentration change of some elements in Giant Sequoia tree rings (Fig. a) and in ponderosa pine tree rings (Fig. b). The concentration of Cu and Zn in Sequoia did not decrease to the level before the fire year.

volcanic sites in other work [82]. After the fire, the concentrations of REEs returned to the pre-fire level (Fig. 6.4). The slightly higher concentrations of REEs (Fig. 6.3) after the fire year indicates that high concentrations of REEs in soil were still available for uptake. The sharp change in concentration suggests that the rare-earth elements do not translocate in the annual ring; otherwise a wide flat peak would be observed. Also, the concentrations suggest that REEs were leached from the soil faster than other elements noting that the relative concentrations of REEs in earth's crust are much lower than those of other elements. The transition elements show a similar change in concentrations but the peak in the fire year is not obvious (Ba and Zn in Figure 6.5). According to the report [83] by the Laboratory of Tree-Ring Research, the fire occurred in 1833 in the area where ponderosa pine grew. The sharp peak located at 1828 (see Figure 6.4) suggests that fire might have occurred in 1828. The Laboratory of Tree-Ring Research also reported that the date of the fire in the Sequoia area was 1592. The reported fire year was consistent with the high concentrations of REEs measured in the 1592 ring in the Sequoia sample.

Rare-earth elements are in low concentration in the soil relative to several other elements. They are easily taken up by the trees and incorporated into the wood. During a fire, vegetation is burned and many elements are concentrated in the ash or smoke particles. Upon weathering (rain, snow, wind etc.), elements become available for plant uptake and the cycle continues throughout the life of the forest. Unfortunately, we did not have soil samples from the forest fire sites. We could have analyzed the soils for REEs and determined if their concentrations in the tree rings were of the same relative proportions as those in the soils.

Rare-earth elements may be considered as elemental signatures that reflect a major change in environment in forests. Whether REEs concentration changes in tree rings can be used to date the years of fires must be proved by analyzing the concentrations of the elements in a few more trees from the fire sites.

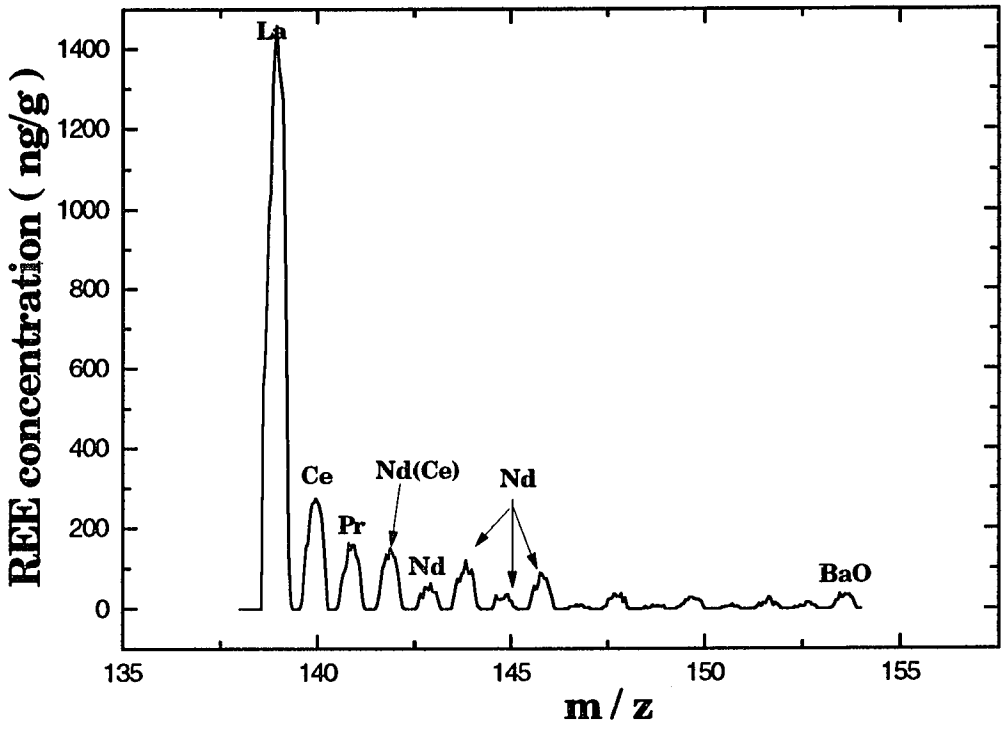

Figure 6.6 ICP mass spectrum of Giant Sequoia tree ring corresponding to the fire year (1592).

Chapter 7 Determination of lead concentration and its sources in drinking water

7.1 Statement of the problem

There are many ways for humans to take in lead unwittingly in their living environment. Drinking water, glass or pottery household utensils, and old paint are the common sources of lead. Lead is an element detrimental to human health. Infants and children under the age of 6 years are most susceptible to lead poisoning [84, 85]. Children can suffer mental retardation, lower performance on IQ tests, hyperactivity, and temporary loss of memory. It has been estimated [86] that about three million children in the United States are subjected to lead poisoning to a serious extent. Although all children are more vulnerable overall to the detrimental effects of lead in the body than are adults, too much lead stored in the skeletons of adults will cause high blood pressure and even lower reproductive ability. Severe exposure in adults causes irritability and sleeplessness. Lead in bone has a half-life of 30 years. An woman poisoned by Pb will affect her infant even a long time after exposure when she is pregnant.

The major route of lead absorption in the human body is via the gastrointestinal tract, with absorption being more efficient for children (50%) than for adults (8%) [84]. Harrison [87] reported that lead in tap water is more easily assimilated by the intestinal tract than lead in food stuffs, based on lead speciation in water and in the stomach.

With the reduction of lead in the environment due to its absence in gasoline and paint in recent years, and strict controlling of pottery imports came a concomitant increase in concern over low-level health effects by

ingestion of lead in drinking water. Numerous investigations have illuminated that the lead in tap water emanates from plumbing rather than source water [88, 89, 90, 91]. The leaching efficiency of lead from the plumbing fixtures depends on the content of Pb in plumbing system and on water quality characteristics such as pH, alkalinity and hardness. A survey of 107 old buildings by New York City Department of Environmental Protection early in 1992 found [92] that about 8% failed to meet the old federal standard for drinking water (50 ng/ml) and more than 35% did not meet the new stricter standard (15 ng/ml) effective in December 1992.

The objective of this experiment was to determine the concentration of Pb in drinking water collected from an old house in New York City and to determine, using isotope signatures and a mathematical model, which part of the plumbing system contributes to the majority of lead in the drinking water.

Lead has four stable isotopes: ^{204}Pb, ^{206}Pb, ^{207}Pb, and ^{208}Pb. Since ^{204}Pb is not radiogenic, its concentration on earth has remained constant since the formation of the earth. The other three isotopes ^{206}Pb, ^{207}Pb, and ^{208}Pb are radiogenic. ^{206}Pb is derived from the radioactive decay of ^{238}U, ^{207}Pb from ^{235}U, and ^{208}Pb from ^{232}Th. During Pb ore genesis, Pb is separated from its parent isotopes thereby fixing the isotope ratios in time. These Pb isotope ratios vary between geologic locations and depend on the age of the geological formation. The isotope ratios found in brass pipes and in lead pipe may vary depending on the sources of Pb from which these pipes were made. Thus the contribution of Pb from each part of the plumbing system can, in principle, be rationalized by measuring the isotope ratios of Pb in drinking water and comparing with the isotope ratios of Pb in the brass and the lead pipes.

7.2 Sample collection and preparation

The water samples were collected from Dean E. T. Williams' (one of my dissertation mentors) house located on Clinton Street, Brooklyn, New York. Two sets of samples were collected on different days. The first set of samples was collected in the early morning of March, 1992. The second set of samples was collected on the early morning of July 11, 1992. The house was built around 1845 and still has a lead pipe which connects the house to the city water main. The water pipes were not hidden in the ceiling and walls in the basement, making the measurement of pipe length easy. Figure 7.1 shows the flow diagram of water plumbing in the sampling site. Prior to collecting the water samples, nobody opened the taps or ran the water in the house for at least 8 hours.

The first set of samples was collected sequentially in 20 ml polyethylene bottles which had been washed with 6N HNO_3. The volume of water allowed to run in between samples was chosen to provide samples which had been sitting overnight in certain location in the pipes. We did not measure pH or temperature in this preliminary sample run.

The second set of water samples was collected in the following procedure: The basement tap was opened carefully and adjusted to give a suitable water flow rate. Once the water started running, the tap was kept open until sampling was completed; otherwise turbulent movement in the pipes could have mixed the water from different locations of the pipe(s). Twenty ml of water was collected in a small polyethylene vial (Wheaton) and then 250 ml or 500 ml of water was collected in a polyethylene bottle (Nalgene). The pH and temperature of the water collected in a big bottle were measured

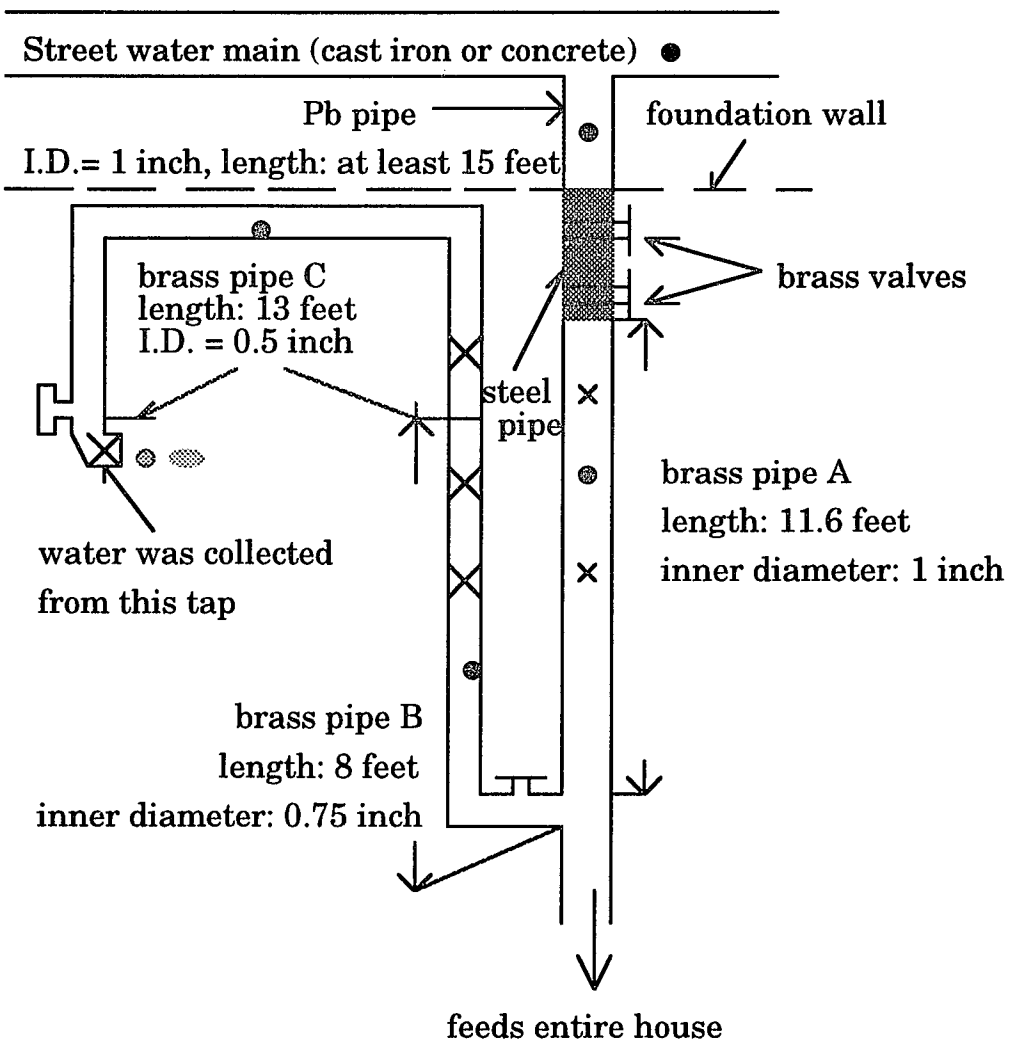

Figure 7.1 Flow diagram of water plumbing in ETW's basement.

× ------ indicates the locations where brass pipe samples were collected.

• ------ indicates the locations in the brass pipes, lead pipe, and water main from which water samples were collected in the preliminary run.

immediately using a digital handhold pH meter (Cole-Parmer Instrument Company) and then discarded. The cycle was repeated 30 times consecutively. During the sampling, we tried to minimize water loss as best as we could. After sampling, the water samples collected in small vials were carried to our laboratory immediately and spiked with 0.1 ml of J. T. Baker Ultrex concentrated HNO_3. All polyethylene vials and bottles were washed with 6 N HNO_3 before use.

The lead pipe where it emerged from the foundation wall was sampled by scraping with a stainless steel knife. Using a triangular file, brass was sampled from different locations of the brass pipes and from the faucet as shown in Figure 7.1. The surfaces of the brass pipes were filed to remove dust and paint before they were sampled.

In the laboratory, the brass filings were weighed accurately in a mass-tared polyethylene bottle. The sample was then dissolved in 2 ml of 6N HNO_3 and diluted to the volume with a suitable dilution factor.

The lead pipe sample was prepared by dissolving it in 6N HNO_3 and was diluted to the volume corresponding to about 25 ppb Pb. This solution was only used for determination of Pb isotope ratios.

In order to know how much Pb the water in water mains contains and what the $^{206}Pb/^{207}Pb$ ratio is, we also collected water samples from several fire hydrants in the following locations:

230 Clinton Street, Downtown Manhattan

233 Clinton Street, Brooklyn

326 Clinton Street, Brooklyn

143-15 Rose Avenue, Flushing Queens

43-37 156 Street, Flushing Queens

The fire hydrant was opened with a special wrench. After the water ran for 10 minutes, it was collected with a 20 ml or 100 ml polyethylene bottle. The collected water samples were immediately spiked with 0.1 ml HNO_3 to prevent Pb from being adsorbed by the bottles.

Both water samples from ETW's for the second run and from the fire hydrants and brass pipe samples were spiked with Tl as an internal standard before analysis.

The first set of samples represented five locations of water in the brass pipes A, B, and C, samples from Pb pipe, and water main. The sample size for each location was 20 ml. These samples were used for preliminary testing.

To examine how far the lead leached from the Pb pipe can diffuse toward the brass pipes axially, diffusion test solutions were prepared. A 7.61-feet (232 cm), 1.5-cm inner diameter of PVC (polyvinyl chloride) pipe with one end stopped was filled with deionized water. One milliliter of 11.5 ppm NIST 981 common lead solution was spiked into the pipe from the other end. The pipe was then stopped by a rubber stopper and placed horizontally. After 6 days, the solution in the pipe was withdrawn from the end opposite to the end with the lead spike by a pneumatic pump and received in 35-ml polyethylene vials. After each tube was full, the tubing inserted into the pipe was pushed a little deeper and next portion of sample was continued to be received. The sampling method chosen was to avoid turbulence in the pipe. The sampled water from the pipe was also spiked with Tl as an internal standard.

7.3 Instrument optimization and sample analysis

7.3.1 Instrument optimization

The determination of lead sources is based on the measurement of isotope ratios of lead from lead pipe, brass pipes, and drinking water. It was found that the precision of lead isotope ratio measurement was affected by operating conditions of the instrument to a certain extent. Therefore, the instrument had to be optimized to obtain the best precision for the measurement.

The precision test was performed by running a set of lead standard solutions (SPEX) under different operating conditions. The result of the test is shown in Table 7.1.

The result of the optimization test suggested that the higher the concentration of lead, the better the precision for the isotope ratio in both peak jump mode and scan mode. Strictly speaking, we should say the higher the count rate, the better precision we have because sometimes the count rate of 25 ppb Pb was higher than that of 50 ppb Pb run on the different day depending on the instrument tuning. When dwell time was fixed, channel numbers per amu did not affect the precision of the ratio too much at higher Pb concentrations (50 ppb and 100 ppb); however, higher channel numbers per amu provided better precision at lower Pb concentration. On the other hand, the effect of the dwell time on precision was concentration dependent when channel numbers per amu was constant. In most of our subsequent experiments, 40 channel per amu and 160 μs dwell time were thus used for Pb analysis.

Table 7.1 also showed that the ^{206}Pb / ^{207}Pb ratios measured with peak jump mode were slightly lower than those with scan mode. Probably the

Table 7.1 Optimization test for isotope ratio of $^{206}Pb/^{207}Pb$.

dwell time	mode used	1ppb	10ppb	25ppb	50ppb	100ppb
160μs	scan, A	1.210(8.54)	1.218(2.00)	1.201(0.35)	1.219(0.56)	1.204(0.12)
320μs	scan, A	1.224(6.32)	1.208(0.99)	1.219(0.61)	1.208(0.15)	1.208(0.44)
160μs	scan, B	1.235(3.92)	1.214(1.96)	1.209(0.09)	1.202(0.53)	1.206(0.12)
320μs	scan, B	1.177(6.34)	1.192(0.53)	1.207(0.85)	1.207(0.18)	1.196(0.44)
1000μs	peak jump	1.092(44.3)	1.206(1.34)	1.188(0.75)	1.196(0.58)	1.197(0.50)

Scan, A -------- number of channel per amu = 20;

Scan, B -------- number of channel per amu = 40;

The values in parentheses indicate %RSD.

degree of mass discrimination effect are different in the two modes. Since NIST 981 Pb standard solution was run along with samples in each experiment, the Pb isotope ratios could be normalized to correct values by the standard.

7.3.2 Effect of acids on sensitivity and precision of lead analysis

The first set of water samples were spiked with 25 ppb Tl. No acid was added to these samples. The samples were analyzed using scan mode with scan range from 200 amu to 210 amu. Dwell time and channel number per amu were 160 μs and 40 respectively. Each sample was run three times.

Unfortunately, the following problems were observed: 1) peak shapes of ^{206}Pb, ^{207}Pb, and ^{208}Pb were not smooth and split into smaller sharp peaks; 2) the reproducibility of count rates of these isotopes was poor and thus the relative standard deviation of ^{206}Pb / ^{207}Pb ratios varied from 3% to 17%; and 3) the analog detector light was on though the concentration of Pb was not very high (normally if the analog detector light is on, it indicates that the concentration of some element whose mass is in the scan mass range is too high).

Because of poor reproducibility of the count rates of ^{206}Pb and ^{207}Pb, the concentrations of Pb and ^{206}Pb / ^{207}Pb ratio could not be determined accurately. We repeated the analysis of the water samples after adding HNO_3. The spectra of the same water sample with and without HNO_3 added are shown in Figure 7.2b and Figure 7.2a, respectively. Figure 7.2b shows that the Pb peak shapes of the acidified sample were improved dramatically. The relative standard deviation of ^{206}Pb /^{207}Pb ratio became much better (below 0.7%). The reproducibility of count rates also improved.

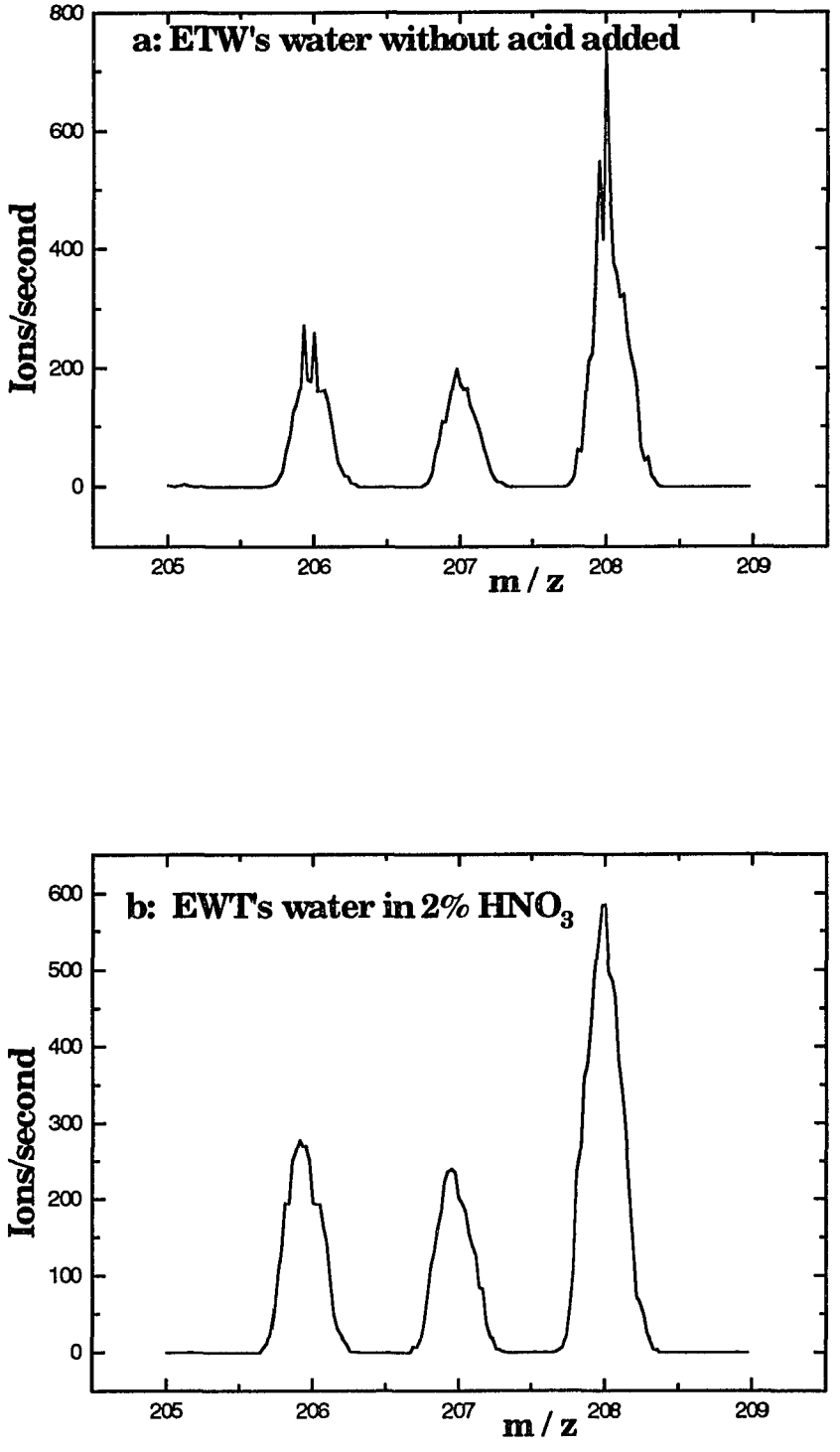

Figure 7.2 Spectra of ETW's drinking water collected from Brooklyn, New York.

The drinking water from Flushing New York has the same characteristics. We collected some water from a house located on 43-47 156 Street, Flushing, New York. The samples were treated and run in the same manner as ETW's water. Figure 7.3 shows the Pb spectra of the water collected from Flushing, New York.

Now the question is, what caused the Pb peak shapes to split and the relative standard deviation of Pb isotope ratio to be poor? The drinking water for New York City is chlorinated with Cl_2 to kill bacteria in the summer and NaOH is added to adjust the pH. The pH values of the drinking water we collected varied from 6.6 to 7.2 (see Table 7.6). Normal doses of Cl_2 added to drinking water vary from 10 to 20 mg/L [93]. We thought two suspected factors, ClO^- and pH value, might cause the problems. Therefore, the simulated drinking water was prepared and analyzed to test our hypothesis.

We thus prepared 250 mg/L of NaClO solution by diluting Clorox bleach solution containing 5.25% NaClO with ultra-pure water. The diluted NaClO solution was used to prepare 10 ppm NaClO solution containing 28 ppb Pb, and 10 ppm NaClO solution containing 28 ppb Pb and 2% HNO_3. These solutions were run in the same conditions as ETW's water samples using 10 ppm NaClO solution (pH=7.0) as a blank. The spectra of the simulated drinking water are shown in Figure 7.4. The distorted peak shapes in the spectrum of 28 ppb Pb solution in NaClO matrix (Figure 7.4a) are similar to those in Figure 7.2a. The spectrum was improved by acidifying the simulated drinking water with HNO_3 and the precision (RSD%) of ^{206}Pb / ^{207}Pb ratio improved from 9.4% to 0.77%.

We also prepared 23 ppb SPEX2 solution (containing Pb) whose pH was adjusted to 7.0 with 0.001 M NH_3 (Fisher). This solution and a 23 ppb SPEX2 solution in 2% HNO_3 were run in the similar condition to the Pb

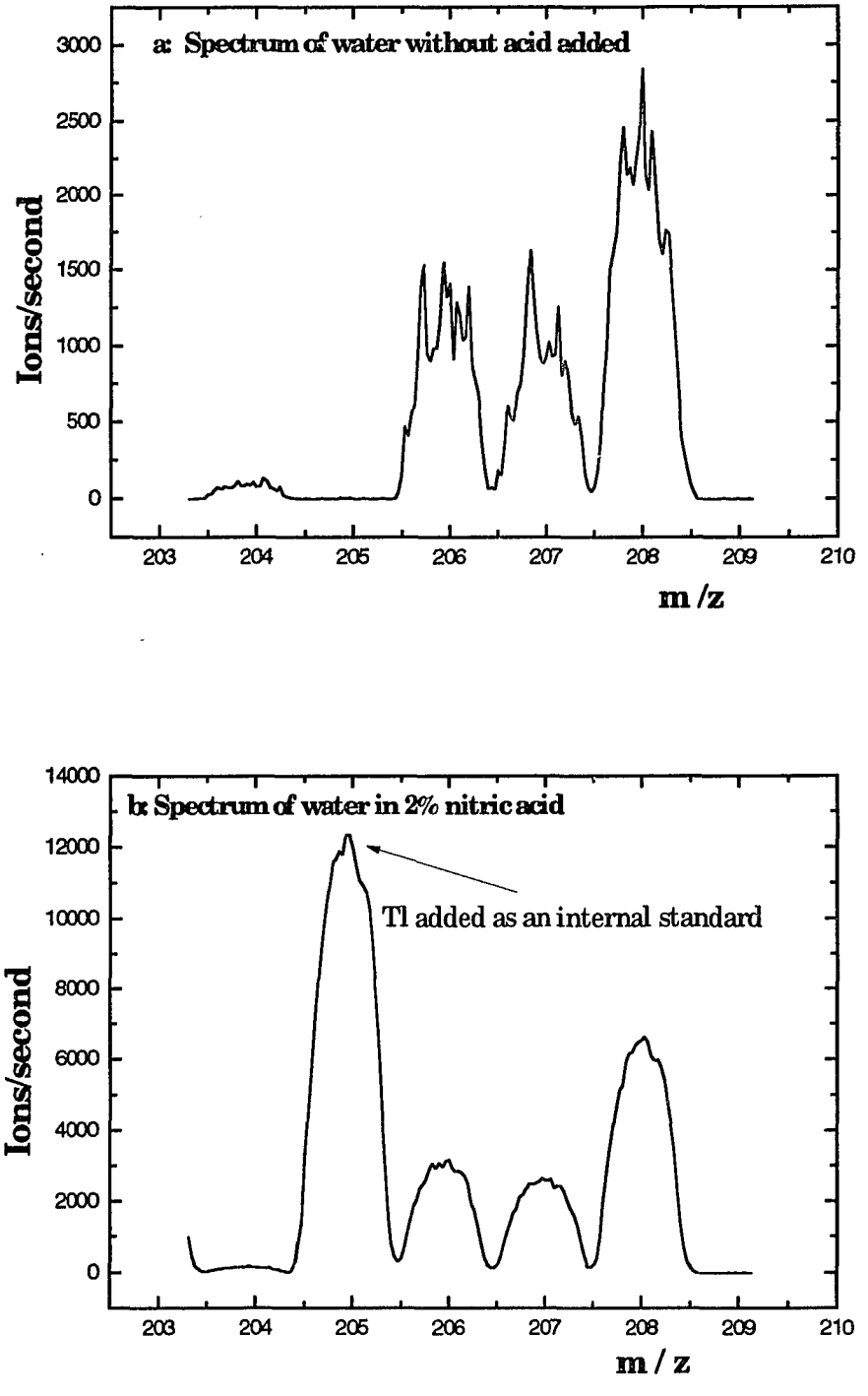

Figure 7.3 Spectra of drinking water collected from Flushing, New York.

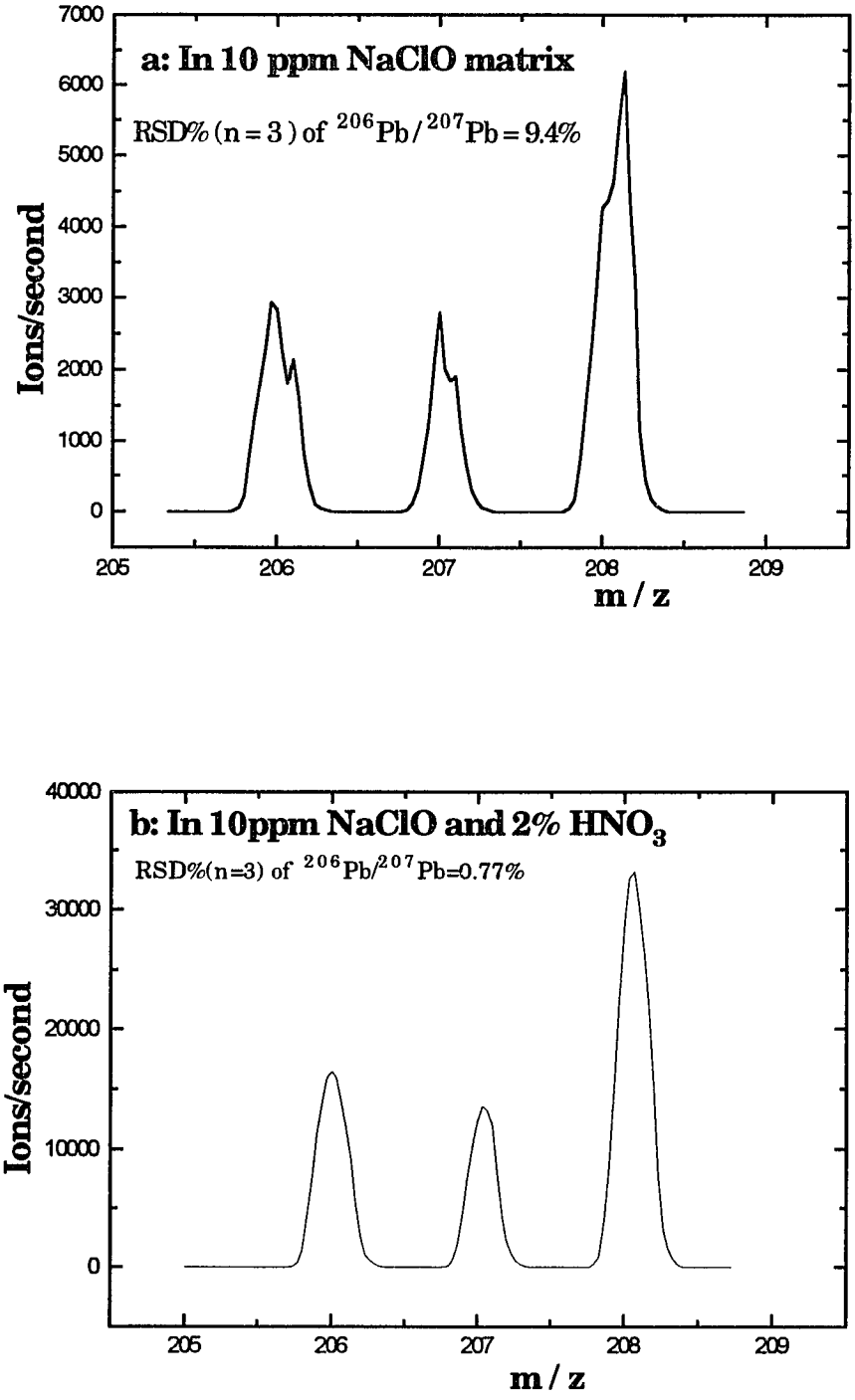

Figure 7.4 ICP-MS spectra of 28 ppb Pb solutions in NaClO matrix.

solution in NaClO matrix. The spectra are shown in Figure 7.5. The peaks of ^{206}Pb, ^{207}Pb, ^{208}Pb and even ^{209}Bi (SPEX2 also contains Bi and Tl) in the spectrum of the SPEX2 solution in NH_3 matrix split into small peaks. Contrary, the corresponding peak shapes in the spectrum from SPEX2 solution in 2% HNO_3 improved.

The above experiment indicated that slightly alkaline or neutral medium, not ClO^- or HClO medium, distort the peak shapes of Pb and deteriorate the precision and accuracy of Pb analysis. The mechanism of distortion of Pb peak shapes by alkaline or neutral medium has not been understood so far.

From Figure 7.3, we found that addition of HNO_3 to drinking water not only improves the precision and accuracy but also the sensitivity. The sensitivity, represented by ions (counts) per second, increased by a factor of 2 to 3. To investigate whether other acids have the similar effect, we performed the following experiment:

ETW's drinking water was spiked with different acids (Fisher) to give an acid concentration in the Pb solutions of 0.3 M. The Pb solutions without acids added were used as references. All prepared solutions were run in the sequence as follows: reference Pb solution; acidified Pb solution; reference Pb solution; another acidified Pb solution; etc. The reference Pb solution was repeated running several times to monitor instrument drift. The relative sensitivities, ratios of ^{208}Pb count rate of acidified solutions to the reference solution, are shown in Table 7.2. After acid was added to drinking water the count rate of Pb increased. But the degrees of increase were dependent on the varieties of acid. In general, the acids enhance the Pb count rate in the order of $HCl < HClO_4 < H_2SO_4 < HNO_3 < H_3PO_4$. $HClO_4$, H_2SO_4, and H_3PO_4 also improved the peak shapes of ^{206}Pb, ^{207}Pb, and ^{208}Pb.

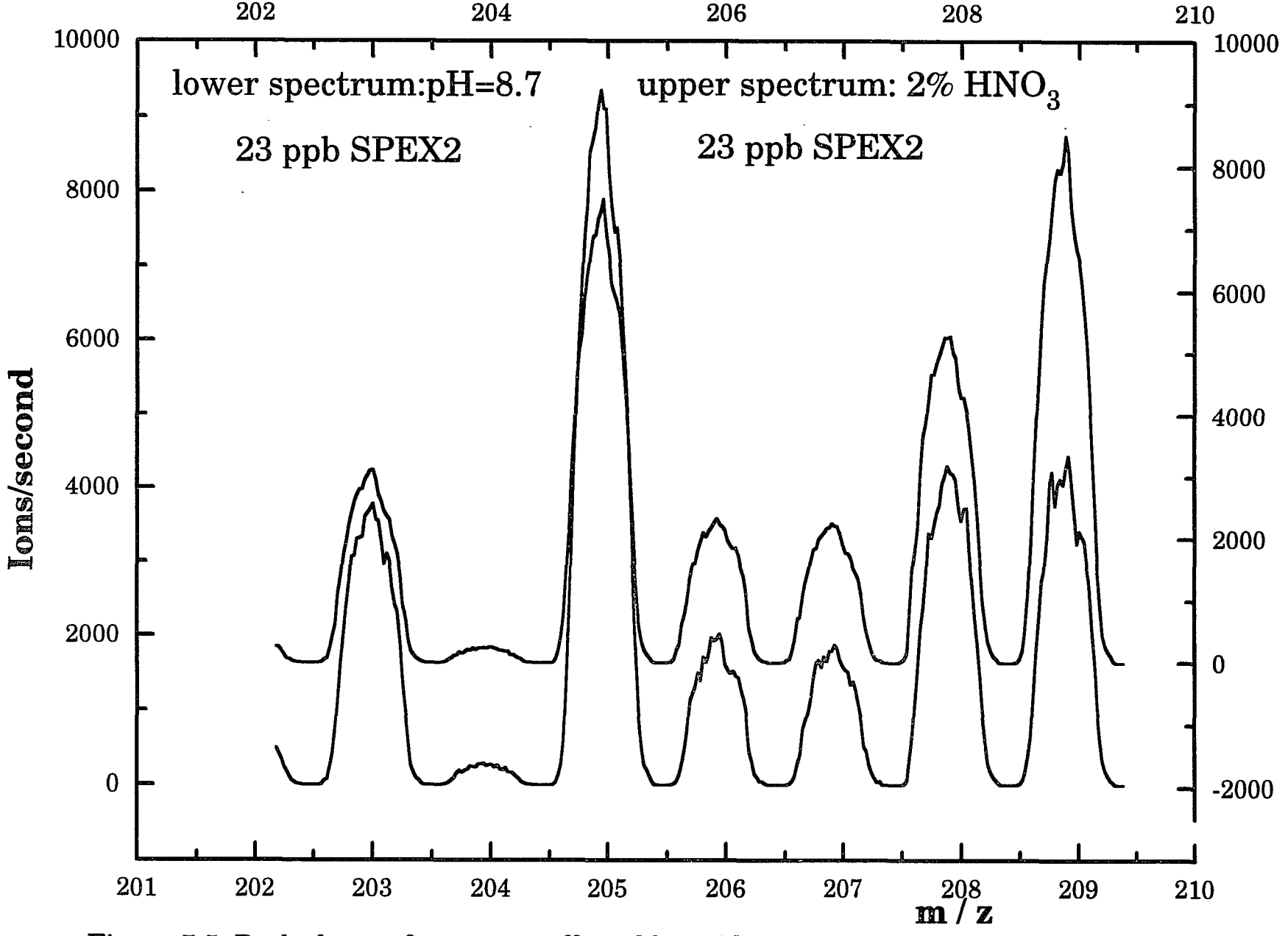

Figure 7.5 Peak shape of spectrum affected by acidity.
The scale on the right is for the acidified solution.

Table 7.2 Relative sensitivity of Pb determination in different acid matrixes*.

Test solution	count rate (^{208}Pb, in acid) / count rate (^{208}Pb, in H_2O)				
	HCl	$HClO_4$	H_2SO_4	HNO_3	H_3PO_4
ETW's water	1.41	1.55	2.13	2.40	2.52

* ---- all acids added are adjusted to 0.3 M.

According to this experiment, acid, preferably HNO_3, must be added to drinking water to increase the sensitivity of the instrument for Pb analysis. Though H_3PO_4 can increase the count rate of Pb most, high concentrations of H_3PO_4 also produce isobaric interferences as stated in Chapter 4 when other elements are being analyzed simultaneously.

Since the sensitivity of the instrument doubled when HNO_3 was added to drinking water, the second set of ETW's water samples were spiked with HNO_3. The acid content in each sample was 2%. The samples were run twice. In the first run, the water samples along with brass pipe and Pb pipe samples were analyzed to determine concentrations and isotope ratios of Pb. The operating conditions for the first run are summarized in Table 7.3. The water samples were run one more time to determine multielemental concentrations using the operating parameters similar to the ones shown in Table 6.1.

7.3.3 The mechanism of enhancement in lead signal by acids

Lead signal is enhanced in acidic medium relative to that in slightly alkaline or neutral medium. This phenomenon is probably due to the hydrogen ions reacting with conjugate bases of weak acids in drinking water.

Drinking water contains trace amount of humic substances which are made up of fulvic and humic acid that originate from degradation of plant matter [94]. The concentration of humic substances in drinking water from lakes or rivers varies from 1.0 to 4.0 mg/L [93]. Generally, the fulvic acid is more water soluble, because it contains more carboxylic and hydroxyl functional groups and is lower in molecular weight, from 800 to 2000. Humic acid is larger than 2000 molecular weight and is often colloidal in size [94]. Dissolved humic substances comprise 5% - 10% of all anions in streams and

Table 7.3 PlasmaQuad operating parameters for analysis of drinking water.

Plasma	1350 W
Reflected rf power	< 2 W
Coolant flow (Ar)	13 L / min.
Nebulizer flow (Ar)	0.83 L / min.
Auxiliary flow (Ar)	0.9 L / min.
Spray chamber temperature	controlled at 0.0 ± 0.1°C
Nebulizer, TR-30-A3	Meinhard concentric
Sample uptake rate	0.7 ml/min.
Sampling depth	12 mm beyond the load coil
Mass spectrometer	
Sampler, Ni	1.0 mm orifice (Nicone)
Skimmer, Ni	0.75 mm orifice (Nicone)
Interface operating pressure	1.9 mbar
Analyzer pressure	2.5×10^{-6} mbar
Data acquisition	
Mass range (amu)	200 - 210
Number of channels / amu	40
Number of scan sweeps	500
Dwell time (μs)	160
Acquisition time (s)	60.0
Collector type	Pulse
Integration method	valley

rivers. The anionic character of the humic substances come from the dissociation of carboxylic-acid functional groups:

$$R—COOH \rightleftharpoons R—COO^- + H^+$$

Carboxyl functional groups occur on aquatic humic substances with a frequency of 5-10 per molecule, and at the pH of most natural waters, pH 6-8, all of these carboxyl groups are dissociated. The counter-ions balancing the charge for these negative groups are mostly calcium and sodium. However, trace metals may be bound to some of these carboxyl groups and phenolic groups that have a favorable steric location. That is, a carboxyl group in association with a phenolic group may form a chelate, or ring structure, and bind metal ions such as lead ions. The pH values of drinking water we collected are in the range of 6.8 to 7.2. At this pH range, the carboxylic groups in humic substances form coordinate complexes with lead ions. The formation of Pb-carboxyl group complexing ions may decrease the aerosol transport efficiency of lead due to a decrease in the fraction of droplets of less than 10 μm. It results in a decrease in the percentage of the mass of Pb that actually reaches the plasma, and thus a decrease in lead count rate. When an acid is added to drinking water, the following equilibra shift to the left side thus increasing the concentration of free lead ions. So, the aerosol transport efficiency of Pb increases and lead signal is enhanced.

$$Pb^{2+} + n\,(R—COO^-) \rightleftharpoons [Pb(R—COO)_n]^{-(n-2)}$$

$$R—COOH \rightleftharpoons R—COO^- + H^+$$

If lead signal were enhanced only by H^+ ions, the extent to which the lead signal is enhanced would be the same no matter what type of acid is added to drinking water as long as the concentration of H^+ ions is the same. However, as indicated by Table 7.2, the effect of acids on the lead signal are not the same. The lead signal was enhanced by 0.3 M HNO_3 more than by 0.3 M HCl. There must be an alternative mechanism by which the lead signal is increased. Probably a charge-transfer effect also causes an increase in the lead signal.

Elements and molecules can be ionized in the plasma by different ionization process, as stated in Chapter 2. One of the processes is called charge transfer. The interaction of analyte species with argon may occur through this process:

$$Ar^+ + X \longrightarrow X^+ + Ar + \Delta E$$

where ΔE is the difference between the argon ionization energy and ionization energy of X. In our experiment Pb is the analyte species and an acid is used as a solvent. Charge transfer may occur between the species from a solvent and Pb in the similar process. If HNO_3 is the solvent, this process might be represented as

$$NO^+(X\ ^1\Sigma^+) + Pb\ (6p^2,\ ^3P_0) \longrightarrow Pb^+(6p,\ ^2P_{1/2}) + NO(\ X\ ^2\Pi) + \Delta E\ (1.89\ eV)$$

where NO^+ ion comes from dissociation and then ionization of HNO_3. The charge-transfer process is advantageous to the formation of Pb^+ and in sequence enhances the lead signal in the instrument. Other ions, such as ClO^+, SO^+, and PO^+ which originate from $HClO_4$, H_2SO_4, and H_3PO_4 also

help to increase lead signal by a charge transfer process. However, according to Rutherford *et al.* [95] and Goldwasser *et al.* [96], the rate of charge transfer process depends on the energy defect (ΔE). The smaller the energy defect the larger the cross section and the greater the reaction rate. Table 7.4 shows the ionization potentials of Pb and the polyatomic species of interest. The energy defects between polyatomic species and Pb become smaller from Cl^- to PO^+. The change of the energy defects explains why lead count rate is enhanced by acids in the order of $HCl < HClO_4 < H_2SO_4 < HNO_3 < H_3PO_4$.

The hypothetical mechanism of enhancement in the lead signal by these mineral acids is: 1) the hydrogen ions from the acid decrease the concentration of anionic forms of humic substances and release Pb ions; 2) the conjugate base of the acids provide ions for charge transfer reaction in plasma.

7.4 Mathematical model used to find lead sources

Lead in drinking water may originate from different sources: lead pipe, brass pipe, solder etc. Consider the two-component mixture of Pb as shown in Figure 7.6.

The lead in the plumbing system comes from Pb pipe with volume V_1 and brass pipe with volume V_2 in terms of extraction by water. The concentrations of Pb leached from Pb pipe and brass pipe are C_{Pb1} and C_{Pb2}, respectively. After mixing, the total concentration of Pb is expressed by:

$$C_M = C_{Pb1} \times f + C_{Pb2} \times (1- f) \qquad (7.1)$$

where $f = V_1/(V_1+ V_2)$.

Table 7.4 Ionization potentials (I. P.) of lead and some polyatomic species.

species (ground state)	ground ionic state and I. P. (eV)		references
Pb ($6p^2$, $^3P_0$)	($6p$, $^2P_{1/2}$)	7.3	[97]
Cl ($3p^5$, $^2P_{3/2}$)	($3p^4$, $^3P_2$)	12.96	[97]
ClO (X $^2\Pi$)	(X $^1\Sigma^+$)	11.0	[98]
SO (X $^3\Sigma^-$)	(X $^2\Pi$)	10.29	[98]
NO (X $^2\Pi$)	(X $^1\Sigma^+$)	9.27	[98]
PO (X $^2\Pi$)	(X $^1\Sigma^+$)	8.23	[98]

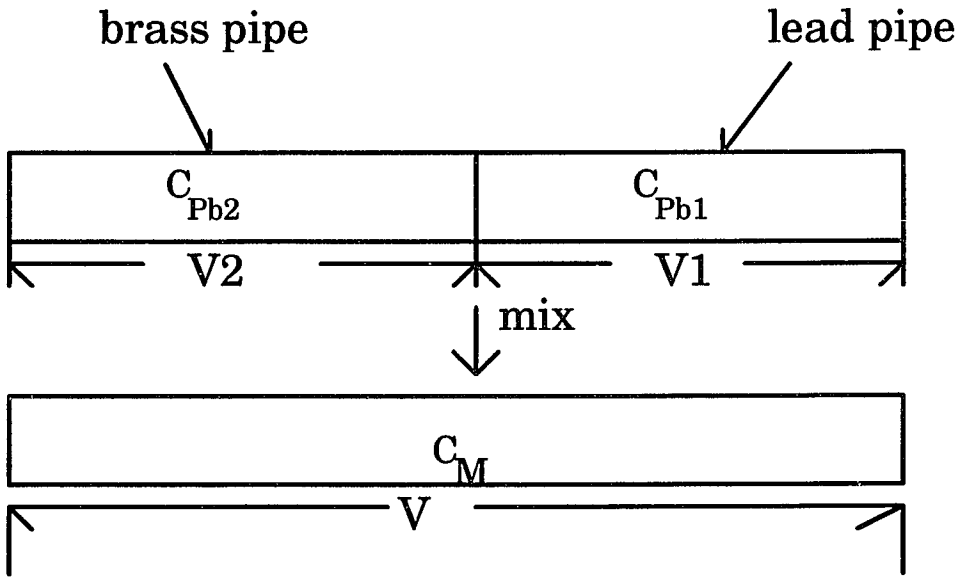

Figure 7.6 Illustration of two-component mixture of Pb.

The $^{206}Pb/^{207}Pb$ ratio in the mixture (M) is [99]:

$$\left\{\frac{^{206}Pb}{^{207}Pb}\right\}_M = \frac{C_{Pb1} \times Ab_1^{206} \times f \times W1 + C_{Pb2} \times Ab_2^{206} \times (1-f) \times W2}{C_{Pb1} \times Ab_1^{207} \times f \times W1 + C_{Pb2} \times Ab_2^{207} \times (1-f) \times W2} \quad (7.2)$$

where Ab_1^{206} and Ab_1^{207} are the isotope abundances of Pb in Pb pipe, Ab_2^{206} and Ab_2^{207} are the isotope abundances of Pb in brass pipe, and W1 and W2 are the atomic weights of Pb in Pb pipe and brass pipe, respectively. If the abundances of ^{207}Pb are not too different and W1 is close enough to W2, Equation 7.2 reduces to:

$$\left\{\frac{^{206}Pb}{^{207}Pb}\right\}_M = \frac{C_{Pb1} \times Ab_1^{206} \times f + C_{Pb2} \times Ab_2^{206} \times (1-f)}{Ab^{207} \times \{C_{Pb1} \times f + C_{Pb2} \times (1-f)\}} \quad (7.3)$$

Setting $Ab_1^{206}/Ab^{207} = (^{206}Pb/^{207}Pb)_1$, $Ab_2^{206}/Ab^{207} = (^{206}Pb/^{207}Pb)_2$, and by making use of Equation 7.1 to eliminate f from Equation 7.3, this equation becomes:

$$\left\{\frac{^{206}Pb}{^{207}Pb}\right\}_M = \frac{C_{Pb1} \times C_{Pb2} \{(^{206}Pb/^{207}Pb)_2 - (^{206}Pb/^{207}Pb)_1\}}{C_M \times (C_{Pb1} - C_{Pb2})} + \frac{C_{Pb1}(^{206}Pb/^{207}Pb)_1 - C_{Pb2}(^{206}Pb/^{207}Pb)_2}{C_{Pb1} - C_{Pb2}} \quad (7.4)$$

This is the equation of a hyperbola in coordinates of $(^{206}Pb / ^{207}Pb)_M$ and C_M of the form:

$$\left\{\frac{^{206}Pb}{^{207}Pb}\right\}_M = \frac{a}{C_M} + b \qquad (7.5)$$

where a and b are constants specified by the concentrations and $^{206}Pb/^{207}Pb$ ratios of lead in lead pipe and brass pipe as shown in Equation 7.4.

With Equations 7.4 and 7.5 or Equation 7.2 we can calculate the concentrations of Pb leached from brass pipe and Pb pipe. To examine the validity of these equations, we did a simulated experiment by using 49.62 ppb Pb from SPEX standard and 26.03 ppb Pb from SPEX2 standard to represent the concentrations of Pb leached from Pb pipe and brass pipe, respectively. We prepared lead mixtures from 49.62 ppb SPEX and 26.03 ppb SPEX2 by mixing these solutions in different mass ratios. The experimental data are shown in Table 7.5.

When $(^{206}Pb/^{207}Pb)_M$ versus $1/C_M$ from Table 7.5 is plotted in Figure 7.7, a straight line is obtained. The slope and intercept on vertical axis are minus 6.819 and 1.3065, respectively. Substituting these values and $^{206}Pb/^{207}Pb$ ratios of SPEX and SPEX2 into the corresponding terms in Equations 7.4 and 7.5, we have:

$$-6.819 = \frac{C_{Pb1} \times C_{Pb2}\,(1.0375 - 1.1662)}{C_{Pb1} - C_{Pb2}} \qquad (7.6)$$

$$1.3065 = \frac{C_{Pb1} \times 1.1662 - C_{Pb2} \times 1.0375}{C_{Pb1} - C_{Pb2}} \qquad (7.7)$$

The values of C_{Pb1} and C_{Pb2} are obtained by solving Equations 7.6 and 7.7. These values are 48.60 ppb and 25.35 ppb which correspond to original

Table 7.5 Data obtained from mixing Pb experiment*.

sample conc., C_M	component	$^{206}Pb/^{207}Pb$	Ab^{206}	Ab^{207}
26.03 ppb	SPEX2,100%	1.0375	0.2349	0.2235
49.62 ppb	SPEX, 100%	1.1662	0.2505	0.2148
45.00 ppb	SPEX, 80.41%	1.1558		
40.38 ppb	SPEX, 60.82%	1.1356		
35.34 ppb	SPEX, 39.46%	1.1153		
30.55ppb	SPEX, 19.18%	1.0828		

* abundances and isotope ratios have been corrected by NIST 981 standard.

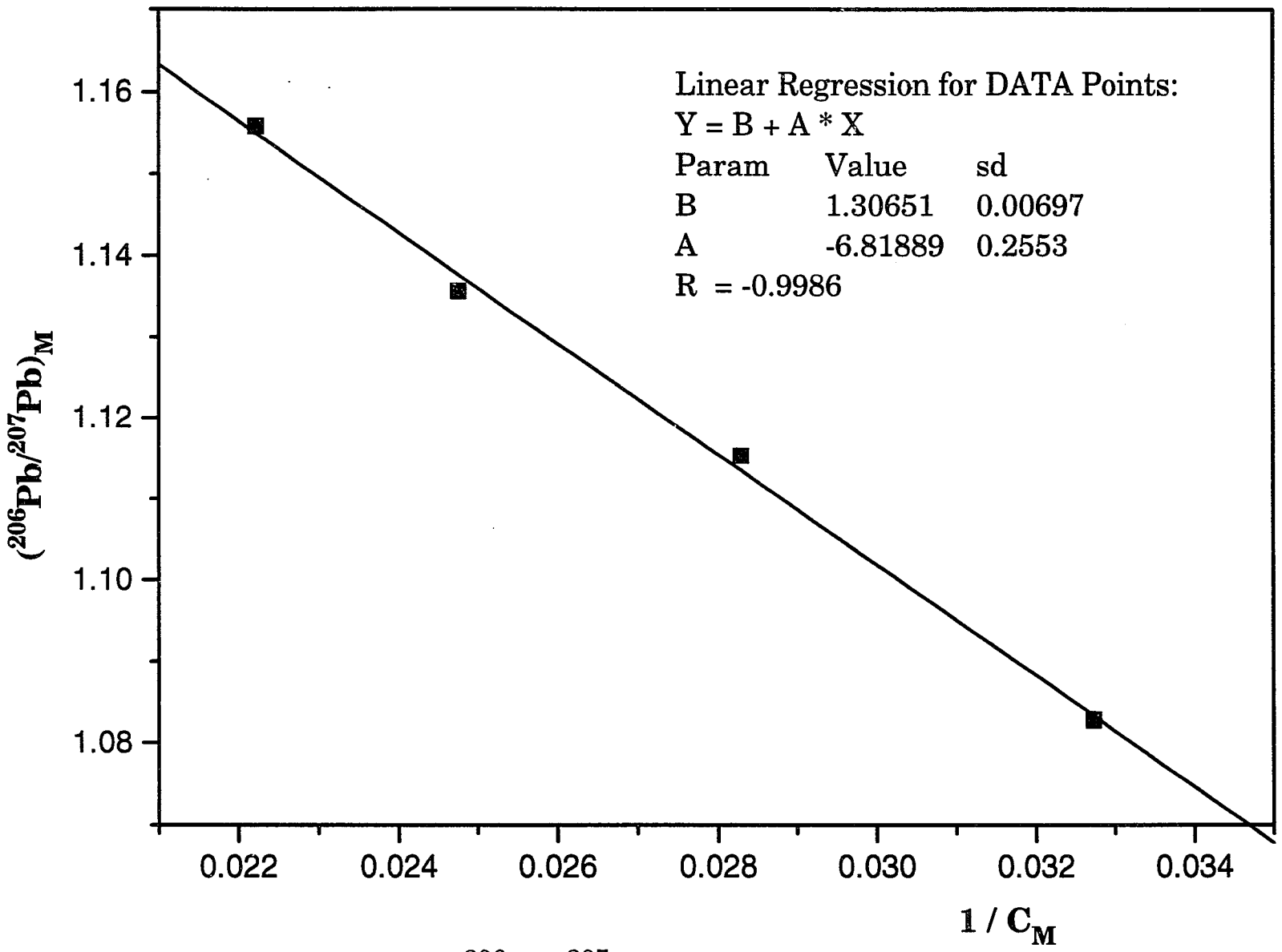

Figure 7.7 Plot of $(^{206}Pb/^{207}Pb)_M$ versus $1/C_M$.

concentrations of SPEX and SPEX2 before they were mixed. The relative errors by this method are -2.0% and -2.6%, respectively.

An alternative way to evaluate C_{Pb1} and C_{Pb2} is to use Equations 7.2 and 7.1. Both sides of Equation 7.1 are divided by C_M. Equation 7.1 becomes:

$$1 = \frac{C_{Pb1} \times f}{C_M} + \frac{C_{Pb2}}{C_M} \times (1 - f) \tag{7.8}$$

Let $\frac{C_{Pb1}}{C_M} = X$, and $\frac{C_{Pb2}}{C_M} \times (1 - f) = 1 - X$. Substituting X and 1- X into Equation 7.2, and eliminating C_M, Equation 7.2 reduces to:

$$(\frac{^{206}Pb}{^{207}Pb})_M = \frac{X \times Ab_1^{206} \times W_1 + (1 - X) \times Ab_2^{206} \times W_2}{X \times Ab_1^{207} \times W_1 + (1 - X) \times Ab_2^{207} \times W_2} \tag{7.9}$$

Now we can substitute experimental data in Table 7.5 to get X and C_{Pb}. Let Ab_1^{206} and Ab_1^{207} be abundance of ^{206}Pb and ^{207}Pb in SPEX solution, and Ab_2^{206} and Ab_2^{207} be abundance of ^{206}Pb and ^{207}Pb of SPEX2 solution. W_1 and W_2 are atomic weights of Pb calculated from SPEX and SPEX2 abundance. The last set of data (C_M = 30.55 ppb, $^{206}Pb/^{207}Pb$ = 1.083) gives:

$$C_{Pb1} \times f = 8.66 \tag{7.10}$$

$$C_{Pb2} \times (1 - f) = 21.89 \tag{7.11}$$

Repeating the calculation using C_M= 40.38 ppb, ^{206}Pb / ^{207}Pb = 1.136, we have:

$$C_{Pb1} \times f' = 29.94 \quad (7.12)$$

$$C_{Pb2} \times (1- f') = 10.44 \quad (7.13)$$

combining Equations 7.10 - 7.13, and solving the resulting equations, finally we obtain C_{Pb1} = 49.34 ppb, and C_{Pb2} = 26.55 ppb. With other sets of data shown in Table 7.5, we can find different sets of C_{Pb1}'s and C_{Pb2}'s. The average values of C_{Pb1} and C_{Pb2} are 49.44 ppb and 26.54 ppb, respectively. The relative errors by this method are 0.4% and 2%.

We have shown that we can calculate concentrations of Pb from two-component mixtures having different ^{206}Pb / ^{207}Pb ratios using Equations 7.2 and 7.5. The method based on Equation 7.5 is simple and fast, but there is a restriction when using this method. If the difference in abundance of ^{207}Pb in two components is too much, this method can not work. The method in terms of Equation 7.2 can provide accurate results but takes a lot of time to calculate the abundance and the atomic weights and solve many equations.

It is impossible to find C_{Pb}'s from more than two component mixtures using Equations 7.2 or 7.5 because the number of unknowns is more than the number of equations. In practical cases, lead in drinking water may come from more than two sources. If the concentration of Pb contributed from some source is very small relative to other sources this portion of Pb can be neglected and the problem can be treated as a two-component mixture.

7.5 Results and discussion

Table 7.6 lists the concentration of Pb and some other elements in the water samples, which were collected on July 11, 1992. For the convenience of studying the sources of Pb, pH values and temperatures of the samples are

also listed in the table. Generally, the concentrations of all analyzed elements in water samples decreased along the pipes from the house to the street main, as shown in Figure 7.8, 7.9a, 7.9b, and 7.13, in which the concentrations of some elements are plotted versus the sample number. The concentrations of Zn and Cu (Figure 7.13) in the first four samples are much higher than those in subsequent collected samples, indicating that Zn and Cu were leached from the faucet, and brass pipes C and B. The change of concentrations of Mn, Se, Sr, and Ba shows the normal trends. The concentrations of Cr and Ni (Figure 7.9b) decreased smoothly but peaked at the 8th sample (cumulative volume = 2410 ml). Nickel and Chromium in the 8th sample were mainly from the steel pipe (see Figure 7.1). The concentrations of Ca and Mg correlated well. They both show peaks at the sample number of 15 and 16. The #15 and #16 samples were located in the Pb pipe (see Figure 7.10). The Pb pipe adsorbed Mg^{2+} and Ca^{2+} (probably other elements such as Fe and Al) and increased their concentrations in the water samples located in the Pb pipe since water remained in the pipe overnight. The concentrations of Al (sample #23) and Fe (sample #27) in the samples from the street main are anomalously high. The reasons for that are not understood. One possible reason is that this portion of Fe and Al was from the street main (cast iron) and the connection between the Pb pipe and the street main, respectively.

The concentrations of Zn, Cr, As, Ba, and Fe (except one sample, #27) measured in the drinking water met the Federal standards as shown in Table 7.7. The concentration of Cu in the first four samples is high due to leaching of copper from the faucet, brass pipe C and B. However, 62.5% (20 out of 32) of water samples collected failed to meet the new Federal standard

Table 7.6 Measured pH and temperature (°C) of water samples, and concentrations (ppb) of some elements in water samples.

sample #	Mg	Al	Ca	V	Cr	Fe	Mn	Ni	Co	Cu
1	**1.866 E4**	228.5	**7281**	**1.0**	**11.7**	209.4	39.7	**20.5**	**0.3**	**3483**
2	4654	2410	5151	0.4	7.6	155.5	12.4	6.7	0.1	1648
3	5232	582.5	5836	0.4	3.7	180.5	21.8	4.8	0.1	1735
4	5051	493.8	5718	0.4	3.7	207.4	37.9	5.4	0.1	1173
5	4270	37.5	4966	0.4	2.5	197.5	36.9	4.3	BDL	489.4
6	4482	39.3	5146	0.4	2.7	194.9	38.6	4.7	0.1	550.2
7	3902	90.2	4545	0.3	2.3	180.0	35.4	3.9	0.1	404.6
8	4041	29.1	4664	0.5	7.8	200.7	36.1	8.5	0.1	376.2
9	3535	25.6	4050	0.3	2.8	149.3	29.7	3.3	0.1	297.3
10	3869	41.5	4419	0.4	3.8	162.0	34.2	3.8	0.1	315.2
11	3494	30.0	3860	0.4	2.3	120.1	29.5	3.0	0.1	237.7
12	4181	**2966**	4773	0.6	2.5	173.0	39.2	4.7	0.1	314.8
13	4221	2959	4764	0.4	2.1	152.0	35.0	3.6	0.1	279.0
14	3813	1268	4358	0.3	2.4	174.4	32.9	3.6	0.1	261.8
15	5041	195.7	5574	0.4	2.1	177.2	**41.8**	3.8	0.1	332.0
16	5400	139.5	5740	0.4	2.1	175.5	40.3	3.2	0.1	345.5
17	2809	81.7	3234	0.2	1.3	101.9	24.8	2.0	BDL	224.7
18	2616	54.6	2949	0.2	1.2	89.9	24.2	2.0	BDL	215.6
19	2275	42.5	2559	0.2	1.1	88.1	23.1	1.7	BDL	173.4
20	2296	24.2	2708	0.2	1.5	92.9	23.5	1.6	BDL	169.3
21	2588	42.8	2737	0.2	1.1	93.1	27.9	2.1	BDL	163.1
22	2639	38.9	2742	0.2	1.2	81.5	25.1	1.4	BDL	125.1
23	2605	2467	2718	0.3	1.4	88.7	24.7	1.5	0.1	124.2
24	3566	1040	3616	0.3	1.3	110.3	30.0	2.0	BDL	141.6
25	2264	316.3	2448	0.2	0.9	84.0	23.5	1.1	BDL	87.6
26	2544	173.2	2735	0.2	1.0	92.2	25.7	1.5	BDL	94.6
27	2922	67.1	3297	0.3	1.6	**324.0**	28.8	5.2	BDL	98.2
28	2520	58.8	2822	0.2	1.2	100.1	27.6	1.9	BDL	78.4
29	2616	48.3	2893	0.2	1.3	100.1	29.3	2.0	BDL	80.9
30	2946	22.9	3227	0.3	1.1	99.7	29.8	1.9	BDL	75.8
31	2652	34.9	3092	0.3	1.4	93.0	36.4	1.7	BDL	129.9
32	2574	24.4	2928	0.3	1.3	85.0	20.5	1.2	BDL	51.2
NIST1643c	8658	179.2	7840	27.3	19.6	103.2	31.6	52.6	20.6	19.2
NIST1643c (certified)	9450	114.6	3.68E4	31.4	19.0	106.9	35.1	60.6	23.5	22.3

BDL ——— below detection limit.

bold values represent the maximum concentrations in water samples.

Table 7.6 (continued)

sample #	Zn	As	Se	Rb	Sr	Ba	Pb	pH	H^+ ion	Temp.	cumulative. vol.(ml)
1	**3587**	0.8	**51.4**	**2.0**	**73.2**	**94.9**	**213.3**	6.65	2.24E-07	23.2	20
2	2004	0.6	32.2	1.2	52.0	41.3	10.9	6.72	1.91E-07	23.0	540
3	1659	0.6	41.4	1.2	55.4	38.8	12.4	6.94	1.15E-07	23.4	810
4	973.5	1.1	36.7	1.5	57.8	39.5	41.0	7.03	9.33E-08	23.4	1080
5	347.5	0.8	33.0	1.1	47.2	35.4	63.6	7.09	8.13E-08	23.3	1600
6	395.0	1.0	30.0	1.0	47.3	34.9	70.2	7.12	7.59E-08	23.0	1870
7	327.4	0.6	28.0	0.9	44.0	32.7	68.8	7.14	7.24E-08	23.1	2140
8	312.7	0.6	29.8	1.1	43.5	32.0	82.6	7.16	6.92E-08	23.1	2410
9	215.5	0.5	31.4	0.8	38.9	29.0	78.8	7.17	6.76E-08	23.0	2680
10	216.4	0.9	27.6	0.9	44.4	32.9	81.2	7.19	6.46E-08	23.0	3200
11	162.1	0.4	26.3	0.9	37.6	27.9	79.8	7.19	6.46E-08	22.9	3470
12	290.6	0.6	27.9	1.0	46.4	34.2	79.4	7.18	6.61E-08	22.8	3740
13	203.9	0.9	31.4	0.9	45.2	31.6	72.4	7.18	6.61E-08	22.8	4010
14	200.7	0.6	25.7	0.9	40.4	29.4	70.7	7.18	6.61E-08	22.9	4280
15	245.7	0.9	36.9	1.2	50.2	35.9	69.8	7.18	6.61E-08	22.8	4550
16	266.9	**1.3**	35.1	1.2	49.9	33.4	65.3	7.18	6.61E-08	22.8	5070
17	181.7	0.7	20.2	0.7	34.1	28.4	61.2	7.18	6.61E-08	22.6	5590
18	164.8	0.6	18.1	0.8	31.7	25.8	51.1	7.17	6.76E-08	22.5	6110
19	116.8	0.6	16.8	0.7	29.1	26.3	46.1	7.18	6.61E-08	22.4	6630
20	103.8	0.6	16.4	0.7	30.4	25.9	43.7	7.18	6.61E-08	22.2	7150
21	109.6	0.8	18.5	0.7	29.9	26.0	24.0	7.18	6.61E-08	21.8	7670
22	104.9	0.7	18.4	0.6	29.5	24.4	11.7	7.18	6.61E-08	21.1	8190
23	92.8	0.6	18.2	0.7	29.1	24.0	10.3	7.18	6.61E-08	20.4	8710
24	103.8	0.6	21.4	0.8	36.0	28.8	9.7	7.19	6.46E-08	20.0	9230
25	58.5	0.7	15.4	0.7	29.3	24.2	9.7	7.19	6.46E-08	19.7	9750
26	73.4	0.5	18.3	0.7	30.5	26.5	10.9	7.19	6.46E-08	19.5	10270
27	64.1	0.7	20.1	0.8	34.2	28.6	13.5	7.18	6.61E-08	19.6	10790
28	54.4	0.6	18.5	0.8	33.1	26.4	12.1	7.18	6.61E-08	19.2	11810
29	61.9	0.7	19.1	0.7	34.3	27.7	10.8	7.13	7.41E-08	19.0	12830
30	53.2	0.5	20.8	0.7	32.6	25.0	10.1	7.07	8.51E-08	18.9	13850
31	57.4	0.7	19.0	0.7	30.4	25.3	22.8				14870
32	27.1	0.5	17.2	0.7	29.6	24.6	11.3				16870
nist1643c	75.8	75.0	21.8	10.0	231.6	46.2	34.2				
nist1643c (certified)	73.9	82.1	12.7	11.4	263.6	49.6	35.3				

bold values represent the maximum concentrations in water samples.

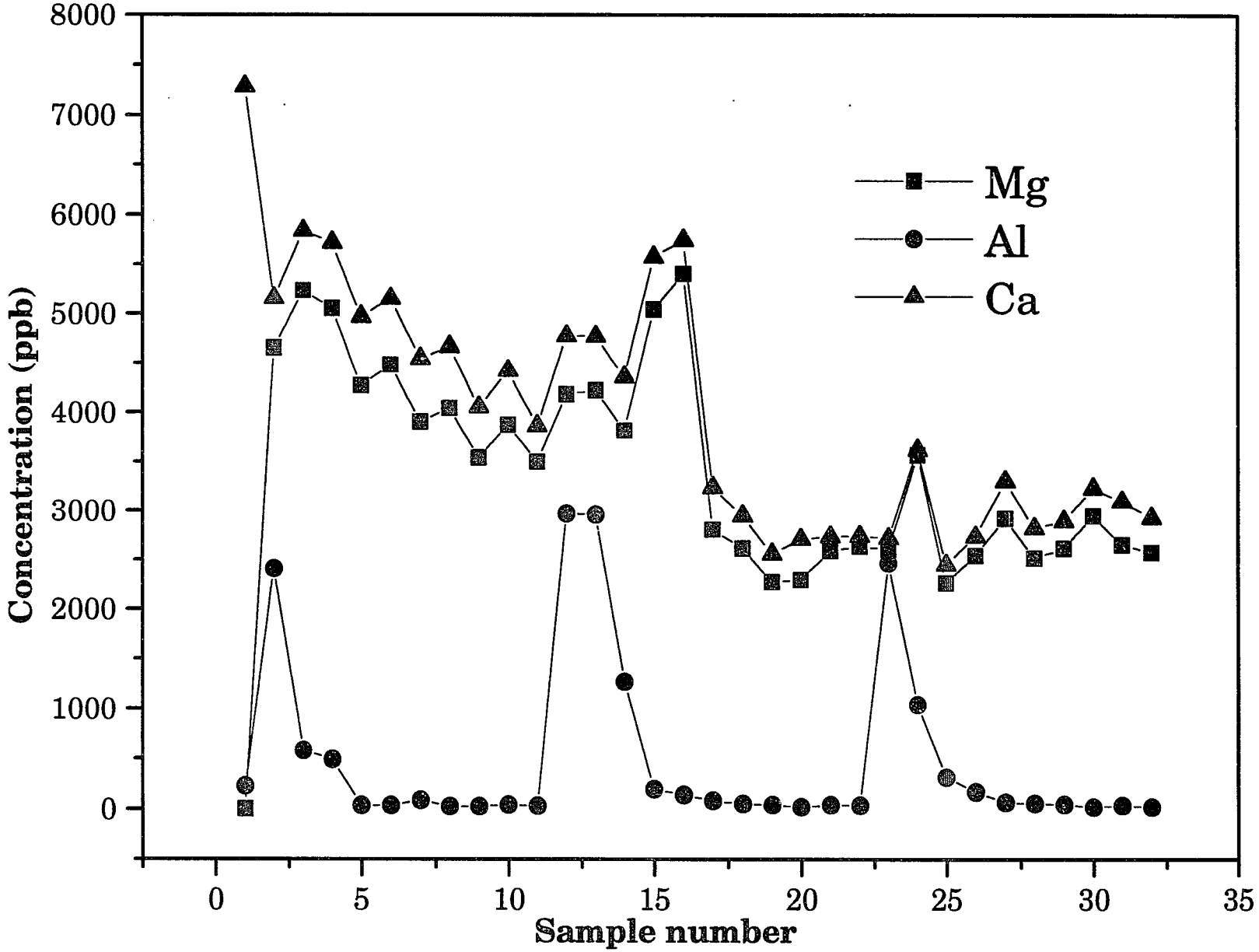

Figure 7.8 Plot of concentration of Ca, Mg, and Al versus sample number.

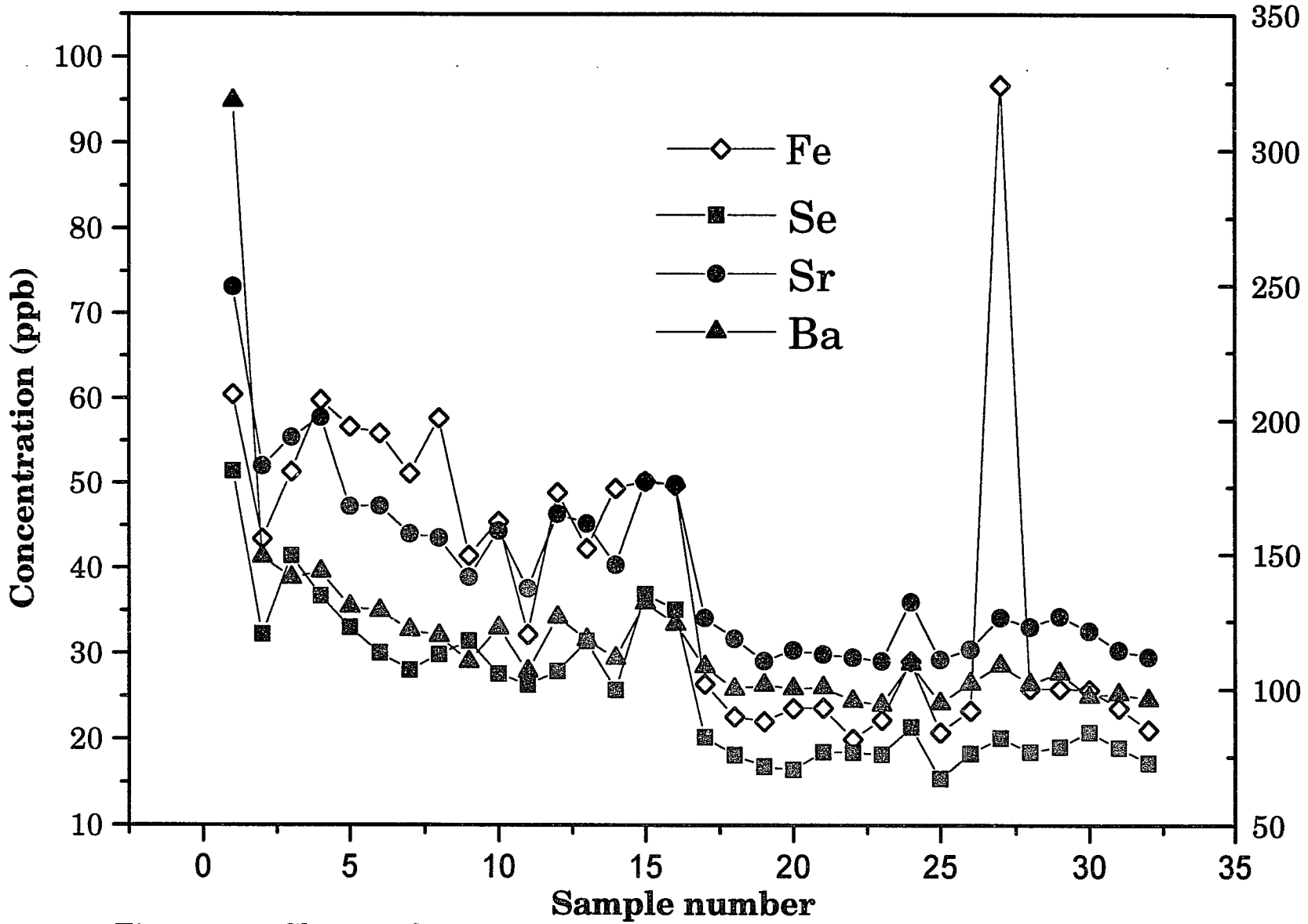

Figure 7.9a Change of concentration of some elements along the pipes.
The scale on the right is for Fe.

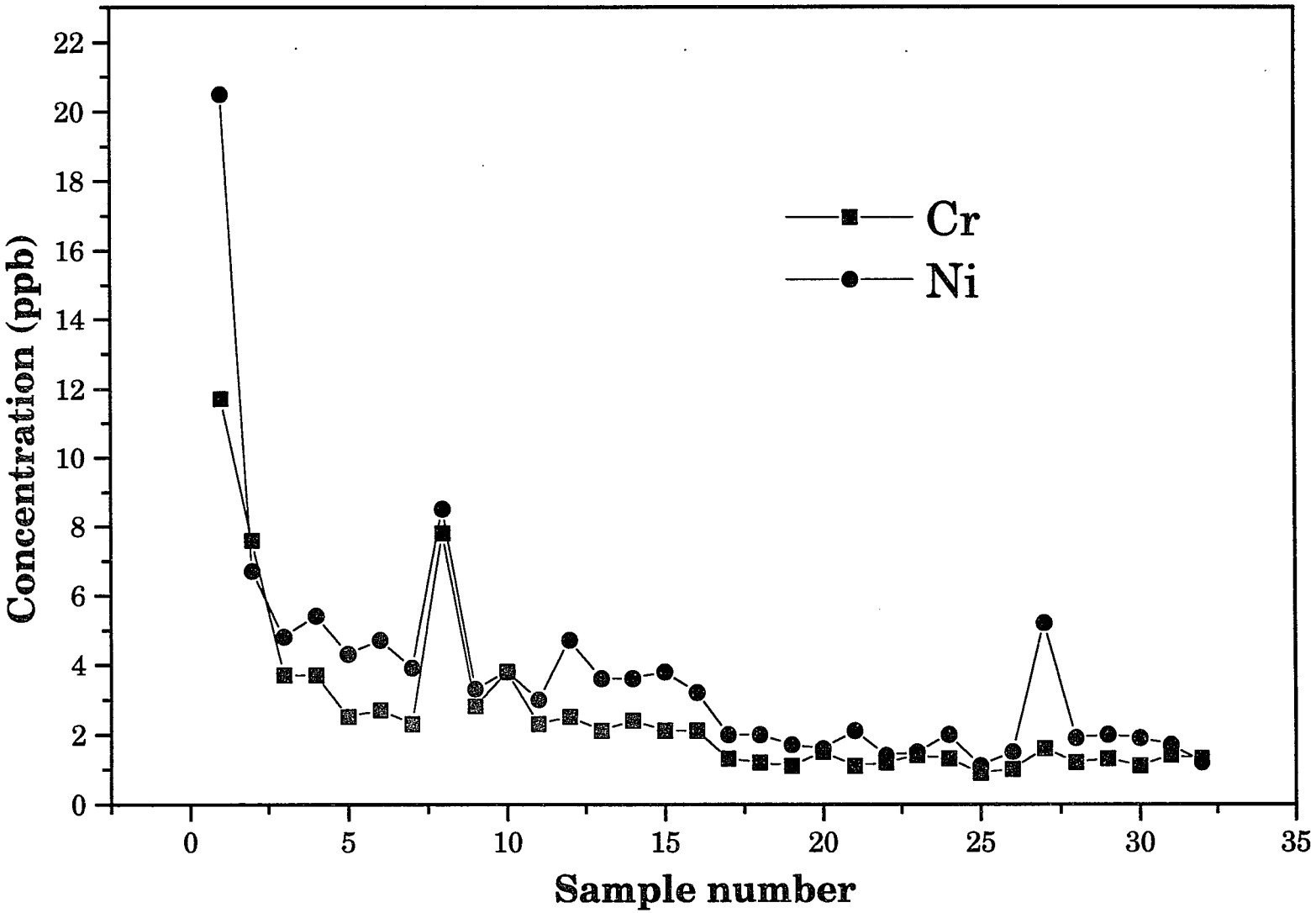

Figure 7.9b Change of concentration of Ni and Cr along the pipes.

of lead (15 ng/ml). To find the sources of Pb, the location of each of sample in the plumbing system should be known.

Table 7.7 Maximum contaminant level (MCL, ng / ml) of some elements in drinking water required by USEPA.

element	As	Ba	Cr	Pb	Cu	Fe	Zn
MCL	50	1000	50	15	1000	300	5000

From the inner diameters of the pipes measured and the cumulative volumes when each sample was collected, the corresponding locations of the samples are known. Sample #1 was collected from brass pipe C (the smallest pipe, see Figure 7.1), samples #2 to #4 were from brass pipe B, samples #5 to #9 were from brass pipe A, and sample #10 and the subsequent samples were from the Pb pipe and street water main. The length of Pb pipe between the foundation and main can be estimated from Figure 7.10, in which lead concentration and water temperature versus sample number are plotted. The water temperatures decreased from the first sample to the last sample because water temperature in street water main is lower. But the degrees of decrease in temperature are different along the pipes and main. Figure 7.10 shows that the slope of the temperature curve from the first point to 21st point is smaller than that from 21st point to 30th point. Also, the concentration of Pb decreases from 21st sample to 22nd sample and then becomes steady. Probably sample #21 or #22 and subsequent samples were located in street main before they were being sampled. The cumulative volume drawn from the tap at this point was about 8190 ml.

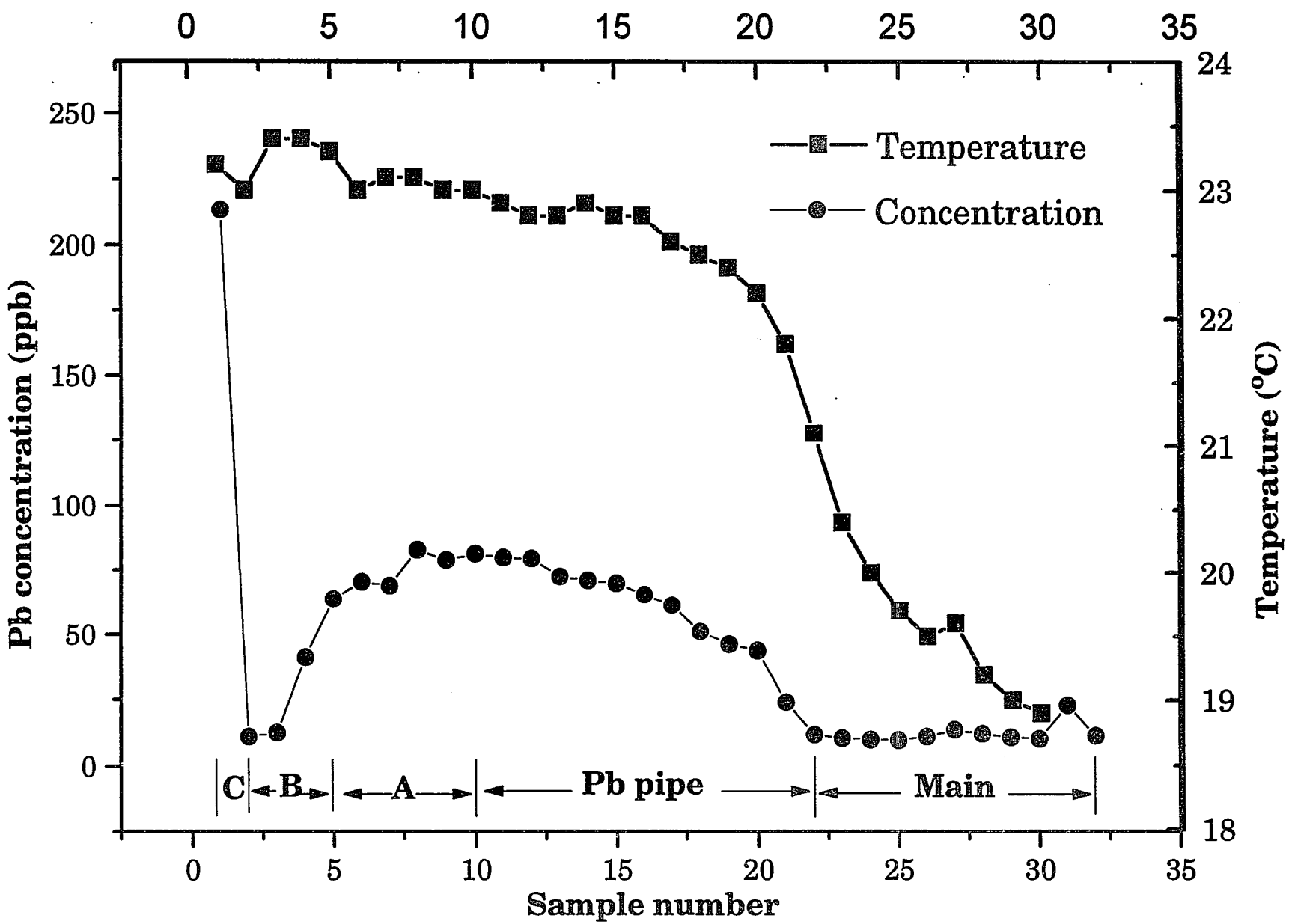

Figure 7.10 Change of temperature and Pb concentration in drinking water along the pipes.

Figure 7.10 also indicates that the concentration of Pb increases from pipe B to pipe A, then reaches a maximum in the lead pipe and returns to a minimum value, about 10 ng/L, in the street main. Did this "background" Pb come from the street main or from the pipes in the house? The answer can be found in Table 7.8, in which the concentration and $^{206}Pb/^{207}Pb$ ratio of Pb in the water samples from fire hydrants are shown.

Table 7.8 shows that the concentration of Pb in water samples from street mains is very low, less than 2.5 ppb. The $^{206}Pb/^{207}Pb$ ratio of Pb in water samples from Manhattan is remarkably higher than those from Brooklyn and Queens because the drinking water supplied to Manhattan and Long Island (Queens and Brooklyn) has different sources. There are three water-supply systems for New York City: 1) the Croton system built in 1842 in Hillview, NY; 2) the Catskill system built in 1907 in Kensico, NY; and 3) the Delaware system built in 1965 in Kensico, NY. The Croton system supplies water to Manhattan and the Bronx. The Catskill and Delaware systems mainly provides water to Queens, Brooklyn, and Staten Island. The average value of $^{206}Pb/^{207}Pb$ ratio in the samples from Brooklyn and Queens is 1.163. This value is significantly different from $^{206}Pb/^{207}Pb$ ratios in the water samples collected from ETW's house, as shown in Table 7.9. It is obvious that the "background" Pb did not come from the street main. This result is consistent with the conclusion, made by Albert F. Appleton, the New York City Environmental Protection Commissioner, the city's water does not contain unacceptable concentration of lead before it enters buildings from mains [92].

Since most of the lead in drinking water drawn in this experiment does not originate from the street water main, it must come from the plumbing system in the house. The sources of lead in the plumbing system can be

Table 7.8 Concentration and isotope ratio of Pb in the water samples collected from fire hydrants in New York City.

hydrant location	Pb conc. (ppb)	^{206}Pb / ^{207}Pb (RSD%)
233 Clinton St. (B)	2.46	1.168 (1.5%)
326 Clinton St. (B)	0.08	1.139 (13%)
43-37 156 St. (Q)	0.25	1.160 (9.6%)
143-15 Rose Ave. (Q)	0.26	1.183 (2.6%)
230 Clinton St., #1 (M)	0.20	1.474 (12%)
230 Clinton St., #2 (M)	0.19	1.562 (17%)

B, Q, and M represent Brooklyn, Queens, and Manhattan, respectively.

Table 7.9 Isotope ratio of $^{206}Pb/^{207}Pb$ in drinking water from Brooklyn.

sample #	$^{206}Pb/^{207}Pb$	sample #	$^{206}Pb/^{207}Pb$
1	1.227±0.005	17	1.275±0.008
2	1.262±0.029	18	1.271±0.009
3	1.273±0.021	19	1.266±0.006
4	1.279±0.013	20	1.273±0.010
5	1.282±0.006	21	1.254±0.023
6	1.273±0.006	22	1.277±0.030
7	1.279±0.007	23	1.253±0.012
8	1.283±0.014	24	1.283±0.008
9	1.276±0.002	25	1.254±0.031
10	1.280±0.006	26	1.254±0.010
11	1.275±0.010	27	1.275±0.023
12	1.280±0.006	28	1.268±0.012
13	1.274±0.015	29	1.255±0.025
14	1.274±0.008	30	1.265±0.052
15	1.278±0.016	31	1.260±0.027
16	1.272±0.005	32	1.276±0.019

deduced from Table 7.10. The concentrations of Pb and ^{206}Pb /^{207}Pb ratios in the brass pipes, the Pb pipe, and the tap fixture are listed in the table. The ^{206}Pb /^{207}Pb ratios in water samples from #2 to #32 (see Table 7.9 and Figure 11) are very close to the $^{206}Pb/^{207}Pb$ ratio (1.283) in the lead pipe. The result of a t-test (95% confidence level) showed that there were no significant differences between the means of the ratios in water samples and in the Pb pipe, but there were significant differences between the ratios in water and in the brass pipes. The result implies that majority of lead comes from the lead pipe. This conclusion can be further proven by the correlation diagram shown in Table 7.11. The population correlation calculation returns the covariance of two data sets divided by the product of their standard deviations. All the original data sets of Table 7.11 come from Table 7.6. One can find from Table 7.11 that most of the correlation coefficients between the concentration of hydrogen ion and other elements have values greater than 0.6 except those from monoisotopic elements (As, Mn, Al) and Fe which suffered interferences from other elements when they were measured by the instrument. The concentration of hydrogen ion also has a poor correlation with that of lead (0.42). The changes of lead and hydrogen ion concentrations in water samples are shown in Figure 7.12. The concentrations of lead and hydrogen ion in the main correlate well. But in brass pipes (from samples #9 to #2), the concentration of lead decreases while the concentration of hydrogen ion increases. In the lead pipe (samples #21 to #10), lead concentrations are high even though $[H^+]$ is low. The similar change in concentrations of Pb, Cu, and Zn in water along the pipes can be found in Figure 7.13. The correlation coefficient between Cu and Zn is 0.99. The correlation coefficients between Pb and Zn, Pb and Cu are 0.54 and 0.57, respectively. The major compositions of brass pipe are Cu and Zn. In the

Table 7.10 Concentration (ppm, unless otherwise noted) of lead and $^{206}Pb/^{207}Pb$ ratio in the metal of the pipes.

sample	brass pipe A	brass pipe B	brass pipe C	Pb pipe	brass faucet
$^{206}Pb/^{207}Pb$	1.188±0.008	1.198±0.001	1.196±0.006	1.283±0.001	1.196± 0.001
concentration	89.5±1.3	126.5±1.4	77.1±0.7	pure Pb	6.55%±0.01%

Table 7.11 Correlation among concentrations of some elements.

Mg	Mg																		
Al	0.02	Al																	
Ca	0.74	0.17	Ca																
V	0.89	0.24	0.80	V															
Cr	0.81	0.11	0.71	0.85	Cr														
Fe	0.41	0.02	0.66	0.53	0.46	Fe													
Mn	0.41	-0.07	0.58	0.52	0.19	0.51	Mn												
Ni	0.94	0.04	0.73	0.92	0.92	0.56	0.37	Ni											
Cu	0.89	0.09	0.74	0.79	0.85	0.38	0.10	0.88	Cu										
Zn	0.87	0.13	0.70	0.77	0.86	0.34	0.03	0.87	0.99	Zn									
As	0.33	-0.04	0.53	0.26	0.12	0.38	0.60	0.22	0.21	0.16	As								
Se	0.78	0.11	0.98	0.81	0.73	0.61	0.53	0.76	0.79	0.75	0.45	Se							
Rb	0.87	0.06	0.92	0.84	0.80	0.61	0.50	0.86	0.87	0.83	0.49	0.92	Rb						
Sr	0.81	0.16	0.98	0.84	0.77	0.63	0.52	0.80	0.83	0.80	0.50	0.97	0.96	Sr					
Ba	0.99	0.04	0.75	0.89	0.84	0.43	0.35	0.95	0.93	0.92	0.31	0.79	0.89	0.83	Ba				
Pb	0.79	-0.05	0.65	0.80	0.66	0.38	0.60	0.77	0.57	0.53	0.27	0.66	0.67	0.65	0.76	Pb			
pH	-0.75	-0.15	-0.61	-0.66	-0.80	-0.28	0.11	-0.77	-0.93	-0.95	-0.06	-0.65	-0.73	-0.71	-0.81	-0.36	pH		
H^+	0.79	0.16	0.59	0.70	0.83	0.26	-0.10	0.81	0.93	0.96	0.06	0.63	0.73	0.69	0.84	0.42	-0.99	H^+	
Temp.	0.36	0.11	0.67	0.47	0.47	0.37	0.33	0.40	0.43	0.39	0.29	0.65	0.56	0.62	0.39	0.62	-0.27	0.26	Temp.

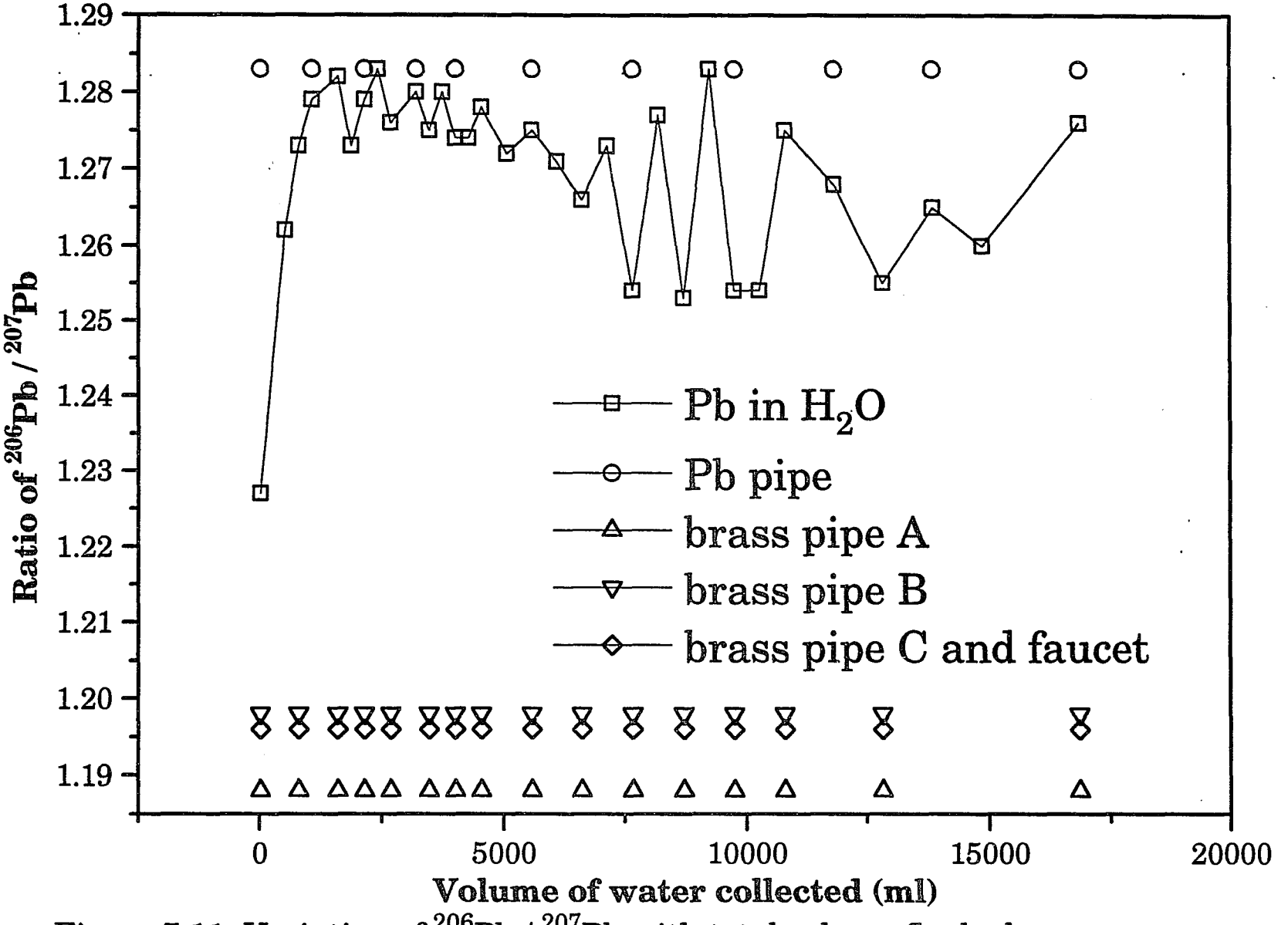

Figure 7.11 Variation of ^{206}Pb / ^{207}Pb with total volume flushed.

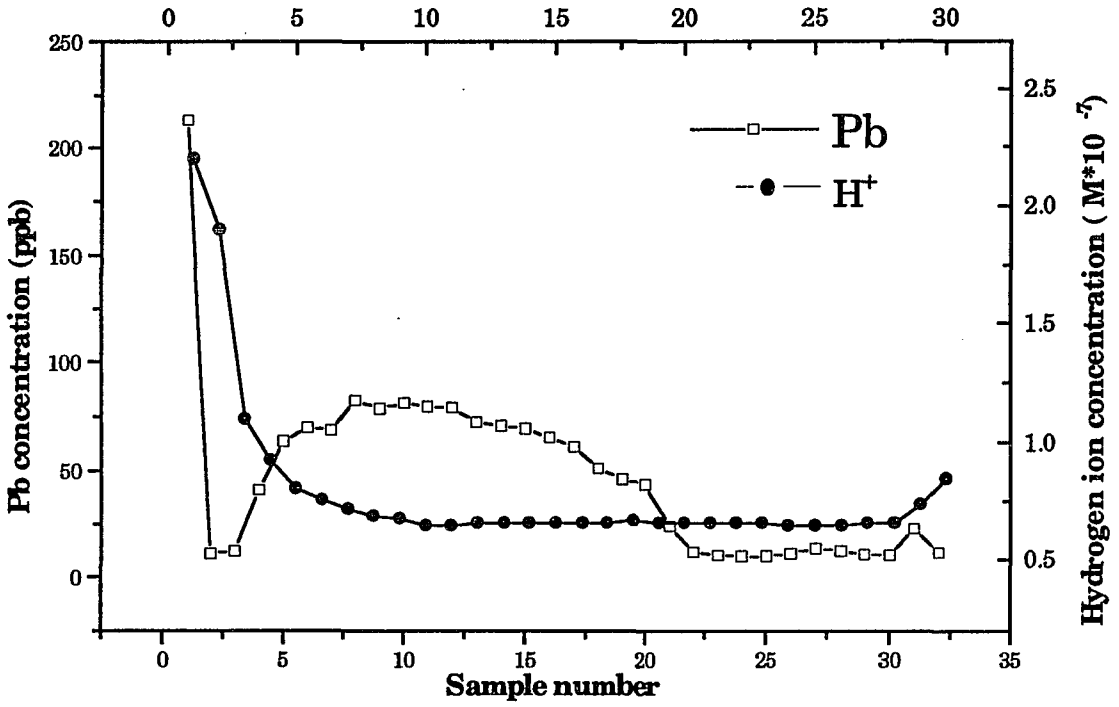

Figure 7.12 Change of concentrations of H^+ and Pb in water along the pipes.

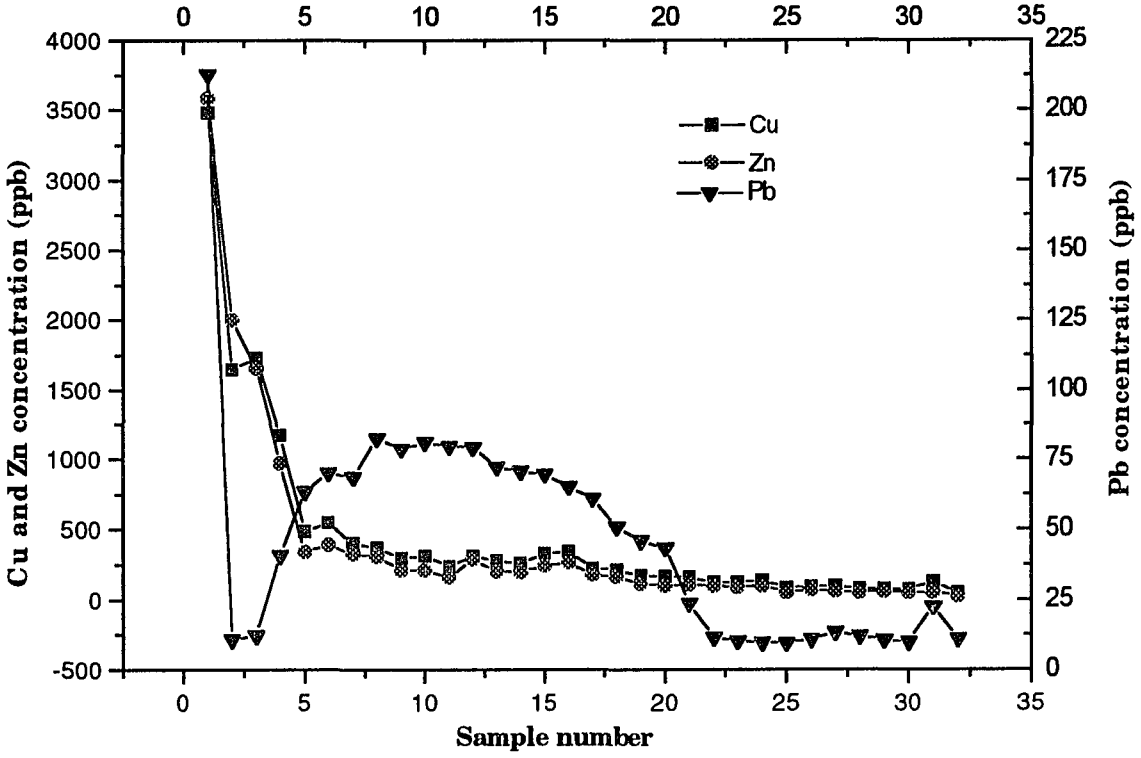

Figure 7.13 Concentrations of Pb, Cu, and Zn in water samples.

brass pipes, the concentration of Cu and Zn were leached from the pipes, so Cu and Zn concentrations in the brass pipes were higher than those in Pb pipe. However, in the brass pipes, the lead concentration did not increase consistently indicating that lead was not extracted from the brass pipes.

The concentration of Pb in the first water sample is substantially higher (see Figure 7.13). This portion of water was located in the faucet. The concentration of Pb in brass pipe C is 77 μg/g while the concentration of Pb in the water located in the pipe is 213 ng/g. On the other hand, the concentration of Pb in brass pipe B is 126 μg/g while the concentration of Pb in the water in pipe B (samples #2 to #4) is 21 ng/g (three sample average). If lead in water located in the brass pipes came from the Pb pipe through diffusion, the concentration of Pb in brass pipe C should be lower than that in brass pipe B since pipe B is closer to the Pb pipe than pipe C. Therefore, the high Pb concentration in the first water sample means that there is another source that provides Pb except the Pb pipe. The only suspected source is the faucet connected to brass pipe C. The concentration of Pb and the ratio of $^{206}Pb/^{207}Pb$ in the faucet are 6.55% and 1.196, respectively. The ratio of $^{206}Pb/^{207}Pb$ in the first sample is 1.227 which is in between the corresponding ratios in the faucet and the Pb pipe (1.283). Unfortunately, we only collected one water sample from brass pipe C so that we can not calculate original concentration of Pb leached from the faucet and the Pb pipe. But we know that most of the lead in the first water sample was leached from the faucet because the ratio of ^{206}Pb /^{207}Pb in the sample is closer to that in the faucet and the Pb content of the faucet is extremely high compared to that in the brass pipes.

Lead in drinking water located in brass pipes A and B might have come from the Pb pipe through diffusion. However, the water-flowing distance

from pipe B to the Pb pipe varies from 11.6 feet (354 cm) to 19.6 feet (598 cm), and the distance of the farthest end of pipe A to the Pb pipe is 11.6 feet. The basement tap was not open for at least one week before the water samples were collected. Can lead leached from the Pb pipe migrate to brass pipes A and B through such a long distance in stagnant water? Figure 7.14 shows the diffusion profile of Pb in a PVC pipe (see Chapter 7.2, sample preparation). Furthermore, the average ratio of ^{206}Pb /^{207}Pb in water samples (#7 to #13) collected from PVC pipe is 1.100 ± 0.011, which is close to the certified value (1.0933) of NIST 981 lead solution that was spiked in the PVC pipe. That is to say, lead did diffuse along the PVC pipe under stagnant conditions. From Figure 7.14, the concentration of lead in PVC pipe at the distance (from the Pb spiked end) greater than 155 cm is very low, less than 1 ppb. The diffusion test showed that Pb leached from lead pipe cannot migrate to brass pipes B and C under stagnant conditions. But when we opened the tap to collect water samples, the water state in the pipes changed from stagnant to flowing. Potential and pressure differences "pushed" lead from the Pb pipe into the brass pipes. The measured concentration of lead in water samples from #2 to #9 is the sum of the "background" Pb concentration (about 10 ppb) and the concentration of Pb diffused from the Pb pipe under flowing condition.

Up to now it is clear that Pb in the drinking water drawn in this experiment mainly came from two sources: the Pb pipe and the faucet. The circles in Figure 7.15 represent the sources of Pb. The point in the small circle represents Pb from the faucet. The points surrounded by a big circle indicate the lead leached from the Pb pipe by water staying in the pipe overnight. The "background" Pb, circled by an ellipse, actually came from the Pb pipe. We conclude from the similar isotope ratios that when we were

collecting the samples the running water extracted a small amount of Pb from the Pb pipe while it was rushing through the pipe from the main.

In conclusion, the amount of Pb contributed to drinking water from brass pipes is small. The majority of Pb in the plumbing system is from the Pb pipe and the faucet. Although the absolute amount of Pb leached from the Pb pipe and the faucet is not known, it makes the concentration of Pb in drinking water exceed the Federal standard of 15 ng/ml. These results show that even as water flows quickly through the Pb pipe from the street main in which water is free of lead, it could leach Pb out from the Pb pipe and increase Pb concentration up to 10 ppb. This result is of significance for the many old houses in cities where Pb plumbing is still in use. New York City [92] has decided to add calcium orthophosphate to its drinking water to combat this problem. The calcium orthophosphate forms an insoluble layer on the Pb surface in contact with water and should reduce the leaching of Pb into drinking water.

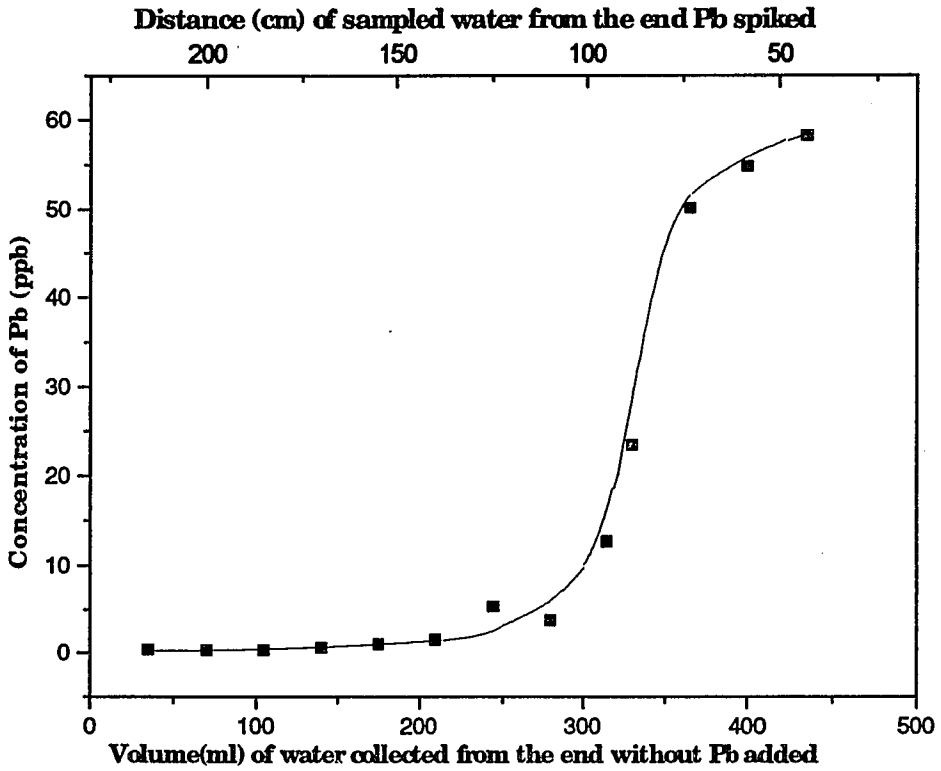

Figure 7.14 Diffusion profile of Pb in a PVC pipe.

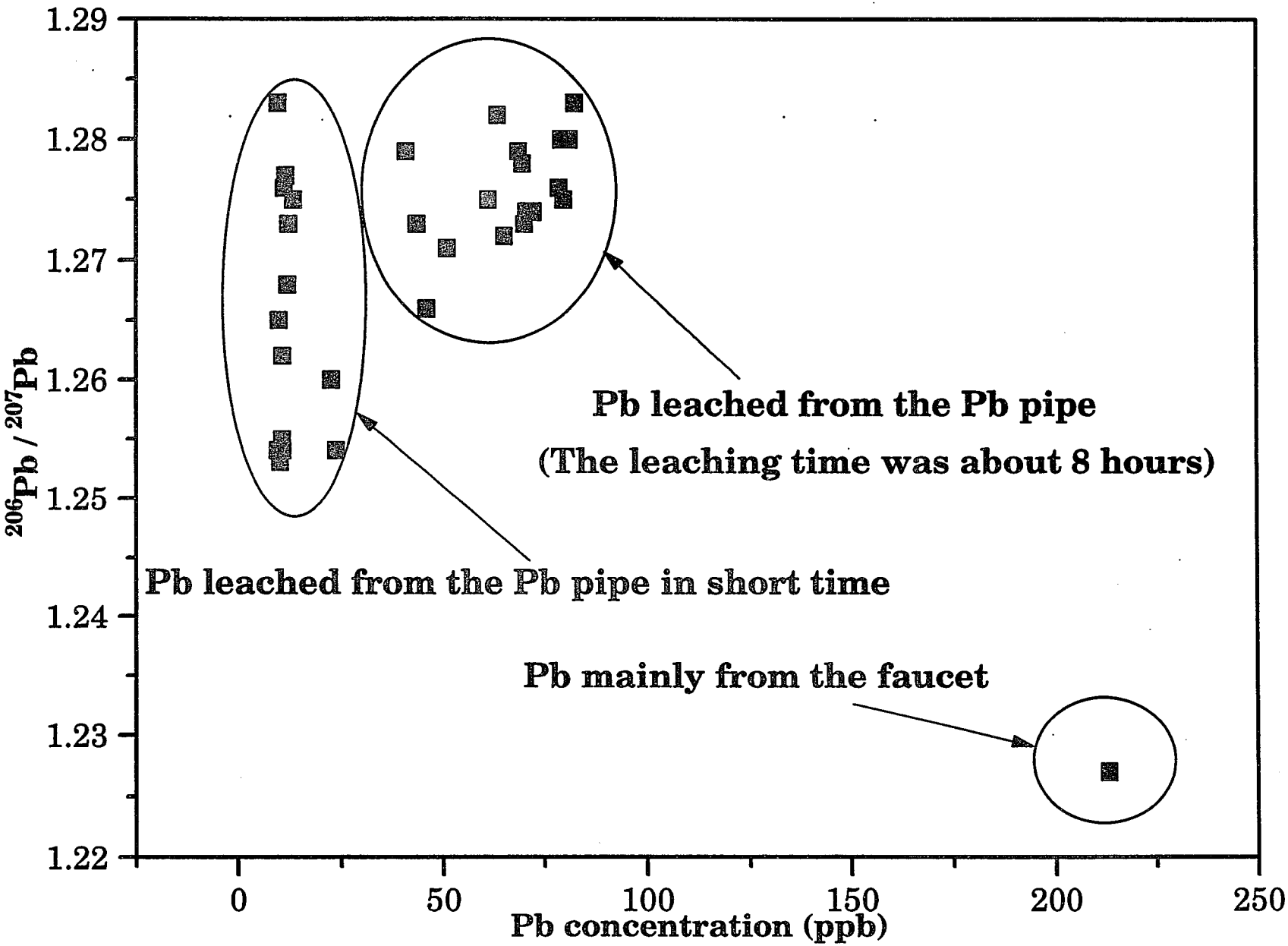

Figure 7.15 Scatter plot of $^{206}Pb/^{207}Pb$ versus Pb concentration.

Chapter 8 Determination of concentration and isotope ratio of lead in tree rings and soil

The antiknock properties of tetraethyl lead was discovered by Thomas Midgley and his colleagues in December 1921 [100]. Since the first gallon of tetraethyl lead (TEL)-added gasoline was sold to a motorist in February 1923 [101], leaded gasoline has become the main force driving the transportation industry. The use of $Pb(C_2H_5)_4$ as gasoline additive increases the engine efficiency, but it has also become one of the few "environmentally unsafe" products. According to Nriagu [100], over seven million tons of lead were burned as lead additives in the United States between 1926 and 1985. The consumption of leaded gasoline was closely matched by airborne level of lead [102] and was consistent with the mean blood lead level of the population in the United States [103].

Lead emitted into the environment, mainly by gasoline combustion and industrial processes, retains the isotopic composition of the ore from which it was derived. Many researchers have utilized the "signature" to distinguish sources of lead pollution in soil [104], airborne [105], snow, and ground water [106] by examining the isotope ratios. These studies demonstrated that isotopic composition of lead is a good indicator to discriminate sources of lead.

So far, there are no published studies on the content of lead in tree rings related to Pb from leaded gasoline by comparing their isotope ratios of Pb using ICP-MS. The objectives of this experiment were to determine the concentration and $^{206}Pb/^{207}Pb$ ratio of lead in tree rings and soil, and observe if the ratio matches the $^{206}Pb/^{207}Pb$ ratio in leaded gasoline. The EPA required major gasoline retailers to sell at least one grade of unleaded gasoline beginning in July 1975 and mandated a reduction in average lead

content from about 0.52 g/l to 0.28 g/l in 1982 and to 0.026 g/l effective in January 1985 [100]. We were interested in whether the concentration of lead in tree rings would decrease accordingly since 1975.

8.1 Sample Collection

The tree cores were collected on September 5, 1991. These trees are located at Ocean Parkway (a street with heavy traffic) and Dekoven Court (a dead end street), Brooklyn, New York. Figure 8.1 is a local map which indicates the sampling site. Sampling consisted of locating candidate trees so situated that comparison could be made of lead concentration in the trees exposed to pollutants emitted from vehicles to different extent. Table 8.1 lists the sites and species of the trees. The trees were sampled using a 40.6-cm-long, 50-mm-diameter, Teflon-plated steel increment borer. The increment borer was inserted at breast height (about 1.3 m) to the center of the tree. The inner wall of the borer was rinsed with acetone after each sampling to minimize cross contamination.

After the cores were extracted from the trees, the holes left were filled with cork to minimize exposure of the tree to insect or fungal invasion. The cores were sealed in plastic straws for later sample preparation and analysis.

The soil samples were taken by boring a small hole with a 92-cm-long, 4-cm-diam. nickel-plated iron increment corer. Core samples at locations A, E, and F were extended to a depth of 36 inches (92 cm) where possible. The cores were divided into 20-cm segments. The soil samples from locations B, C, and D were collected at 10-cm depth. The sampled soils were placed in polyethylene bags.

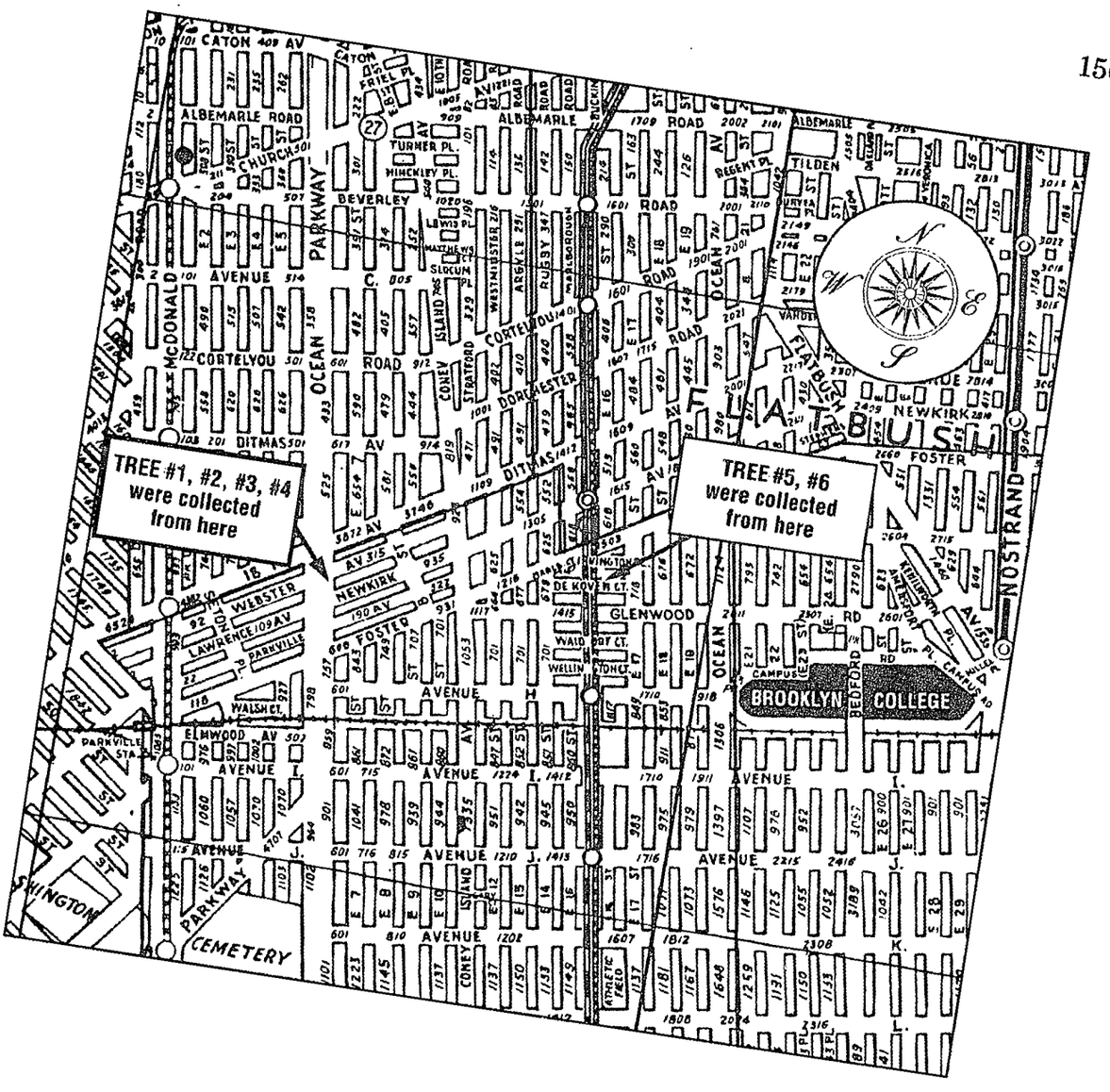

Figure 8.1 Location in Brooklyn, New York from which tree cores and soil were sampled.

Table 8.1 Sites sampled for tree cores in Brooklyn, New York.

Location	Sample ID	Tree species	Number of cores	diameter (inch)
A	#1	Norway maple (*Acer platanoides* L.)	3	22
B	#2	Norway maple	1	16
C	#3	Pin oak (*Quercus phellos* L.)	2	12
D	#4	Linden (*Tilia americana* L.)	2	12
E	#5	London plane (*Platanus* × *acerifolia* Willd.)	2	35
F	#6	Norway maple	2	24

8.2 Sample preparations

8.2.1 Tree sample preparation

In the laboratory the tree cores were placed in a drying oven (Precision Scientific Co., Model 28) at 100 ^{o}C for 3 days. The dried cores were sanded, in sequence, with medium flint paper, finer grit paper (grit No. 2), and silicon carbide paper (No. 600) until the ring structure was clearly revealed. Segments were carefully cut from the cores using a stainless-steel blade. Each cut segment represented two years growth from 1952 to 1991.

The cutting process was somewhat inaccurate for some cores since the distance between successive rings (especially from younger rings) were less than 0.1 mm, and some annual-growth rings were not visible. The structure of the cores from pin oak (tree #3) was handily seen. The ring structure of the cores from linden (tree #4) earlier than 1969 could not be seen clearly. These unclear cores or sections were not further processed.

The segments of the cores were weighed to the nearest 0.01 mg on an analytical balance and then subjected to microwave digestion. If more than one core was sampled from a tree, rings corresponding to the same year were combined and treated as one sample. The procedure and instrument used for dissolution of the wood samples from Brooklyn were the same as that used for Giant Sequoia from California (see Chapter 6). The digestion recipe for wood samples is summarized in Table 8.2. After digestion, the sample solutions were spiked with 1.00 ml of 1.00 ppm thallium solution (ICP Calibration Standards, Environmental Resource Associates) used as an internal standard, and diluted to 20 grams with 18 MΩ ultra-pure water.

A NIST 1575 Pine Needles standard sample was prepared in the same procedure as tree samples except that the standard sample was dried by lyophilization.

8.2.2 Soil sample preparation

Soil samples were placed into 200 ml Pyrex beakers which had been stored in 6N HNO_3 and rinsed with 18 MΩ ultra-pure water. The beakers containing soil were placed in the drying oven at 70 ^oC for 24 hours. The dried samples were sieved through a 437 μm polyethylene screen (Spectrum Medical Industries, Inc.) and ground in a mullite mortar with a mullite pestle to make them homogeneous. The prepared soil samples were used for pH measurement, total and plant-available lead analysis. The soil sample from location C was not processed since the core of tree #3 was not analyzed.

The plant-available Pb is the Pb in soil, which can be taken up by trees. Total Pb includes plant-available Pb and originally bound Pb in soil. The sample preparation procedures for pH measurement and Pb analysis are summarized as follows:

1) pH measurement [107]

A 10-g soil sample was mixed with 30 ml of deionized water in 250 ml polyethylene bottle and shaken for 30 seconds. Sample pH was determined on a digital pH meter after the soil and water were allowed to stand for 60 seconds.

2) Extraction of plant-available lead

An accurately weighed 0.5-g soil sample collected at 4" and 8" depth was placed in a 20-ml polyethylene vial (Wheaton), and 15 ml of 1.0 N HCl (Baker) was added. The sample was shaken in a wrist-action shaker (Burrell

Corp., Model BB) for one hour. The samples were then filtered through Whitman #4 filter paper. A 100-µl aliquot was diluted to a suitable volume and spiked with Tl as an internal standard. According to Neuhauser and Hartenstein [108], this procedure is considered generally capable of extracting plant-available levels of trace metal from soil.

3) Sample dissolution for total lead analysis

A 100-mg sample was accurately weighed to nearest to 0.01 mg into a Teflon digestion cup. To the sample was added 2-ml each of J. T. Baker Ultrex HNO_3 and HF. The samples were subjected to microwave heating using a CEM microwave digestion system. The digestion procedure is summarized in Table 8.2. After digestion, the bomb contents were quantitatively transferred to 20-ml acid-washed polyethylene bottles. The aliquot was then spiked with Tl and diluted to a suitable volume. The final acid content in the sample solution was adjusted to 2% with HNO_3. A certified NIST 278 (obsidian rock) was digested in the same procedure as soil samples. Soil samples treated by this method were not converted to solution completely. Different procedures, including decreasing amount of sample, adding HCl as dissolution agent, and increasing digestion time, had been tried to obtain a clear digested soil solution. However, a very small amount of tiny black particulates were still found on the bottom of the digested solution. To examine if lead was totally converted to solution, a conventional dissolution method was employed.

An accurately weighed 50-mg sample was transferred into a 25 ml Teflon cup (Parr Instrument Company). To the cup was added 5 ml of concentrated HF (J. T. Baker). The cup with sample was placed on hot plate and evaporated to almost dryness. To the cup was then added 5 ml of concentrated HF, 2 ml of concentrated HNO_3, and 2 ml of concentrated

Table 8.2 Recipes for digestion of geological and environmental samples using CEM microwave oven.

Parameter	Value
NIST1575 (pine needles)	
numbers of cup in microwave oven:	6
mass of sample in each cup:	0.20 g
amount of HNO_3 in each cup:	2.0 ml
amount of HF in each cup:	1.0 ml
cook power:	70%
maximum cook time:	12 min.
degree of digestion:	100%
Wood (test for REE)	
numbers of cup in microwave oven:	12
mass of sample in each cup:	0.5-0.6 g
amount of HNO_3 in each cup:	3.0 ml
amount of H_2O in each cup:	2.0 ml
1st cook power:	50%
1st cook time:	20 min.
2nd cook power (after cool and air vented)	70%
2nd cook time:	20 min.
degree of digestion:	100%

Table 8.2 (continued)

Parameter	Value
Soil (from Brooklyn, New York)	
numbers of cup in microwave oven:	6
mass of sample in each cup:	50-60 mg
amount of HNO_3 in each cup:	2.0 ml
amount of HF in each cup:	2.0 ml
1st cook power:	70%
1st cook time:	12 min.
2nd cook power (after vent air and add 1 ml HF):	70%
2nd cook time:	12 min.
degree of digestion:	85-90%
Wood (tree rings from Brooklyn, NY)	
numbers of cup in microwave oven:	12
mass of sample in each cup:	0.15-0.30 g
amount of HNO_3 in each cup:	2.0 ml
amount of H_2O in each cup:	2.0 ml
cook power:	80%
cook time:	20 min.
degree of digestion:	100%

$HClO_4$, and placed into a bomb. The bomb was sealed and placed in an oven at 140 °C for 24 hours. After cooling in a refrigerator, the cup was taken out of the bomb and 2 ml of $HClO_4$ was added and the contents evaporated on hot plate. The evaporation was repeated once with the same amount of $HClO_4$ and twice with the same amount of HNO_3. The cup content was then quantitatively transferred to a polyethylene tube, Tl spiked and diluted to a suitable mass with 2% HNO_3. Soil was all converted to clear solution by this method.

The lead concentration of soil samples digested by both methods is listed in Table 8.3. Within experimental errors (t-test with 95% confidence level), there is no difference between the concentration of lead in soil digested by microwave oven and by conventional oven. It can be concluded that the lead was leached to solution completely when soil was digested by microwave dissolution system. Since the soil digestion efficiency for lead by microwave system was the same as that by conventional digestion method and the digestion time was much shorter for the former method, all the soil samples were digested by microwave oven.

Table 8.3 Comparison of digestion efficiency of soil using microwave oven (M) and conventional oven (C).

Method	Sample ID	A32	A24	F34	F8	F26
M	Pb conc.(ppm)	26.8±6.1	105.9±2.1	109.6±3.8	851.2±8.1	87.4±1.0
C	Pb conc.(ppm)	27.9±4.9	105.8±3.5	111.7±8.6	850.1±5.1	86.9±5.4

8.3 Sample analysis

The operating parameters of the ICP-MS were the same as those stated in Table 7.3. NIST 278 (Obsidian Rock) and NIST 1575 (Pine Needles) standard samples were analyzed along with soil and tree samples respectively to verify the accuracy of analysis of lead concentrations. Since there were more than 90 tree samples, they were run separately at different times. Samples from the same core were analyzed in the same time.

All $^{206}Pb/^{207}Pb$ ratios of lead in tree samples and soil samples were normalized by NIST 981 (Common Lead) standard which was analyzed together with the samples each time. The corrected $^{206}Pb/^{207}Pb$ ratio was obtained using the following equation:

$$R_{true}(sample) = R_{measure}(sample) \times \left\{\frac{R_{true}(NIST)}{R_{measure}(NIST)}\right\} \qquad (8.1)$$

where R represents the $^{206}Pb/^{207}Pb$ ratio.

Before samples were analyzed, the instrument was always tuned with NIST 981 standard to make the $^{206}Pb/^{207}Pb$ ratio close to 1.0933, the certified $^{206}Pb/^{207}Pb$ ratio. The significance of the tuning is to minimize the mass discrimination difference in the samples and in the standard so that Equation 8.1 is valid.

8.4 Results and discussion

The lead concentration and isotopic composition of the tree samples are summarized in Tables 8.4 and 8.5 respectively. Decrease in lead

Table 8.4 Concentration (ppb) of Pb found in tree cores from Brooklyn, New York.

year	tree #1	tree #2	tree #4	tree #5	tree #6
1952-53	4779±82	2748±15		2982±18	3905±46
1954-55	3936±37	4102±41		2500±10	3329±44
1956-57	4876±27	7255±97		3445±22	2742±55
1958-59	4480±34	7909±132		2831±22	2369±19
1960-61	5522±93	5662±32		3700±34	2283±8
1962-63	5420±41	11690±70		3967±15	2574±12
1964-65	4104±29	5976±58		4727±16	2747±32
1966-67	5323±16	5800±29		4842±33	3183±10
1968-69	4704±20	6878±25		3517±7	3178±17
1970-71	5818±14	6374±6	1115±26	5492±13	3054±99
1972-73	6042±12	5586±354	888±17	5859±19	2608±59
1974-75	6940±68	4877±108	861±30	6224±27	2323±30
1976-77	6901±46	4817±166	921±19	6317±23	2542±8
1978-79	6326±31	4162±101	713±59	6912±20	3410±94
1980-81	4080±15	3263±75	891±25	6078±50	2526±40
1982-83	5145±7	4116±143	830±31	6162±35	2901±87
1984-85	4368±12	4163±97	1058±60	1662±26	2732±8
1986-87	5124±25	2630±113	913±37	2272±5	3091±43
1988-89	4367±20	3083±28	638±23	1615±16	3322±56
1990-91	2805±31	3520±177	445±29	1366±14	1616±81

Table 8.5 Isotope ratios of $^{206}Pb/^{207}Pb$ (mean ± s.d.) in tree rings from Brooklyn, New York.

year	tree #1	tree #2	tree #4	tree #5	tree #6
1952-53	1.185±0.011	1.203±0.016		1.179±0.007	1.178±0.008
1954-55	1.202±0.006	1.208±0.015		1.183±0.005	1.181±0.013
1956-57	1.212±0.011	1.194±0.004		1.182±0.015	1.187±0.008
1958-59	1.215±0.049	1.198±0.004		1.183±0.007	1.182±0.003
1960-61	1.201±0.012	1.176±0.023		1.171±0.003	1.185±0.008
1962-63	1.208±0.006	1.194±0.036		1.166±0.003	1.177±0.006
1964-65	1.217±0.011	1.191±0.008		1.171±0.010	1.184±0.014
1966-67	1.196±0.010	1.198±0.013		1.176±0.012	1.170±0.017
1968-69	1.196±0.005	1.196±0.012	#####	1.176±0.006	1.174±0.012
1970-71	1.185±0.008	1.189±0.006	1.167±0.031	1.173±0.018	1.171±0.009
1972-73	1.177±0.012	1.200±0.014	1.187±0.030	1.177±0.000	1.176±0.012
1974-75	1.192±0.007	1.199±0.050	1.177±0.020	1.176±0.004	1.182±0.018
1976-77	1.182±0.007	*****	1.174±0.010	1.170±0.005	1.168±0.005
1978-79	1.181±0.002		1.194±0.028	1.173±0.009	1.172±0.005
1980-81	1.199±0.019		1.175±0.002	1.172±0.012	1.174±0.006
1982-83	1.199±0.008		1.194±0.020	1.173±0.001	1.180±0.018
1984-85	1.199±0.017		1.201±0.008	1.178±0.006	1.181±0.006
1986-87	1.199±0.003		1.193±0.014	1.198±0.007	1.171±0.017
1987-89	1.198±0.016		1.187±0.028	1.193±0.034	1.168±0.027
1990-91	1.187±0.026		1.153±0.023	1.199±0.015	1.191±0.015

***** --- data after 1977 are not listed because their standard deviations are greater than 0.10.

--- tree rings before 1969 are not clearly distinguishable so that they were not cut and analyzed.

concentration in recent years is the general trend of the concentration change as shown in Figures 8.2 and 8.3, in which the Pb concentration in trees versus their growth year are plotted. The Pb concentration in tree #1 and #5 reached a maximum in 1975 and 1979, respectively. We did not analyze the tree rings of Linden (tree #4) before 1969, but the Pb concentration in the tree presents the declining trend from 1971 to 1991. These results are consistent with historical trends in the consumption of lead in gasoline in the country (see Figure 8.4). The change of Pb concentration in tree rings studied reflected the chronological change of concentration of Pb emitted from automobiles. Although the Pb content in tree #2 reached the maximum in 1963, it decreased after 1969. The Pb concentration in the tree did not peak in the period between 1970 and 1980 probably due to the translocation of Pb in the tree.

In addition, Figure 8.2 also shows that Pb concentration in the trees collected on Ocean Parkway (a heavy traffic road) is higher than that collected on Dekoven Court (a dead end street). This is another piece of evidence that Pb in trees is primarily from gasoline. It is important to choose the same type of trees when the comparison is made of Pb concentration in different trees since the uptake rate of Pb may vary from tree to tree.

An attempt was made to relate the Pb concentration to the isotopic composition ($^{206}Pb/^{207}Pb$) in a single tree core. Unfortunately, the measured isotope ratios of $^{206}Pb/^{207}Pb$ in most rings of a tree are the same within our experiment errors.

To find the correlation between the isotopic composition in tree rings and in soil, we summarize the $^{206}Pb/^{207}Pb$ ratios in soil samples from digestion and from extraction in Table 8.6. Lead in soil can be divided into two types: plant-available lead and background (natural) lead. The former can be taken

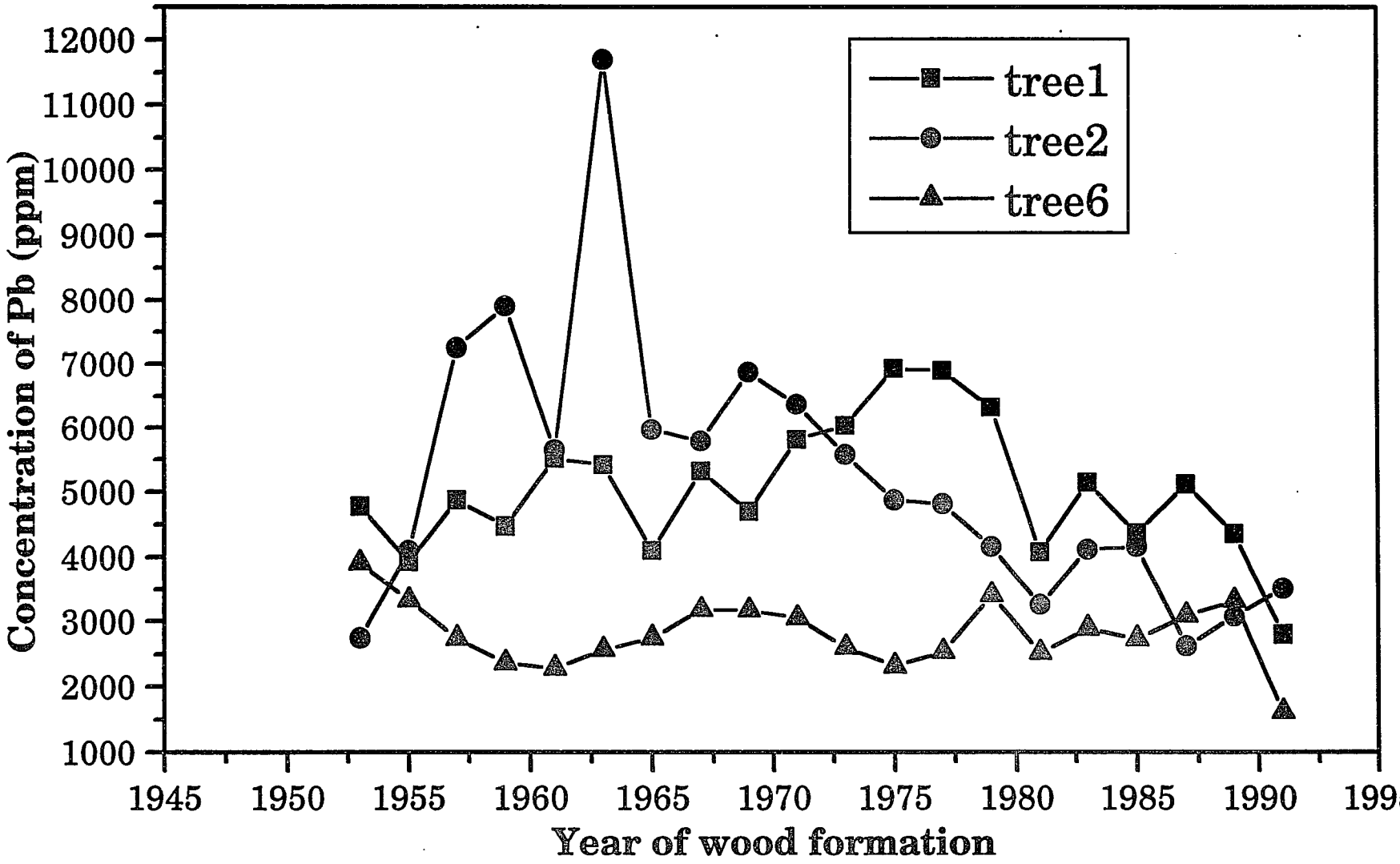

Figure 8.2 Change of Pb concentration in Norway maple with growth year.

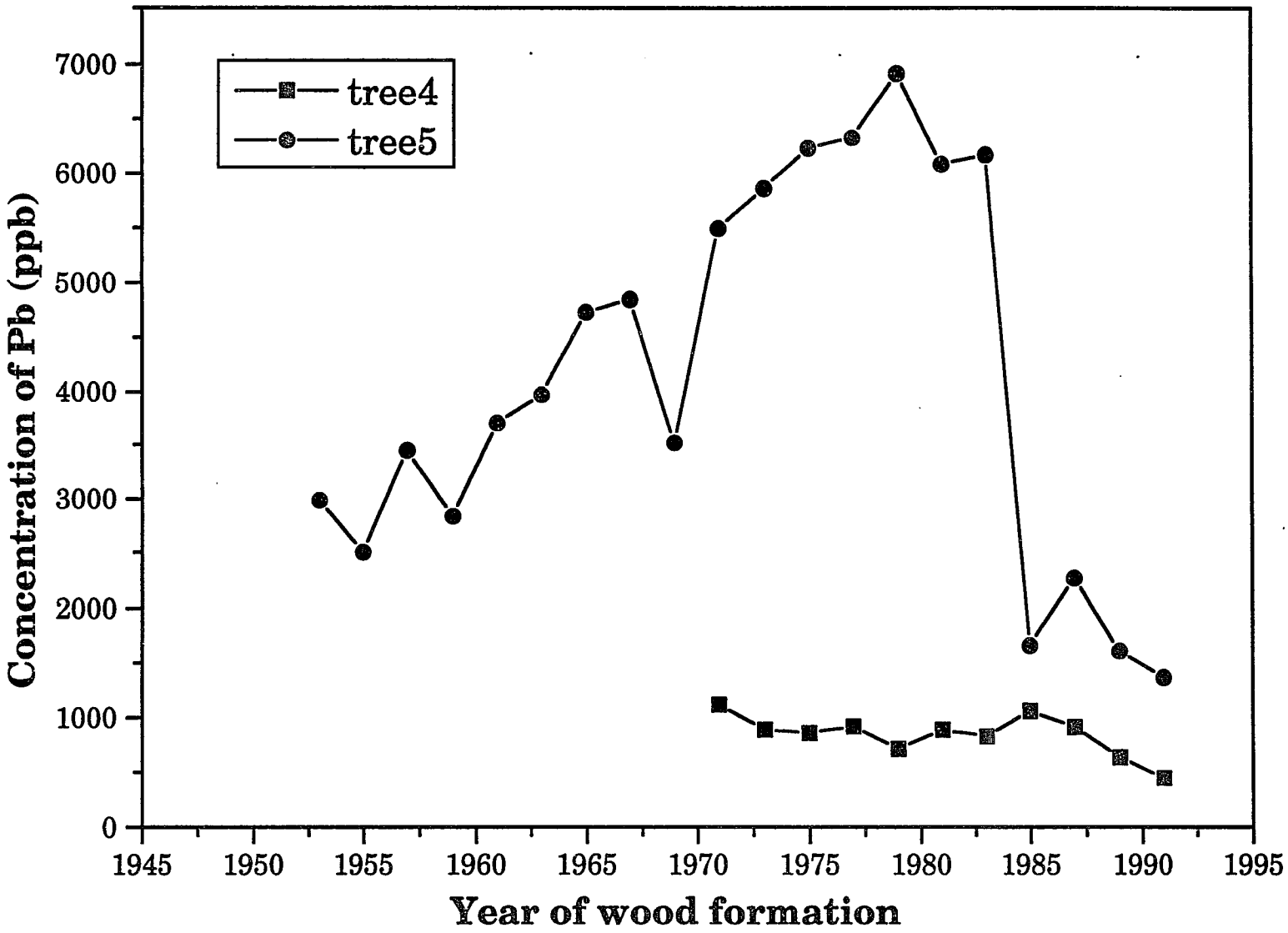

Figure 8.3 Change of Pb concentration in linden (tree #4) and London plane (tree #5).

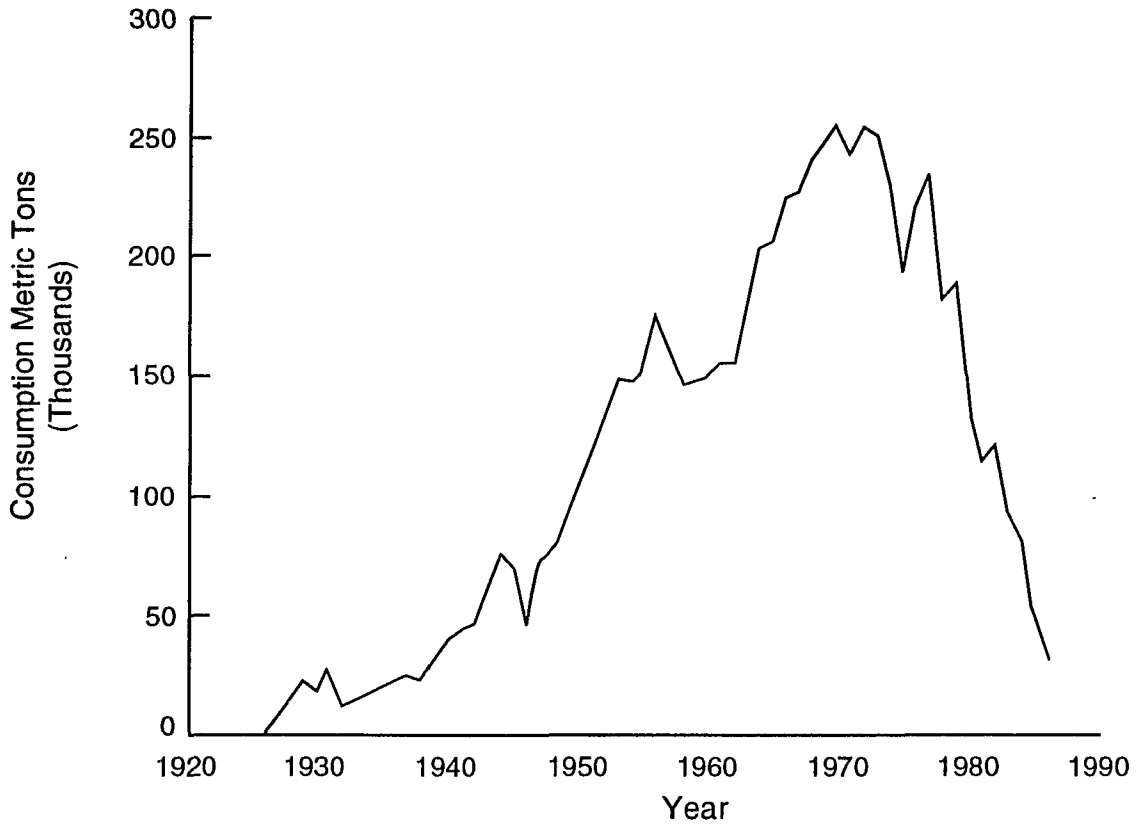

Figure 8.4 Historical trends in the consumption of lead in gasoline in the United States (from reference 100).

Table 8.6 Soil pH and concentration (ppm) and isotope ratio of Pb in soil[a] samples prepared by microwave digestion with HNO_3 and by extraction with 1.0 N HCl[b].

sample	soil#1, 4"	soil#1, 8"	soil#1, 12"	soil#1, 24"	soil#1, 32"
conc.	108.1±5.8	150.9±5.3	123.1±0.6	105.9±0.1	31.6±4.4
	(75.2±0.2)	(104.7±0.5)			
$^{206}Pb/^{207}Pb$	1.218±0.008	1.215±0.012	1.219±0.025	1.245±0.007	1.225±0.005
	(1.197±0.007)	(1.209±0.004)			
pH	6.24	6.28			

sample	soil#5, 4"	soil#5, 8"	soil#5, 12"	soil#5, 16"	soil#5, 20"
conc.	934.9±6.5	497.5±9.9	350.2±2.9	330±10.7	293.9±5.9
	(602.2±2.6)	(384.8±1.2)			
$^{206}Pb/^{207}Pb$	1.183±0.005	1.180±0.004	1.189±0.002	1.210±0.008	1.233±0.004
	(1.174±0.002)	(1.182±0.007)			
pH	6.22	5.88			

a ---- sample ID is the same as tree-ring sample ID, e.g. soil #1 was collected under tree #1; number after sample ID represents the depth from which soil sample was collected.

b ---- the values in parentheses represent the data obtained from extraction process.

Table 8.6 (continued)

sample	soil#6, 4"	soil#6, 8"	soil#6, 16"	soil#6, 26"	soil#6, 34"
conc.	526.5±8.2	853.9±5.6	240.2±7.5	87.2±0.4	104.7±5.8
	(484.4±2.0)	(724.9±1.6)			
$^{206}Pb/^{207}Pb$	1.186±0.004	1.181±0.005	1.182±0.003	1.189±0.008	1.192±0.008
	(1.184±0.002)	(1.176±0.003)			
pH	5.54	5.42			

sample	soil#2, 4"	soil#4, 4"
conc.	192.8±4.9	129.3±3.6
	(132.3±0.5)	(124.4±0.3)
$^{206}Pb/^{207}Pb$	1.204±0.003	1.191±0.017
	(1.201±0.001)	(1.176±0.006)
pH	5.06	6.42

up by plants through extraction and/or diffusion. The fraction of lead extracted from the soil by 1.0 N HCl may represent the plant-available lead [101]. The total lead content in the soil samples were obtained by acid digestion. It is observed that lead concentration in soil generally decreases with sampling depth (see Table 8.6). On the other hand, $^{206}Pb/^{207}Pb$ ratio in soil increases with sampling depth. The two trends indicate that the soil close to ground level were contaminated by lead from automobile exhausts. Gasoline Pb is produced from ore bodies whose isotopic composition differs from that of Pb in rocks. During the formation of ore bodies, Pb is separated from U so that ^{206}Pb, derived from ^{238}U decay, is no longer accumulated after the ore is formed. Consequently $^{206}Pb/^{207}Pb$ ratio in most Pb ores are lower than in most bed-rock, where accumulation of ^{206}Pb has continued. Radioactive accumulation of ^{207}Pb is minor during the last billion years since its parent, ^{235}U, possesses a 0.7 billion year half-life and has essentially decayed. Therefore, the $^{206}Pb/^{207}Pb$ ratio in uncontaminated soil is greater than that in the soil close to the surface which has been contaminated by leaded gasoline. The $^{206}Pb/^{207}Pb$ ratio of lead as an additive in gasoline in New York City in 1967 was 1.165 (one sample) [102]. The value is closer to the isotopic compositions of plant-available lead than the corresponding isotopic compositions of total lead in soil. The plant-available lead consists of the Pb from pollutants and original lead. The $^{206}Pb/^{207}Pb$ ratio of the plant-available lead actually is the ratio of mixed lead. Therefore, there is slight difference between the ratios in gasoline and in soil samples prepared by extraction.

The Student's t-test was used to compare the ratios in tree rings to those in soil in 4 to 8 inch depth where the root zones were located. All comparisons were performed at the 95% confidence level. The result is listed in Table 8.7.

The values in the table represent numbers of "no significant different" mean divided by total number of tested mean. The $^{206}Pb/^{207}Pb$ ratios in tree rings correlate well with those of plant-available Pb in soil.

Tables 8.4 and 8.6 show that the concentration of Pb in tree #1 and tree #2 are higher than that in tree #6, but the acidity, represented by pH, and Pb concentration in soil under tree #6 are higher than those under tree #1 and #2. Probably some portion of Pb was absorbed by trees #1 and #2 via deposition on leaves or bark. Since trees #1 and #2 are located on a heavy traffic street, they are exposed to aerosol lead more severely than the tree on the dead-end street.

On the basis of these experiments, we conclude that tree rings "store" the chronological record of lead pollution. Due to the use of unleaded gasoline in recent years the concentration of Pb in tree rings has decreased. By comparing the $^{206}Pb/^{207}Pb$ ratios in tree rings to those in soil and in leaded gasoline, it is safe to say that Pb in tree rings is mainly from leaded gasoline.

Table 8.8 Correlation between the isotopic composition in tree rings and in soil. *

sample	tree #1	tree #2	tree #4	tree #5	tree #6
soil #1, 4"	**85%**, *55%*				
soil #1, 8"	**60%**, *65%*				
soil #2, 4"		**83%**, *75%*			
soil #4, 4"			**91%**, *91%*		
soil #5, 4"				**85%**, *65%*	
soil #5, 8"				**90%**, *85%*	
soil #6, 4"					**85%**, *85%*
soil #6, 8"					**100%**, *95%*

* ----- use Student's t-test (CL=95%) to compare $^{206}Pb/^{207}Pb$ ratio in each ring in a tree to $^{206}Pb/^{207}Pb$ ratio in soil. The values in the table represent number of "not significant different" mean divided by total number of tested mean. **Bold** values indicate correlation between tree rings and soil prepared by extraction and *italic* values represent correlation between tree rings and soil prepared by digestion.

Chapter 9 Determination of geographical origin of archaeological samples by cluster analysis of the ratios of rare earth elements

An Indian reservation was located in Chaco Canyon, Arizona where American Indians used to live a few hundred years ago. Many tree logs were found in that reservation in 1989. These trees are believed to have been cut by Indians. However, Chaco Canyon is not considered the original site where the trees grew. Archaeologists are interested in the geographical origin of these trees which may allow them to trace the Indians' migration routes.

A powerful method for the determination of the geographical origin of archaeological samples is multivariate statistical analysis of the multielemental analytical data. This methodology has been used to determine the geographical origins of orange juice [109], pottery [110], honey [111], and wine [112, 113]. The experiments showed that the method is essentially helpful when the number of components that serve to differentiate samples from different geographical origin is reasonably large.

In this experiment, we applied cluster analysis, one of the multivariate methods, to determine the geographical origin of trees obtained from Chaco Canyon sites. We chose rare earth elements as analyzed components since pollution to the tree growth environment by these elements is almost negligible relative to other elements. We assumed that the ratios of REEs in the soils where the trees grew are constant and the soils from different geographical areas have different REEs ratios. Rare earth elements, along with other elements, must be absorbed by the trees from the soil in which they grew. It is known that the levels of elements present in tree tissue is directly dependent on the levels of these elements in their growth media

[114] such as soil. The ratios of REEs thus form a characteristic pattern relating to the geographical origins of the trees.

9.1 Experimental

The trees from Chaco Canyon sites had been cut in small wedges before they were brought to our laboratory. There are 13 trees studied. Two or more than two samples were collected from each tree. The names of the samples are listed in Table 9.1.

All samples were prepared for analysis by microwave digestion using an MDS-81D microwave digestion system (CEM). The wedge of the tree was cut into a small "V" shaped piece using an electric saw. All the surfaces of the samples were cleaned by cutting with the saw. The sample sizes varied from 0.5 g to 0.6 g. Samples were weighed into 120 ml Teflon digestion vessels, and 3 ml of concentrated HNO_3 and 2 ml of deionized H_2O were added to each sample. Twelve samples were heated in the digestion system at one time using the appropriate program as listed in Table 8.2. After digestion the vessel contents were transferred to 20 ml polyethylene vials and diluted to 15 ml with deionized H_2O.

To examine if trees growing in the same area have the same ratios of rare earth elements, we collected some tree samples from Brooklyn, New York. The sampling sites and sample code numbers are listed in Table 9.2.

The cores were collected with a Teflon coated coring tool. The tool was screwed into the tree at breast height and a core about 3 mm in diameter and 25 cm long was removed and stored in a plastic bag. In our laboratory, the cores were dried at 70 ^{o}C in an oven for 12 hours. The cores were then

Table 9.1 The tree samples collected from the trees from Chaco Canyon.

tree ID number	number of samples	sample ID number
JPB137	2	JPB137-1a, JPB137-2a
JPB147	2	JPB147, JPB147-R
JPB133	2	JPB133-2, JPB133-7
DPB7	2	DPB7, DPB7-R
HP13	2	HP13-L, HP13-R
CK707	2	CK707-1a, CK707-2a
CK718	2	CK718-L, CK718-R
CK761	2	CK761-L, CK761-R
CK838	2	CK838-1a, CK838-2a
CK853	2	CK853-a1, CK853-a2
CK868	2	CK868-1a, CK868-2a
CK893	2	CK893, CK893-L2
GP218	5	GP218-18, GP218-6, GP218-6L, GP218-13, GP218-6R

Table 9.2 Brooklyn tree cores used for cluster analysis.

location	number of cores	sample ID
1060 East 24 Street	3	tn8076, tn8581, tn9086
1052 East 24 Street	3	ts8076, ts8581, ts9086
3088 Bedford Avenue	3	30889086, 30888581, 3088mix
1241 East 23 Street	2	12411, 12412

separated with a stainless steel blade. The sample size was about 0.5 gram. The samples were digested in the same manner as done for the tree samples from Chaco Canyon.

The sample solutions were analyzed on the instrument under the operating conditions as shown in Table 6.1 except that the scan range was 138.5 amu to 177 amu. Since the maximum concentration of REEs in the sample solutions was less than 5 ppb, interferences of rare earth oxides (see Chapter 5) were neglected.

9.2 Cluster analysis

The intensities of rare earth elements in each tree sample are shown in Table 9.3. From the table, we note that the intensities of the Er, Tm, Yb, and Lu are very low. The ratios from these elements can not be used as variables for cluster analysis. According to the result of our preliminary discriminant analysis, we chose the following REEs' ratios as variables for cluster analysis:

Ce/La, Pr/La, Nd/La, Sm/La, Gd/La, Eu/La, Ho/La, Nd/Pr, Sm/La, Eu/Pr, Gd/Pr, Nd/Ce, Gd/Ce, Ho/Tb, and Tb/Pr.

The cluster analysis was performed on a UNIX system through an IBM 486 personal computer using SAS Ward's minimum variance. The maximum number of clusters was determined by the cubic clustering criterion (ccc). A plot of cubic clustering criterion versus number of clusters is shown in Figure 9.1. The possible number of clusters is indicated by the maxima, i.e., 3 or 6. The six clusters were selected in our analysis because the data shown in Table 9.3 reveals that at least 4 different groupings among the tree samples: one from Brooklyn and three from Chaco Canyon. The three groupings of tree

samples from Chaco Canyon are differentiated by their intensities: high concentration in REEs, low concentration in REEs, and high concentration in light REEs but low in heavy REEs.

The results of the cluster analysis are shown in Table 9.4. With the data obtained from Table 9.4, we constructed a Dendrogram (Figure 9.2).

9.3 Results and discussion

There are 40 samples from 16 different trees. Originally, we planned to use control samples from Chaco Canyon to distinguish the geographical origins of the 13 trees. Unfortunately, the control samples were not available. This section is therefore focused on whether the cluster analysis of REEs' ratios in the tree is able to determine the geographical origin of the trees.

Since two or more than two samples were collected from each tree, the samples from the same tree should not belong to different clusters. Table 9.4c shows that most samples are satisfied with this requirement. All the samples from Brooklyn are clustered in one grouping (Cluster 1). The samples from the trees located on East 24 street are even clustered in one subgrouping (see Figure 9.2). Trees from Brooklyn are distinguished from the trees from Chaco Canyon except two samples. Among the 40 samples, only six pairs of samples are divided into different clusters. These sample pairs are CK853-a1, CK853-a2; CK761-L, CK761-R; CK893-L2, CK893; JPB133-2, JPB133-7; CK718-L, CK718-R; and CK838-1a, CK838-2a (the samples with asterisk in Table 9.4c). Carefully checking the intensities of these samples in Table 9.3, we found that the intensities of heavy REEs (after Nd) in six samples (CK838-1a, CK838-2a, CK853-a2, CK893, CK718L, and JPB133-7) were low. The

ratios of REEs in these samples have great uncertainties and obfuscate the clustering of the samples. The intensities of REEs in tree CK761 are not low. But the two samples from that tree belong to different clusters (Cluster 2 and Cluster 3). In addition, samples of JPB137-1a and JPB137-2a are not classified in the same subgrouping. The reason for the wrong clustering of these samples is that rare earth elements did not distribute homogeneously in the trees. In other word, the ratios of REEs in different cores of a tree are not constant.

In conclusion, it is possible to determine the geographical origins of trees by cluster analysis of REEs ratios. For the samples containing low concentrations of REEs, one should increase the sample weight to increase the intensities. For statistical reasons, it is better to collect more than two samples from each tree. For example, we collected five samples from the tree with ID number of GP218. Since four out of five samples are clustered in one grouping (cluster 3), we know that the tree should belong to cluster 3. We should have ground or sawed each tree log in powder and mixed the sample (from the same tree) well to avoid non-homogeneous distribution of REEs.

Table 9.3 Intensities of rare earth elements obtained from ICP-MS.

Sample	^{139}La	^{149}Ce	^{141}Pr	^{146}Nd	^{147}Sm	^{151}Eu	^{157}Gd	^{159}Tb	^{163}Dy	^{165}Ho
12411	5915	3457	942	571	68	58	119	75	72	61
12412	12476	8335	2167	1520	227	145	305	209	216	132
30888581	2741	1706	410	230	17	23	36	29	17	22
30889086	4383	2897	611	339	58	78	54	29	48	28
3088mix	2727	1679	477	339	45	34	61	49	51	29
CK707-1a	1638	2472	258	102	20	18	28	7	23	14
CK707-2a	1561	2528	269	127	40	29	25	23	31	36
CK718-L	864	1072	217	132	11	94	31	14	20	7
CK718-R	44399	93373	14314	10002	1710	1228	1706	1442	1803	1321
CK761-L	1975	3948	565	491	115	140	143	132	196	153
CK761-R	2583	5593	825	643	124	162	117	119	169	160
CK838-1a	954	1329	181	97	6	109	19	27	18	22
CK838-2a	728	852	108	48	7	167	22	13	15	5
CK853-a1	3210	3405	600	413	34	92	76	45	83	40
CK853-a2	2169	2079	418	159	21	82	38	28	37	19
CK868-1a	2039	6913	495	228	38	66	39	40	54	23
CK868-2a	1386	2258	382	149	18	61	33	28	29	18
CK893	394	869	175	132	16	26	26	53	53	53
CK893-L2	542	1160	195	143	38	36	35	22	58	35
DPB7	6449	13049	2116	1616	256	367	361	269	401	306
DPB7-R	20708	43063	6863	4934	975	884	1082	914	1218	934
GP218-13	65226	148459	21965	18568	3041	2227	3769	3399	4646	3394
GP218-18	25949	64951	10094	8735	1654	1398	2233	1999	2779	2008
GP218-6	7458	17205	2707	2402	476	410	601	615	905	672
GP218-6L	9047	21482	3415	2748	586	479	633	622	899	643
HP13-L	636	1231	175	106	18	24	33	17	17	14
HP13-R	695	1327	199	136	24	24	24	21	18	28
JPB133-2	6420	10999	1527	1040	149	122	202	145	186	130
JPB133-7	615	1010	134	71	4	12	10	10	10	10
JPB137-1a	3084	2202	489	211	45	55	47	37	43	27
JPB137-2a	5973	3507	895	541	78	82	81	73	85	57
JPB147	944	1796	227	164	15	32	25	27	26	23
JPB147-R	1145	2505	362	266	45	30	52	36	31	30
GP218-6R	14095	33835	5371	4536	1036	779	1224	1055	1496	1292
tn8076	37101	18198	7188	4927	642	472	911	619	629	421
tn8581	12797	7675	2406	1680	271	175	316	296	300	206
tn9086	6046	3446	1204	848	104	71	116	100	132	89
ts8076	15306	7265	2589	1672	220	163	269	204	165	98
ts8581	15545	5964	2607	1693	233	175	253	163	161	108
ts9086	9586	4286	1625	1081	165	118	163	139	128	51

Table 9.4a Results of cluster analysis using Ward's method.

Ward's Minimum Variance Cluster Analysis

Eigenvalues of the Covariance Matrix

	Eigenvalue	Difference	Proportion	Cumulative
1	8.01793	5.58936	0.57271	0.57271
2	2.42856	0.75669	0.17347	0.74618
3	1.67187	0.91432	0.11942	0.86560
4	0.75755	0.32065	0.05411	0.91971
5	0.43690	0.20464	0.03121	0.95092
6	0.23226	0.03577	0.01659	0.96751
7	0.19649	0.04462	0.01404	0.98154
8	0.15187	0.08872	0.01085	0.99239
9	0.06315	0.04790	0.00451	0.99690
10	0.01525	0.00091	0.00109	0.99799
11	0.01434	0.00535	0.00102	0.99901
12	0.00899	0.00528	0.00064	0.99965
13	0.00371	0.00259	0.00027	0.99992
14	0.00112	.	0.00080	1.00000

Root-Mean-Square Total-Sample Standard Deviation = 1

Root-Mean-Square Distance Between Observations = 5.291503

Table 9.4b Results of cluster analysis using Ward's method (continued).

Number of clusters	clusters joined		frequency of new cluster	semipatial R-squared
39	12412	3088mix	2	0.000263
37	ts8076	ts9086	2	0.000403
38	CK718-R	JPB147-R	2	0.000535
36	CL39	tn8581	3	0.000776
35	GP218-18	GP218-6	2	0.000791
34	12411	JPB137-2a	2	0.000830
33	DPB7	DPB7-R	2	0.000836
32	tn8076	ts8581	2	0.000985
31	CL35	GP218-6R	3	0.001253
30	CL32	tn9086	3	0.001287
29	JPB133-2	JPB147	2	0.001362
28	30889086	JPB137-1a	2	0.001636
27	CL34	30888581	3	0.001717
26	CL33	GP218-13	3	0.001790
25	CK853-a2	CK868-2a	2	0.001942
24	CK761-R	CL26	4	0.002617
23	CL31	GP218-6L	4	0.002671
22	CL30	CL38	5	0.002765
21	CL27	CK853-a1	4	0.003285
20	CL37	HP13-R	3	0.003857
19	CL25	JPB133-7	3	0.003961
18	CL21	CL28	6	0.004753
17	HP13-L	CL29	3	0.005125
16	CL36	CL22	8	0.005821
15	CK707-1a	CK707-2a	2	0.005932
14	CK761-L	CL23	5	0.006401
13	CK718-L	[illegible]8-1a	2	0.006430
12	CL20	[illegible]7	6	0.006999
11	CL24	[illegible]K893-L2	5	0.009699
10	CL19	CK868-1a	4	0.011339
9	CL13	CL10	6	0.022995
8	CL14	CK893	6	0.024503
7	CL18	CL16	14	0.028656
6	CL12	CL11	11	0.033585
5	CL15	CL9	8	0.043099
4	CL7	CL5	22	0.089760
3	CL6	CL8	17	0.107554
2	CL4	CK838-2a	23	0.121653
1	CL2	CL3	40	0.430134

Table 9.4c Results of cluster analysis using Ward's method (continued).

Sample ID	Clusters
12411	1
12412	1
3088mix	1
30889086	1
30888581	1
ts9086	1
ts8581	1
ts8076	1
tn9086	1
tn8581	1
tn8076	1
JPB137-1a	1
JPB137-2a	1
CK853-a1*	1
CK853-a2*	4
JPB147	2
JPB147-R	2
DPB7	2
DPB7-R	2
HP13-L	2
HP13-R	2
CK761-L*	3
CK761-R*	2
CK893-L2*	2
CK893*	3
JPB133-2*	2
JPB133-7*	4
CK718-L*	4
CK718-R*	2
GP218-18	3
GP218-6	3
GP218-6R	3
GP218-13	2
GP218-6L	3
CK868-1a	4
CK868-2a	4
CK838-1a	4
CK838-2a*	6
CK707-1a	5
CK707-2a	5

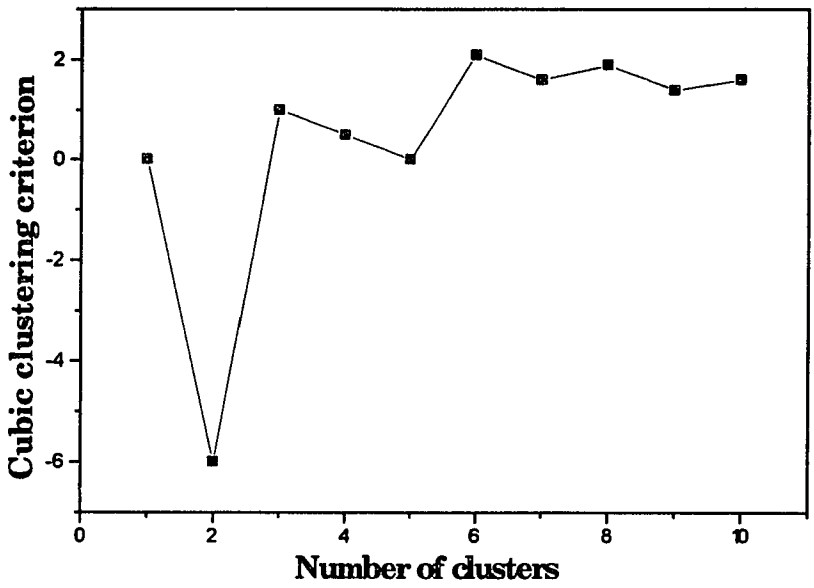

Figure 9.1 Determination of probable cluster number by cubic clustering criterion method.

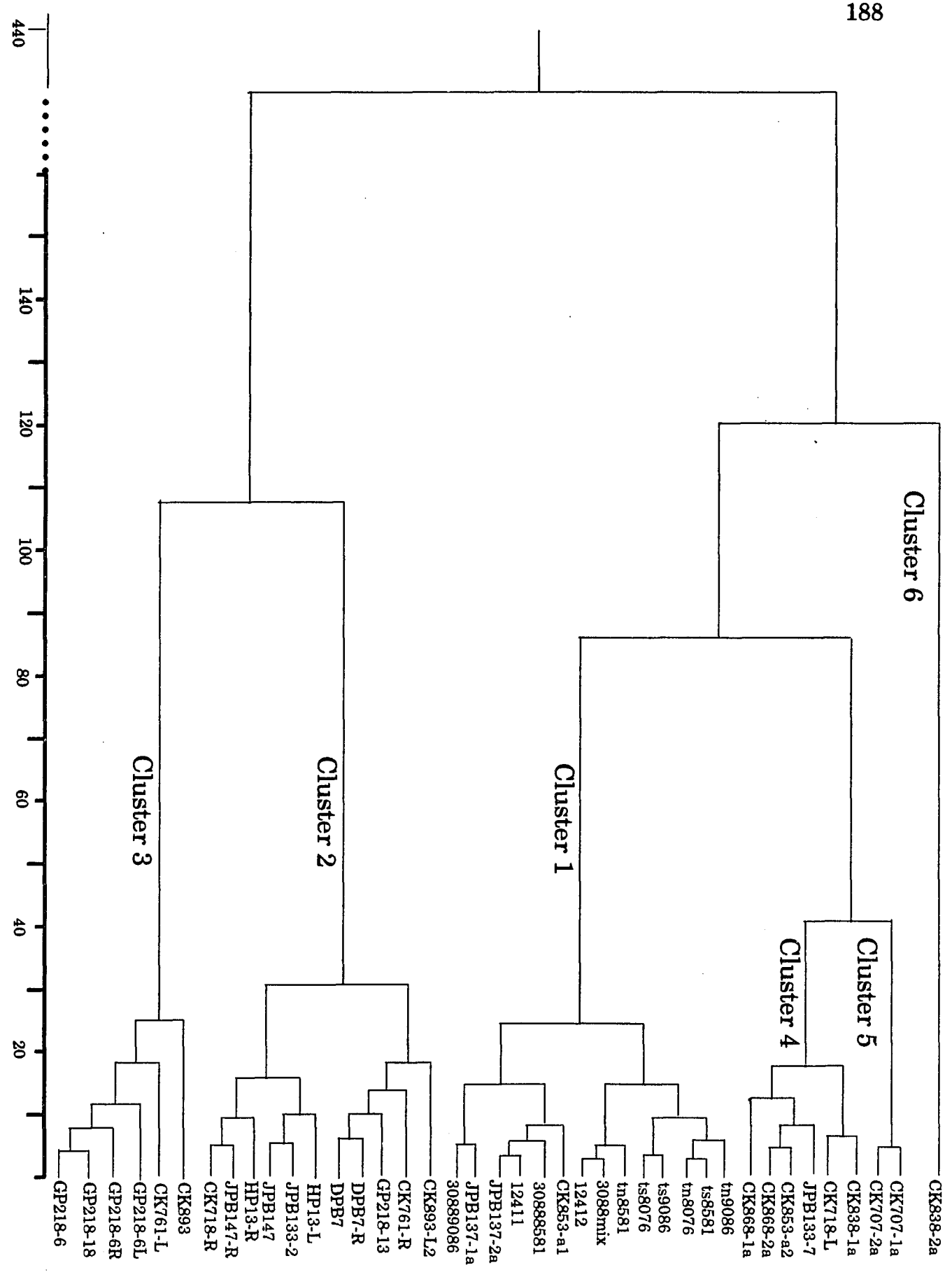

Figure 9.2 Dendrogram of wood samples tabulated from the data in Figure 9.4b.

Appendix I Analysis of metals in annual-growth rings in New York City tree by proton induced X-ray emission

A.1 Introduction

X-rays were discovered by Röntgen in 1895 [29]. Interest in using characteristic X-rays for chemical analysis arose in 1913 as a result of Moseley's study on the relationship between an element's characteristic spectrum and its atomic number [115]. With development of high-resolution, solid state, energy-dispersive photon detectors, a relatively new method based on determination of characteristic X-rays emitted from analyzed target, proton-induced X-ray emission (PIXE) has been available to analytical chemists since 1970 [116].

It has been reported that PIXE detection limits can be as low as 0.1 to 0.01pg using a thin sample backing and a beam with a diameter of 1 mm [117]. A precision of 2-3% and an accuracy of 5-10% can be attained with some care. Moreover, the samples analyzed by the PIXE method in some cases are non-destructive and analysis time is short. The advantages make the method comparable to other analytical methods such as AAS, NAA, ICP, DCP, and XRF in dendrochemical analysis.

The first dendrochemical analysis began in the 1960s. Recently, the study of trace elements in tree rings by PIXE are focused on the extent to which tree has been exposed to pollutants over its life span [118, 119, 120]. The studies have shown that it is possible to determine a "pollution chronology" for some elements. For example, in the case of a tree which absorbs lead and is at least fifty years old and is situated in an area impacted by motor vehicle exhaust, it should be possible to see significant changes in lead concentration

in the growth rings. So far the analyzed tree rings were limited to the trees collected from suburban areas or forests. It is necessary to study the chronological change of metals in trees growing in urban areas to see whether the results are consistent with those previous studied.

This research was undertaken to determine the concentration of trace elements in annual-growth rings of tree collected from inner New York City area. We were especially interested in the change of lead in rings. We expected a decrease in Pb concentration in recent years due to the increasing use of unleaded gasoline.

A.2 Conceptual basis of the PIXE method

PIXE analysis involves a bombardment of target atoms to be analyzed by charged particles, usually protons of 2 to 3 MeV. Being used as bombarding particles, protons are advantageous compared to other particles, such as electrons, because a proton microprobe is more sensitive than electron microprobe due to the low bremsstrahlung from protons.

When an energetic proton passes through a target atom it loses most of its energy through interaction with atomic electrons producing excitation and ionization. The inner-shell, usually a K-shell or L-shell, ionization creates a vacancy which may be filled by an electron from an outer shell, accompanied by the emission of an X-ray with energy $E_{x\text{-}ray} = E_f - E_i$, where E_f and E_i represent the energies of the final and initial electron energy states. Figure A.1 shows the brief scheme of X-ray emission caused by proton impact.

The energies of the bound electrons depend essentially on the principal quantum number n. The shells corresponding to n = 1, 2, 3, ... are called K, L, M, ... shell respectively. If the transition is between the L and K shells, a K_α

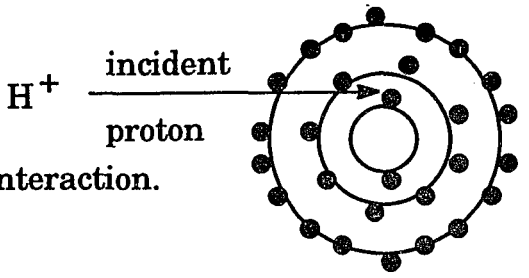

a) Proton- atom interaction.

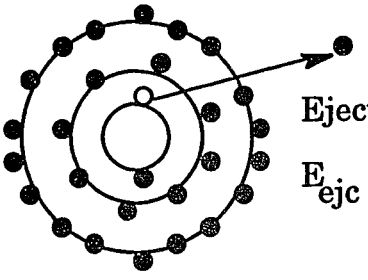

b) Proton energy absorbed by K- shell, ejecting an electron .

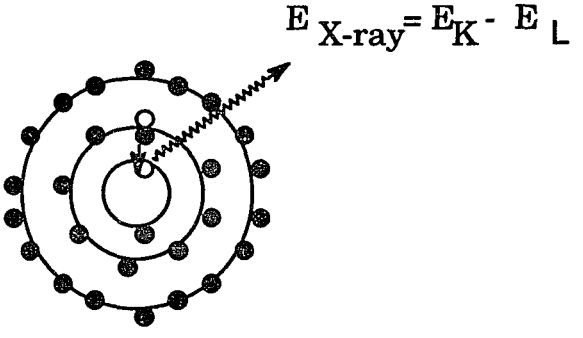

c) Outer shell electron fills into the vacant K-shell emitting a charateristic X-ray.

Figure A.1 X-ray emission induced by proton.

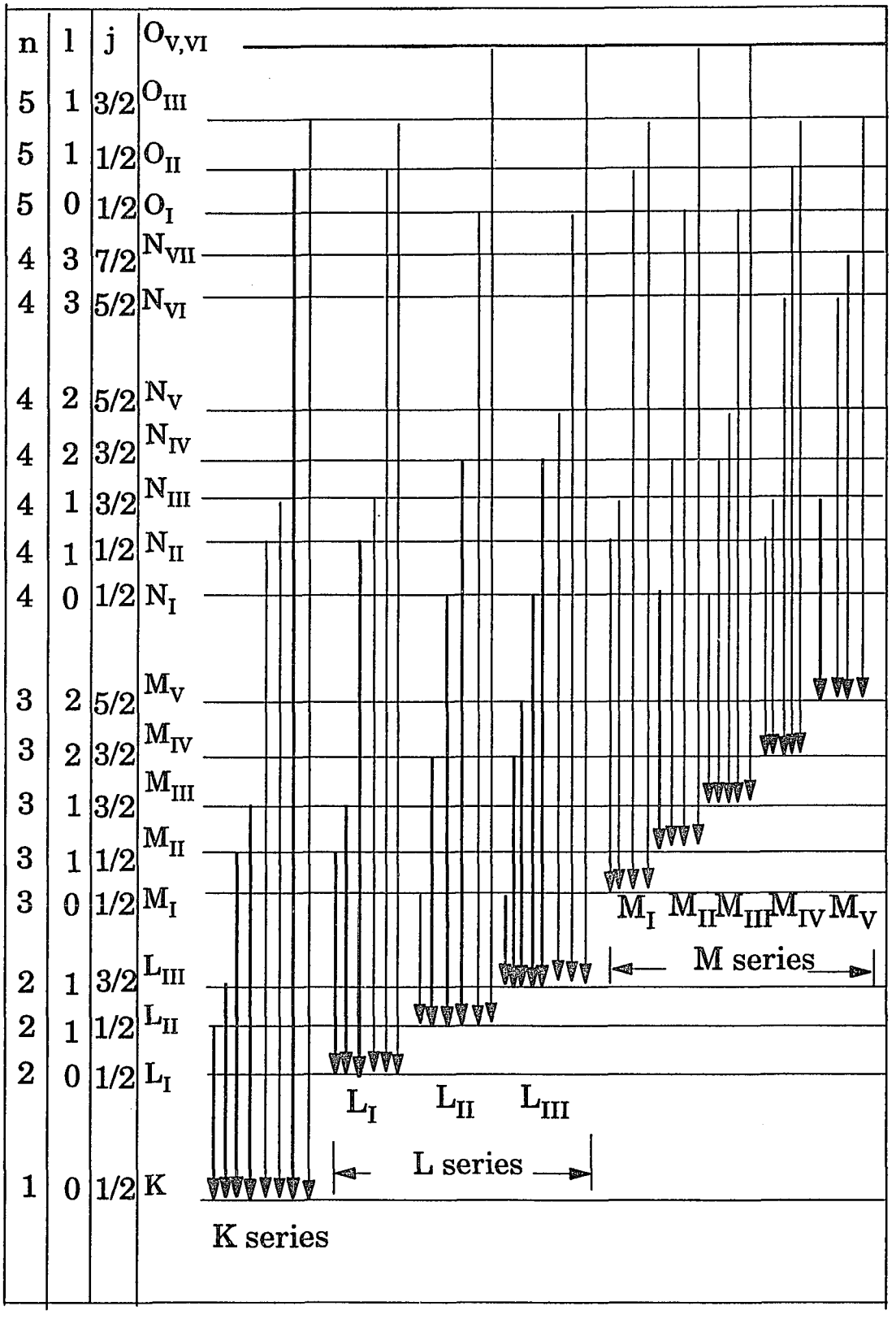

Figure A.2 Energy level diagram and possible transitions (from ref. 121).

line of the K series will be emitted; if the transition is between the M and K shells, a K_β line is emitted. The complete electron transitions are schematically represented in Figure A.2. The energy of X-ray emitted is characteristic of the elements. The region between 0.62 to 62 keV is most appropriate to PIXE analysis of the elements fluorine through uranium.

The ratio of the number of primary vacancies filled, giving rise to X-ray emission, to the number of initial vacancies created is termed the fluorescence yield (ω). The fluorescence yield of an element is a function both of the atomic number Z and the shell where the initial vacancy takes place. The value of the fluorescence yield is always less than one due to a competing type of transition known as the Auger effect. In the Auger effect, the energy of X-ray released in the transition of an outer shell electron to an initial inner shell vacancy ejects a second outer-shell electron, known as an Auger electron. The energy of the Auger electron is equal to the energy difference between the energy released due to the initial electron transition and the binding energy of the Auger electron. The schematic process of the Auger effect is shown in Figure A.3. For low Z elements, the emission of Auger electrons predominates. At higher atomic numbers the probability of the vacancies being filled and accompanied by the emission of X-rays increases. The Auger effect is one of the reasons for the low sensitivity for the light elements in PIXE analysis.

Another important factor in PIXE is X-ray ionization cross-section, which can be obtained either from experimental data or from theoretical studies. Actual calculations of ionization cross-sections are quite complex. Two approximate calculations, the Plane Wave Born Approximation (PWBA) [122] and the Binary Encounter Approximation (BEA) [123] have been developed.

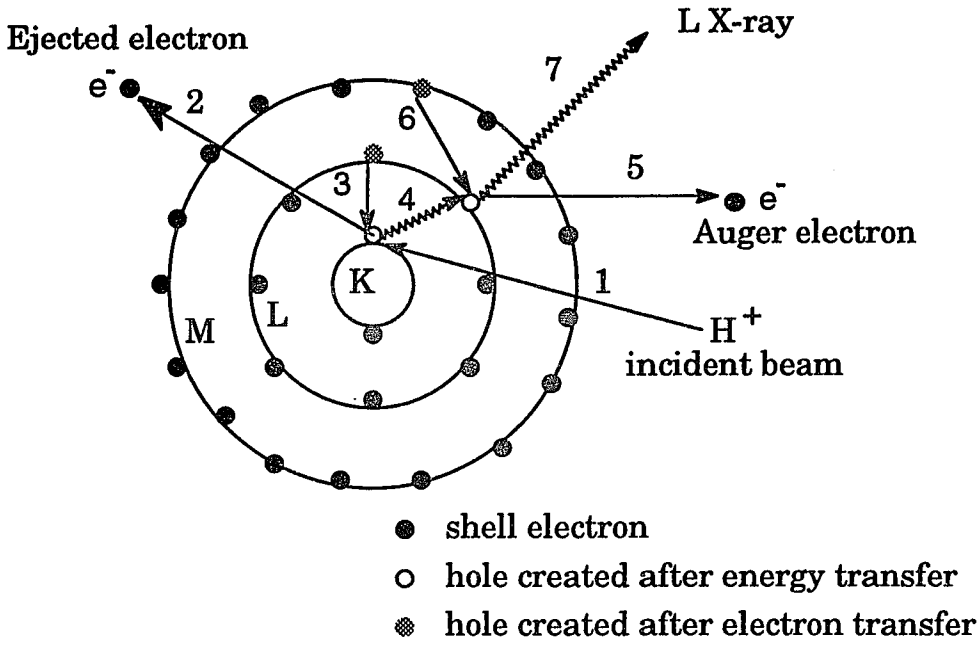

Figure A.3 Schematic representation of the Auger effect [ref. A.10].

Incident beam (1) transfers energy to the K-shell, ejecting an electron (2). Transition of an electron from L-shell (3) into the K-shell vacancy results in a K_α X-ray emission (4). K_α X-ray energy is absorbed by L-shell releasing an Auger electron (5). Transition of an electron from M-shell to L-shell (6) releases an L_α X-ray (7).

Generally, the element with greater total cross-section is more sensitive to PIXE analysis.

A.3 Instrumentation of PIXE

A.3.1 Accelerator

The accelerator used for our experiments is a Dynamitron accelerator (Radiation Dynamics Corp.). Figure A.4 shows the general layout of the Dynamitron. The accelerator operates at accelerating voltages between 0.5 and 3.75 MeV with a maximum current of 2 mA. The beam energy can be maintained within ±1.5 keV over the whole operating proton energy range.

The protons are produced by arc in the ion source located in the rear of the accelerator. The H^+ ions along with H_2^+ and H_3^+ are extracted from the ion source and accelerated through the 9.5 feet-long accelerating tube according to the applied potential difference. There is a total of 74 solid state rectifiers, each of which operates at a maximum output of 50,000 volts. The incoming beam is deflected by two 60°-bending magnets. A pair of slits located at the entrance of the first bending magnet defines the direction of the incoming particles. The other pair of slits following the second bending defines the direction of the outgoing particles. In PIXE operation, by adjusting the magnitude of the magnetic fields, only H^+ ions with certain energy can pass through the magnets and reach the target chamber.

A.3.2 The target chamber

In order to ensure that the entire sample is subjected to a uniform flux of protons of equal velocity, the proton beam is defocused and collimated before it emerges from the high vacuum of the beam transport system. Defocusing

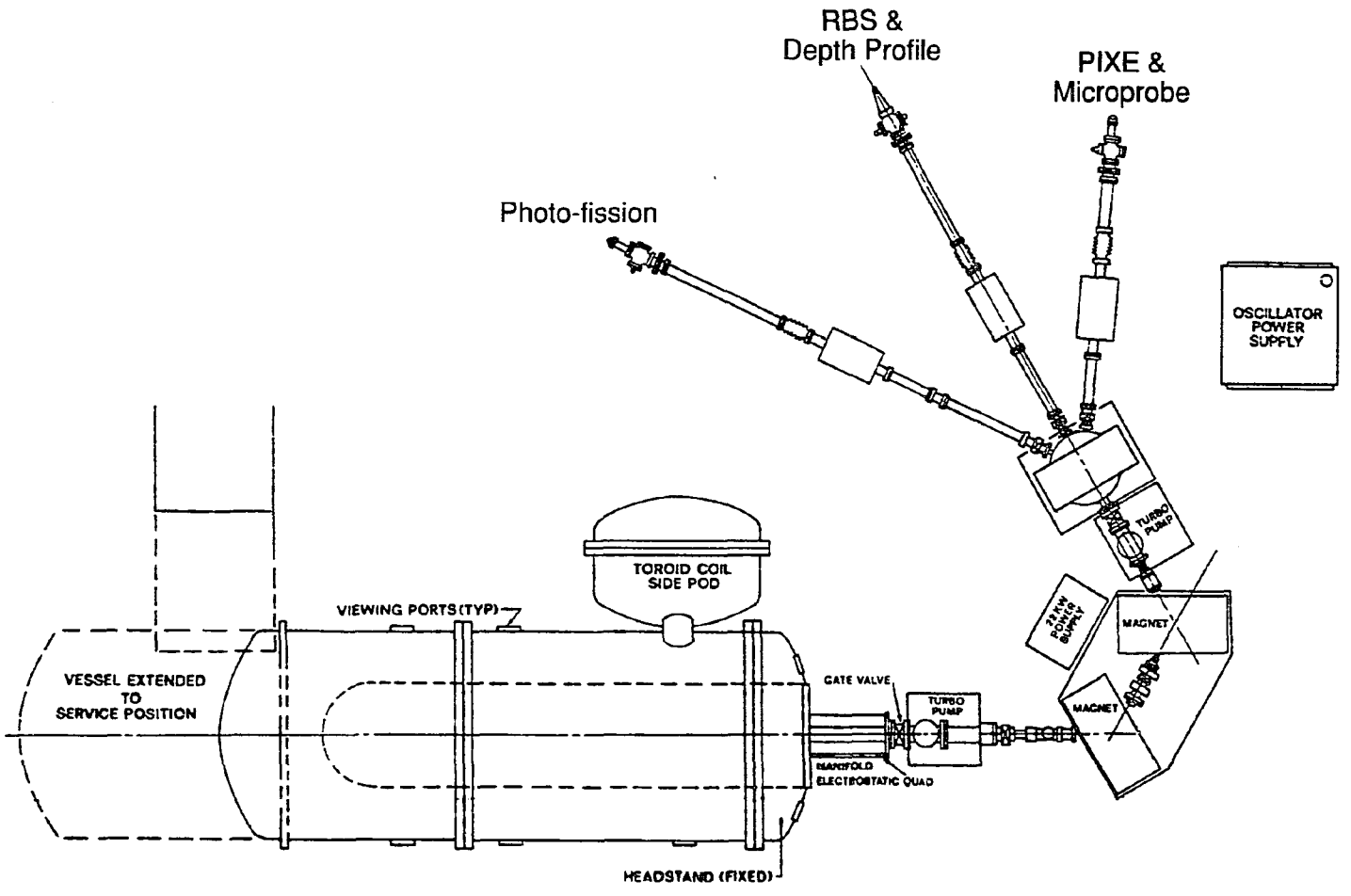

Figure A.4 Schematic diagram of the Brooklyn College 3.75 MeV Dynamitron accelerator (top view).

occurs when the beam passes through a 7 μm thick (13.2 mg/cm^2) tungsten foil placed at a distance of about 35 cm from the target. The scattered beam is then collimated by three 1-cm i.d. graphite apertures each separated by 6-cm-long graphite spaces. The collimated beam enters the target chamber through a 25 μm thick Kapton (polyimide) foil sealed with epoxy to a brass ring, which is sealed on an O-ring at the end of a graphite-lined port mounted on the end of the beam tube. Proton energy loss in the tungsten foil and in the Kapton foil are 0.5 and 0.4 MeV, respectively. The diameter of beam reaching the target was measured to be 1.25 cm FWHM [110].

External beam technique is employed in our laboratory. Helium is used as the ambient atmosphere in the target chamber when the target is irradiated by the proton beam. The advantages of using helium rather than vacuum in the target chamber have been discussed [124]. Figure A.5 is the schematic diagram of the PIXE setup. The target chamber is an aluminum box, 45 cm on a side, containing the sample changer, an ordinary Kodak carousel projector modified by removing the optical parts. The projector can sequentially present up to 80 samples into the beam. The beam exit port protrudes 15 cm into the box so that the Kapton window is 4 cm from the target. The X-rays produced are detected by a Si(Li) detector placed at 135^o from the beam direction. Beam current is collected in a graphite Faraday cup sealed at the open end with 2.5 μm Mylar or Kapton (to present escape of charge) and located 6 cm behind the target. The chamber is fitted with a safety valve which will admit air if the Kapton window were to fail and expose to the chamber to the beam-tube vacuum.

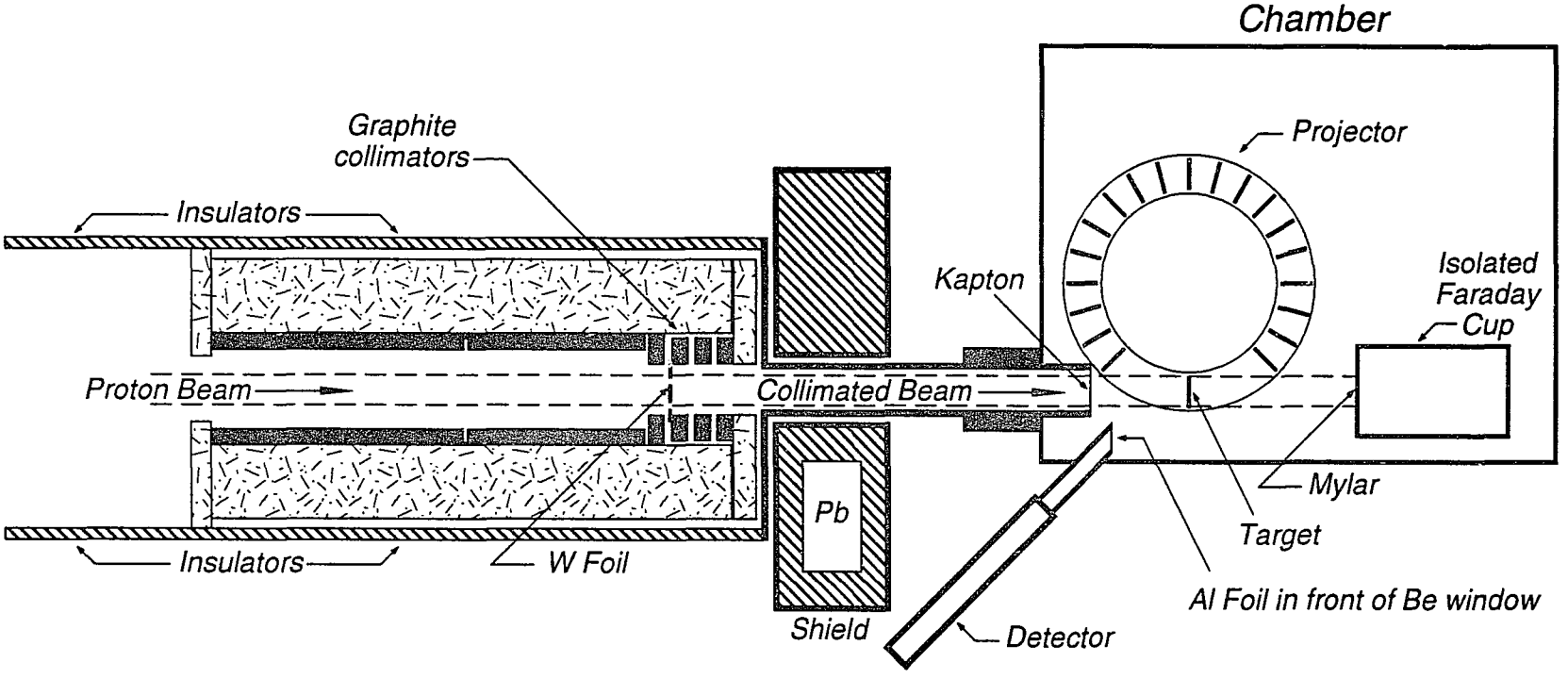

Figure A.5 Top view of our PIXE experimental setup.

A.3.3 X-ray detection and data handling system

Lithium drifted silicon detector (LS-30, Princeton Gamma-Tech) is used for X-ray detection. The detector is cooled to liquid nitrogen temperature to reduce thermal noise and prevent diffusion of lithium through the crystal. The detector actually consists of a silicon crystal with a sensitive region of 6 mm and a diameter of 3 mm, mounted in a cryostat. It has a very high efficiency for X-rays of energies 1.5 keV to 25 keV.

The block diagram of the detection and data handling system is shown in Figure A.6. The X-ray photon is absorbed by the silicon detector through photoelectric effect and loses its energy to the detector, thus producing electron-hole pairs. The charge of the pulse from the detector is integrated by the preamplifier and then converted to a voltage signal proportional to the energy deposited. The voltage signal is processed by the amplifier (Princeton Gamma-Tech) to produce the appropriate shape and amplitude and then converted from an analog to a digital signal by an ADC converter before it enters the multichannel analyzer (MCA). A program functioning as multichannel analyzer is performed in a IBM PC/XT computer.

The function of the pile-up rejecter (PUR) is to eliminate pulse pile-up distortion. If the count rate of X-rays produced is too high, two pulses arrive at essentially the same time at the main amplifier. This results in the formation of a signal pulse the height of which is the sum of the individual pulses. For monoenergetic X-rays this results a "sum peak" in the spectrum at twice the energy of the incident radiation. This problem can be eliminated or reduced by PUR. As shown in Figure A.6, a separate signal from the output of the preamplifier is sent to the pile-up rejecter that inspects the time interval between successive pulses. The pile-up signal is rejected and sent to MCA as long as effective overlap is detected.

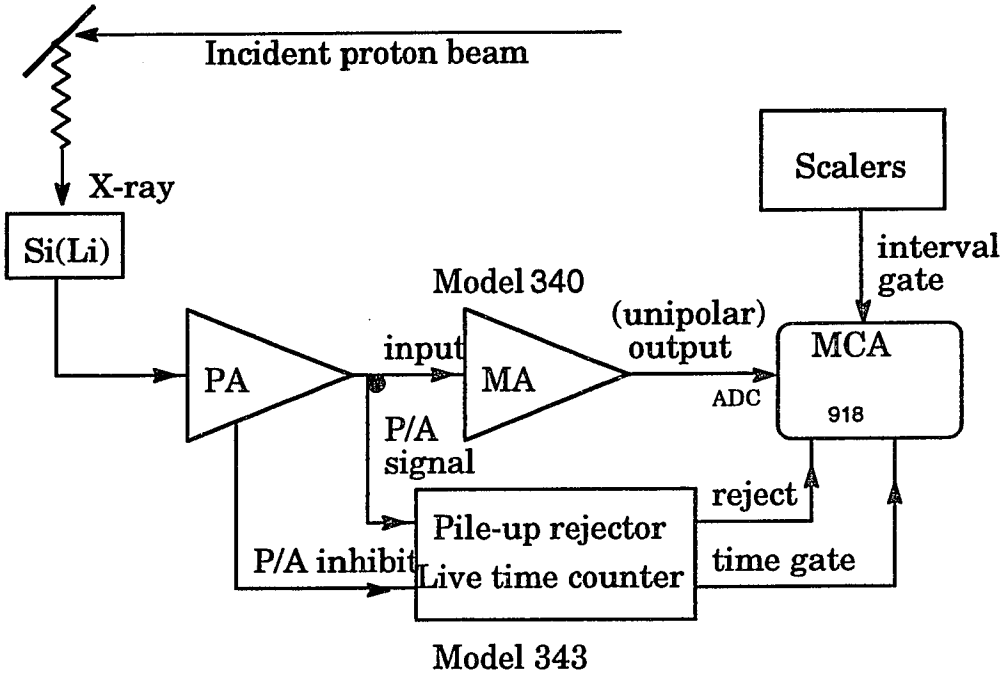

Figure A.6 PIXE detection and data handling system.

(PA) pre-amplifier, (MA) main amplifier, (MCA) multi-channel analyzer.

The entrance of the detector is covered with a 7 mm-diameter and 7 μm-thick beryllium window which allows reasonable efficiency for low energy X-rays. When the incident X-ray is deposited, the X-ray photon creates silicon X-rays which are reabsorbed in the crystal. However, some of Si K X-rays escape from the detector. The signal distorted by escape peak appears as a loss from the full energy peak and reappears in the spectrum as a separate peak of energy equal to incident X-ray energy minus Si K_α X-ray (1.74 keV). The escape probability decreases with increasing energy above Si K-absorption edge (1.838 keV) since the higher energy photons penetrate deeper into the silicon crystal.

A.4 Sample preparation

Following a severe storm in 1988 in which two large Norway maples (*Acer platanoides* L.) on Kings Highway, Brooklyn New York blew down, sections of the trunks were cut and brought back to the laboratory. Multiple core samples were taken around the circumference at two different heights using an increment borer of 4.3 mm in diameter and 40 cm long.

After being dried in a oven at 70 ^{o}C for 24 hours, the cores were sanded with silicon carbide sandpaper of progressively finer grit until the ring structures was clearly revealed. Segments of up to 100 mg were cut from the cores and represented three to four years growth. The wood was placed in 45 ml or 23 ml of Teflon microwave digestion vessel (Parr Instrument Co.) with 1.0 ml of ultrapure HNO_3 (GFE Chemicals) and 50 μl of 1000 ppm Yttrium solution (Aldrich Chemical Company, Inc.) to act as internal standard. The volume of solution was adjusted to 2 ml with double distilled deionized H_2O.

Digestion was achieved by heating in a microwave oven (Sears) for 5 minutes at full power. Only one bomb with sample was heated in the oven each time.

The sample target was prepared as follows. Prior to deposition of the aliquot solution, a piece of 6-μm thick polypropylene film (Somar International Co.) was placed over a brass ring, and then another slightly larger brass ring was pressed so as to stretch the film evenly between the two concentric rings. This assembly was placed on a Teflon apparatus which permits a gentle vacuum to be drawn on the center (0.75 cm circle) of the film. A 200 μl of aliquot from the digested solution was then pipetted to the center of film being subjected to a small vacuum to ensure a circular deposit. The sample was then heated under a 250 W IR lamp. To avoid permanent curvature and softening of the film at the center, the vacuum was removed just before the sample was completely dry. The film was then mounted in a 35-mm slide holder.

Most samples analyzed in our laboratory were thin target samples. The requirements for the supporting film or backing are: 1) very thin to minimize bresstrahlung; 2) strong enough to be handle easily; and 3) very low level of impurity atoms. Our experiments showed that polypropylene is a suitable material for sample backing. However, polypropylene is hydrophobic causing the drop of sample to shrink as it dries and form an unacceptable deposit, thick and with non-uniform crystals. This problem can be solved by treating the film with surfactant before the digested solution is added to it. Many surfactants have been suggested for this purpose [125, 126, 127]. The surfactant we used is Igepol CA-720 (GAF Corp.) whose structure is

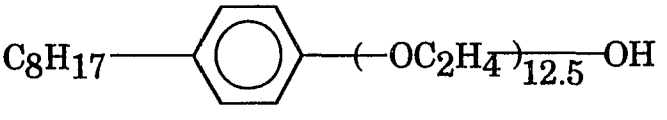

The modified target preparation procedure is that 10 μl of 2% (v/v) CA-720 was added on a polypropylene film and allowed it to dry before digested solution was pipetted to it. A relatively thin and uniform target was obtained by using this method. The PIXE spectrum showed that 10 μl of 2% (v/v) CA-720 only contains trace amount of Cu which can be subtracted from samples as a blank.

To verify accuracy of our PIXE analysis, NIST 1577a (bovine liver) standard was prepared in the following procedure:

Accurately weighed 0.1 g of NIST 1577a, 1.0 ml of ultrapure HNO_3, 0.5 ml of double distilled deionized H_2O, and 50 μl of 1000 ppm Y were added to the Teflon digestion cup. The cup with jacket was placed in microwave oven at full power (650 W) for 1 minute. After the cup was cooled, it was opened to release CO_2 and NO and added 0.5 ml HNO_3. The cup was heated again in the oven at 80% power for 8-9 minutes. The target preparation of the standard was the same as that for the tree samples.

A.5 Standard calibration system

PIXE, unlike other elemental analysis techniques, is a relative rather than absolute type of analysis. Since the ratio of X-ray yield of elements of interest to that of internal elements is constant under certain conditions such as proton energy, the quantitative analysis depends on comparison with the ratios in sample and in the standard. Our previous work [110] showed that the $K_\alpha(Z)/K_\alpha(Y)$ ratios vary as a smooth function with atomic number from Z=14 to 42. So, the calibration process can be greatly simplified. We only need to measure the $K_\alpha(Z)/K_\alpha(Y)$ ratios for some elements. The $K_\alpha(Z)/K_\alpha(Y)$

ratios for other elements can be found from the plot of $K_\alpha(Z)/K_\alpha(Y)$ against atomic number.

The procedure for standard preparation is almost the same as that for sample preparation except that 100 μl of diluted standard solution containing each of 20 ppm Y and selected elements instead of digested solution was pipetted onto the polyethylene film.

The measured ratios of some elements to Y are listed in Table A.1 and the ratios versus atomic number are plotted in Figure A.7.

With the standard calibration curve, we can calculate the concentration of each element in the wood samples according to the following equation:

$$C_Z\ (\text{ppm}) = \frac{I_u(Z)}{I_u(Y)} \times \frac{Ks(Y)}{Ks(Z)} \times \frac{C_u(Y) \times V_u(Y)}{W} \qquad [A.1]$$

where

C_Z is concentration of element with atomic number Z in a sample;

$I_u(Z)$ is the X-ray intensity of element Z in a sample;

$I_u(Y)$ is the X-ray intensity of Yttrium in a sample;

Ks(Z) is the X-ray intensity of element Z in standard;

Ks(Y) is the X-ray intensity of Yttrium in standard, the ratio of Ks(Z) to Ks(Y) can be found in Table A.1;

$V_u(Y)$ and $C_u(Y)$ represent the volume (milliliter) and concentration (μg/ml) of Y added to the digestion cup;

W is the weight of the sample (gram) in digestion cup.

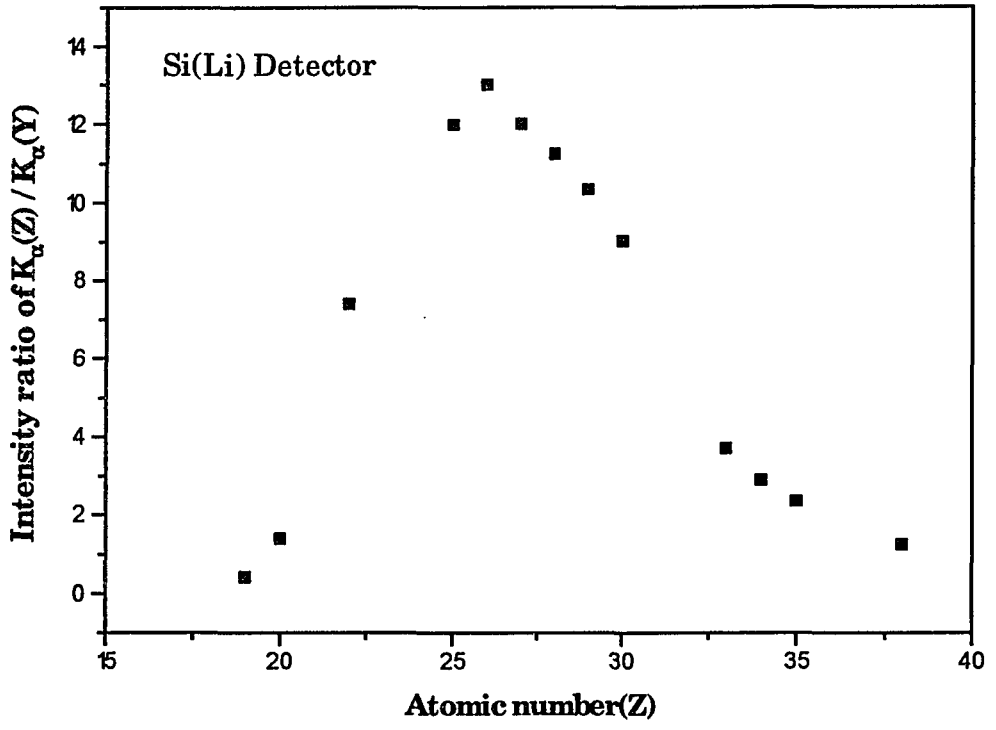

Figure A.7 PIXE standard calibration curve (detector absorber: 50 μm Al foil).

Table A.1 Ratios of $K_\alpha(Z) / K_\alpha(Y)$ or $L_\alpha(Z) / K_\alpha(Y)$ for some elements.

element	K	Ca	Ti	Mn	Fe	Co	Ni
atomic number	19	20	22	25	26	27	28
$K_\alpha(Z) / K_\alpha(Y)$	0.42	1.39	7.39	11.97	13.01	12.2	11.25

element	Cu	Zn	As	Se	Sr	Br	Pb
atomic number	29	30	33	34	35	38	82
$K_\alpha(Z) / K_\alpha(Y)$	10.3	9.03	3.7	2.87	2.33	1.24	
or $L_\alpha(Z)/ K_\alpha(Y)$							0.68

A.6 Sample analysis

Before each analysis, the Si(Li) detector was calibrated with a radioisotope ^{57}Co source. The ^{57}Co source placed approximately 1/4 to 1/2 inch in front of the detector, gives a spectrum showing three peaks at 6.40 (K α of Fe), 7.04 (K_β of Fe), and 14.41 (γ ray) keV, respectively. The peaks of 6.40 and 14.41 keV were used for calibration. The 6.40 keV peak was also used to determine the resolution of the detector. Resolution is stated in terms of electron volts at full-width at half-maximum (FWHM) of Fe K_α peak. The best resolution in our laboratory was 168 eV FWHM at Fe K_α.

The samples were irradiated by 3.3 MeV proton beam with current of 0.8 μA. A total charge of 40 μC was accumulated on each target. The background components and the net areas of all peaks in the X-ray spectra were fitted with a computer program called PCRACE [128].

A.7 Results and discussion

Results of PIXE analysis of NIST 1577a (bovine liver) and wood samples are displayed in Table A.2 and Table A.3 respectively. The concentrations of Mn, Fe, Cu, Zn, and Se obtained by PIXE in our laboratory are within the range of certified values of NIST. The concentrations of K and Ca are lower than the certified values due to the partial overlap of K K_α (3.31 keV) and Ca K_α (3.69 keV) peaks as shown in Figure A.8. The K K_β (3.59 keV) is also superimposed by Ca K_α. Although PCRACE program could subtract the intensity of K K_β from that of Ca K_α, there was still error produced since the three peaks are too close to each other to be separated.

Table A.3 indicates that Pb concentration in tree rings decreased from rings 66-70 to rings 84-88 whose spectra are shown in Figure A.9. This was

what we expected because the unleaded gasoline substituted for the leaded gasoline and thus the concentration in atmosphere declined. Unfortunately, Pb L_{α} peak did not show up in some tree-ring spectra (71-74, 62-65, and 59-61). We could not determine in which annual-growth of ring the maximum Pb concentration appear. Lead in some of these samples was below the detection limit.

In summary, PIXE provides low detection limits and multielemental capacity for trace element analysis in tree rings. Although the sensitivity of most elements is not comparable to ICP-MS, the detection limits of K, Ca, and Fe are lower in PIXE than in ICP-MS. We could have reduced the proton beam to 0.1 mm diameter to increase the sensitivity of PIXE and to analyze samples non-destructively. Unfortunately, the accelerator was shut down because of a major equipment failure plus severe budget cuts so that the experiment was not continued.

Table A.2 PIXE analysis of NIST 1577a, bovine liver.

	our result (ppm)	NIST certified (ppm)
	mean ± s.d. (n=3)	mean ± s.d. [Ref. 129]
K	0.47% ± 0.13%*	0.996%*
Ca	103 ± 10	121 ± 5
Mn	10.0 ± 0.3	9.9 ± 0.4
Fe	168 ± 2	155 ± 17
Cu	162 ± 4	149 ± 14
Zn	122 ± 4	122 ± 4
Se	0.66 ± 0.10	0.78 ± 0.20

* — percentage values

Table A.3 Concentrations (ppm) of some elements found in the tree rings of Norway maple from Brooklyn, New York.

ring section	K	Ca	Ti	Mn	Fe	Ni	Cu	Zn	Pb	Sr
59-61	1642	1999	4.9	8.3	56	489	27	23	BDL	BDL
62-65	1005	1764	2.5	5.6	24	0.7	6.7	10	BDL	6.4
66-70	1228	1564	5.2	5.5	57	2.3	50	43	13	9.9
71-74	498	552	4.9	4.0	35	289	75	31	BDL	BDL
79-83	1302	1840	BDL	5.7	31	BDL	5.1	6.7	11	8.1
84-88	1106	1636	1.5	5.2	27	3.4	7.2	7.8	BDL	5.3

BDL —— below detection limits.

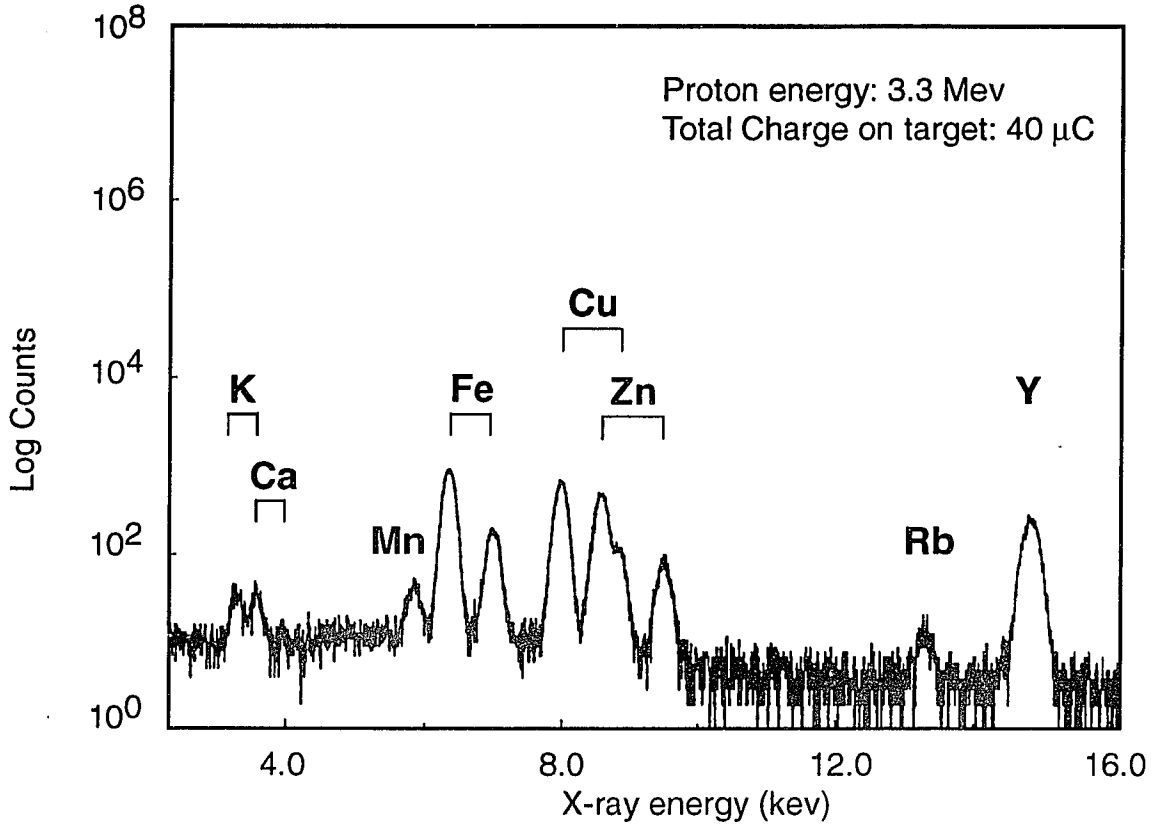

Figure A.8 PIXE spectrum of NIST 1577a, bovine liver

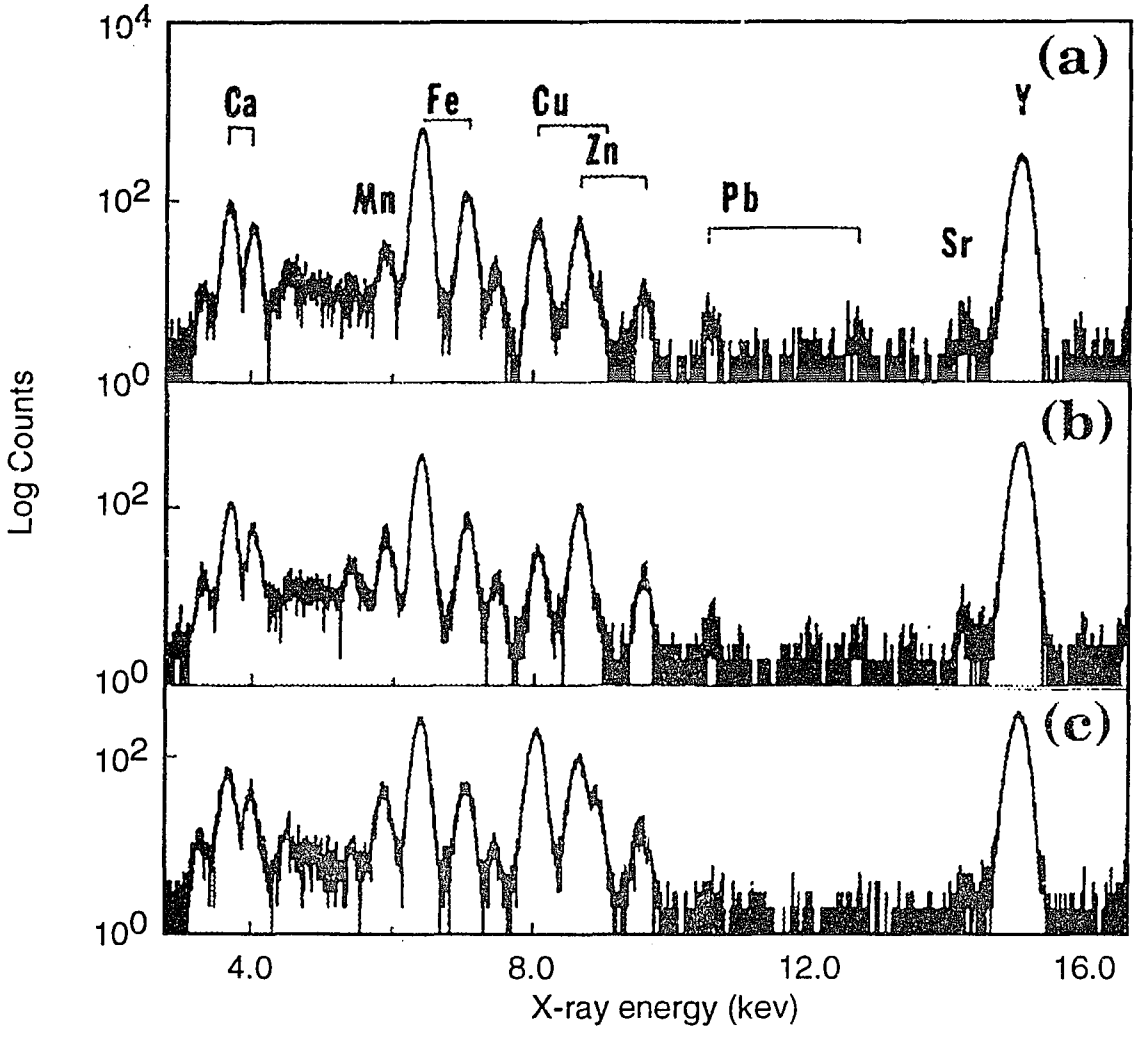

Figure A.9 PIXE Spectra of three segments of a single core taken from a Norway maple tree in Brooklyn (Kings Highway). The Spectra represent annual-growth rings from the periods: 1966-70 (a), Pb easily detected; 1979-83 (b), Pb still detected; and 1984-88 (c), Pb essentially not detected.

References

[1] E. Goldstein, Berl. Ber., 1886, **39**, 691.

[2] W. Wien, Wied. Ann., 1898, **65**, 440.

[3] J. J. Thomson, Phil. Mag., 1912, **24**, 209.

[4] J. J. Thomson, "Rays of Positive Electricity and Their Application to Chemical Analysis" , Longmans, Green and Co., London, 1913.

[5] W. R. Smythe, L. H. Rumbaugh, and S. S. West, Phys. Rev., 1934, **45**, 724.

[6] A. O. Nier, E. T. Booth, J. R. Dunning, and A. V. Groose, Phys. Rev., 1940, **57**, 546.

[7] J. A. Hipple and D. P. Stevenson, Phys. Rev., 1943, **63**, 121.

[8] H. Hoover and H. W. Washburn, Amer. Inst. Mining Metallurgical Engrs. Tech., 1940, Publ. No. **1205**.

[9] A. J. Dempster, Phys. Rev., 1918, **11**, 316.

[10] R. W. Kiser, "Introduction to Mass Spectrometry and Its Applications", Prentice-Hall, Inc. 1965.

[11] W. Paul and H. Steinwedel, Z. Naturforsch., 1953, **8a**, 448.

[12] W. Paul and H. Steinwedel, German Patent, 1956, **944,900**.

[13] G. I. Babat, Vestn. Elektroprom, 1942, **No2**, 1-12, **No3**, 2-8.

[14] G. I. Babat, J. Inst. Elect. Eng., 1947, **94**, 27.

[15] T. B. Reed, J. of Appl. Phys., 1961, **32**, 821.

[16] S. Greenfield, I. Ll. Jones, and C. T. Berry, Analyst, 1964, **89**, 713.

[17] R. H. Wendt and V. A. Fassel, Anal. Chem., 1965, **37**, 920.

[18] G. W. Dickinson and V. A. Fassel, Anal. Chem., 1969, **41**, 1021.

[19] J. L. Jones, R. L. Dahlquist, J. W. Knoll, and R. H. Hoyt, 24 Pittsburgh Conf. Anal. Chem. and Appl. Spectrosc., Abstr. Paper No **147**, 1974.

[20] R. S. Houk, V. A. Fassal, G. D. Flesch, H. J. Svec, A. L. Gray, C. E. Taylor, Anal. Chem., 1980, **52**, 2283.

[21] G. J. O'Halloran, R. A. Fluegge, J. F. Betts, W. L. Everett and L. W. Walker, A. F. Materials Laboratory, ASD-TDR-62-644 parts I and II, 1964.

[22] A. L. Gray, Analyst, 1975, **100**, 289.

[23] A. L. Gray, "Dynamic Mass Spectrometry", 1978, **5**, 106, Heyden, London.

[24] A. L. Gray and A. R. Date, "Dynamic Mass Spectrometry", 1981, **6**, 252, Heyden, London.

[25] A. R. Date and A. L. Gray, Analyst, 1981, **106**, 1255.

[26] A. L. Gray, Spectrochim. Acta, 1985, **40B**, 1525.

[27] D. R. Wiederin, F. G. Smith, and R. S. Houk, Anal. Chem., 1991, **63**, 219.

[28] D. R. Wiederin, R. E. Smyczek, and R. S. Houk, Anal. Chem., 1991, **63**, 1626.

[29] T. L. Brown, H. E. Lemay, Jr. and B. E. Bursten, "Chemistry —— The Central Science" (5th edition), Prentice Hall, 1991.

[30] J. W. Olesik, Anal. Chem., 1991, **63**, 12A.

(31) J. D. Ingle and Jr. S. R. Crouch, "Spectrochemical Analysis", Prentice-Hall Inc., NJ, 1988.

(32) J. F. Alder, R. M. Bombelke, and G. F. Kirkbright, Spectrochem. Acta, 1980, **35B**, 165.

(33) L. de Galan, R. Smith, J, D. Winefordner, Spectrochim. Acta, 1968, **23B**, 521.

(34) A. L. Gray, Spectrochim. Acta, 1986, **41B**, 151.

(35) C. E. Moore, "Ionization Potentials and Ionization Limits Derived from the Analyses of Optical Spectra," NSRDS-NBS 34, National Bureau of Standards, Washington, D.C., 1970.

(36) R. S. Houk, Anal. Chem., 1986, **58**, 97A.

(37) R. W. Kiser, "Introduction to mass spectrometry and its application", Prentice-Hall, Inc., Englewood Cliffs, NJ, 1965.

(38) P. H. Dawson, Mass Spectrom. Rev., 1986, **5**, 1.

(39) D. R. Denison, J. Vac. Sci. Technol., 1971, **8**, 266.

(40) A. R. Date and A. L. Gray, " Applications of Inductively Coupled Plasma Mass Spectrometry", Blackie, Glasgow, 1989.

[41] H. P. Longerich, J. Anal. At. Spectrom., 1989, **4**, 491.

[42] V. A. Fassel and B. R. Bear, Spectrochim. Acta, 1986, **41B**, 1089.

[43] A. L. Gray and A. R. Date, Analyst, 1983, **108**, 1033.

[44] A. L. Gray, Analyst, 1985, **110**, 551.

[45] E. H. and L. Ebdon, J. Anal. At. Spectrom., 1991, **6**, 421.

[46] J. W. H. Lam and G. Horlick, Spectrochim. Acta, 1990, **45B**, 1313.

[47] F. E. Lichte, A. L. Meier and J. G. Crock, Anal. Chem., 1987, **59**, 1150.

[48] N. Doherty and A. Van der Voet, Can. J. Spectr., 1985, **30**, 135.

[49] H. P. Longerich, B. J. Fryer, D. F. Strong and C. J. Kantipuly, Spectrochim. Acta, 1987, **42B**, 75.

[50] N. Jakubowski, I. Feldmann, and D. Stuewer, Spectrochim. Acta, 1992, **47**, 107.

[51] N. Jakubowski, I. Feldmann, and D. Stuewer, and H. Berndt, Spectrochim. Acta, 1992, **47B**, 119.

[52] D. C. Gregoire, J. Anal. At. Spectrom., 1988, **3**, 309.

[53] C. J. Park and G. E. M. Hall, J. Anal. At. Spectrom., 1988, **3**, 355.

[54] R. Tsukahara and M. Kubota, Spectrochim. Acta, 1990, **45B**, 779.

[55] N. Shibata, N. Fudagawa, and M. Kubota, Anal. Chem., 1991, **63**, 636.

[56] F. G. Smith, D. R. Wiederin, and R. S. Houk, Anal. Chem., 1991, **63**, 1458.

[57] E. H. Evans and L. Ebdon, J. Anal. At. Spectrom., 1990, **4**, 299.

[58] J. W. H. Lam and J. W. H. McLaren, J. Anal. At. Spectrom., 1990, **5**, 419.

[59] J. W. McLaren, J. W. H. Lam, and A. Gustarsson, Spectrochim. Acta, 1990, **45B**, 1091.

[60] M. A. Vaughan and G. Horlick, Appl. Spectrosc., 1991, **44**, 587.

[61] A. R. Date and A. L. Gray, "Applications of Inductively Coupled Plasma Mass Spectrometry", Blackie and Sons, 1989.

[62] D. J. Douglas and R. S. Houk, Prog. Anal. At. Spectrosc., 1985, **8**, 1.

[63] G. Houlick, S. H. Tan, M. A. Vaughan, and Y. Shao, "Inductively Coupled Plasmas in Analytical Atomic Spectroscopy", VCH, New York, 1987.

[64] J. A. Olivares and R. S. Houk, Anal. Chem., 1986, **58**, 20.

[65] C. Vandecasteele, M. Nagels, H. Vanhoe, and R. Dams, Anal. Chim. Acta, 1988, **211**, 91.

[66] G. R. Gillson, D. J. Douglas, J. E. Fulford, K. W. Halligan, and S. D. Tanner, Anal. Chem., 1988, **60**, 1472.

[67] M. B. Shabani, T. Akagi, H. Shimizu, and A. Masuda, Anal. Chem., 1990, **62**, 2709.

[68] M. B. Shabani and A. Masuda, Anal. Chem., 1991, **63**, 2099.

[69] M. R. Plantz, J. S. Fritz, F. G. Smith, and R. S. Houk, Anal. Chem., 1989, **61**, 149.

[70] J. J. Thompson and R. S. Houk, Appl. Spectrosc., 1987, **41**, 801.

[71] Y. Igarashi, H. Kawamura, K. Shiraishi, and Y. Takaku, J. Anal. At. Spectr., 1989, **4**, 571.

[72] M. Viczian, A. Lasztity, X. Wang, and R. M. Barnes, J. Anal. At. Spectr., 1990, **5**, 125.

[73] J. R. Dean, L. Ebdon, and R. J. Massey, J. Anal. At. Spectr., 1987, **2**, 369.

[74] J. J. Thompson, Proceedings of First National Conference on ICP-MS, Sept. 19-20, 1992, Philadelphia, Pennsylvania.

[75] K. E. Jarvis, A. L. Gray and R. S. Houk, "Handbook of Inductively Coupled Plasma Mass Spectrometry", Chapman and Hall, New York, 1992.

[76] R. J. Raison, P. K. Khanna, and P. V. Woods, Can. J. For. Res., 1985, **15**, 132.

[77] C. T. Dyrness, K. Van Cleve, and J. D. Levison, Can. J. For. Res., 1989, **19**, 1389.

[78] A. M. O'Connell, T. S. Grove, and D. Lamb, CSIRO, 1981, 277.

[79] G. S. Hall and M. Naumann, J. Radioanal. Nucl. Chem. Letters., 1984, **87**, 317.

[80] T. W. Swetnam, Forest Sci., 1984, **30**, 238.

[81] K. E. Jarvis, " Plasma Source Mass Spectrometry ", Royal Society of Chemistry, 1990.

[82] G. S. Hall, D. K. Yamaguchi, and T. M. Rettberg, J. Radioanal. Nucl. Chem. Letters, 1990, **146**, 255.

[83] A. C. Caprio, C. M. Baisan, P. M. Brown, and T. W. Swetnam, "Fire Scar Dates From Bandelier National Monument, New Mexico — Final Report to Bandelier National Monument", Laboratory of Tree-Ring Researsh, University of Arizona, September 30, 1988.

[84] J. J. Chisolm Jr., and D. M. O'Hara, "Lead Absorption in Children", Urban & Schwarzenberg, Baltimore, 1982.

[85] K. R. Mahaffey, "The Biochemistry of Lead in the Environment", Elsevier / North-Holland, Biomedical Press, New York, 1978.

[86] Associated Press, Atlanta, December 7, 1992 quoted by World Journal (Chinese), December 8, 1992.

[87] R. M. Harrison and D. P. H. Laxen, Nature, 1980, **286**(21), 791.

[88] H. H. Birden Jr., E. J. Calabrese, and A. Stoddard, J. Am. Water Works Assoc. (JAWWA), Nov. **66**, 1985.

[89] M. M. Frey, "The American Water Works Association Lead Information Survey: A Final Report", JAWWA, Sept. **64**, 1989.

[90] A. Goldberg, Envir. Health Persp., 1974, **7**, 103.

[91] M. R. Schock and Ch. H. Neff, JAWWA, Nov. **47**, 1988.

[92] J. C. McKinley Jr., New York Times, Sept. 15, 1992.

[93] N. M. Ram, E. J. Calabrese, and R. F. Christman, "Organic Carcinogens in Drinking Water", John Wiley and Sons, 1986.

[94] R. M. Thurman, R. L. Wershaw, R. L. Malcolm, and D. J. Pinckney, Organic Geochem., 1982, **4**, 27.

[95] J. A. Rutherford, R. F. Mathis, B. R. Turner, and D. A. Vroom, J. Chem. Phys., 1977, **56**(No. 9), 4654.

[96] A. Goldwasser and J. M. Mermet, Spectrochim. Acta, 1986, **41B** (No. 7), 725.

[97] K. P. Huber and G. Herzberg, "Molecular Spectra and Molecular Structure --- IV. Constants of Diatomic Molecules", Van Nostrand Reinhold Company, 1979.

[98] R. F. Bacher and S. Goudsmit, "Atomic Energy States", (1st. ed.) McGraw-Hill Book Company, Inc., 1932.

[99] G. Faure, "Principles of Isotope Geology" (second edition), John Wiley & Sons, 1977.

[100] J. O. Nriagu, Sci. Tot. Environ., 1990, **92**, 13.

[101] S. P. Nickerson, J. Chem. Educ., 1954, **31**, 560.

[102] U. S. Environmental Protection Agency, Air Quality Criteria for Lead, Environmental Criteria and Assessment Office, Research Triangle Park, NC, 1986.

[103] J. L. Annest, New Engl. J. Med., 1983, **308**, 1373.

[104] T. J. Chow, C. B. Snyder, and J. L. Earl, "Isotope ratios of lead as pollutant source indicators", Proceedings of symposium on isotope ratios as pollutant source and behaviors indicators, Vienna, November 18-22, 1974.

[105] W. T. Sturges and L. A. Barrie, Nature, 1987, **329**, 144.

[106] Y. Erel, C. C. Patterson, M. J. Scott, and J. J. Morgan, Chem. Geol., 1990, **85**, 383.

[107] C. F. Baes III and S. B. McLaughlin, "Multielemental analysis of tree rings: A survey of coniferous trees in the Great Smoky Mountains National Park", Oak Ridge National Laboratory, ORNL-6155.

[108] E. F. Neuhauser and R. Hartenstein, J. Environ. Qual., 1980, **9**(1), 21.

[109] S. Bayer, J. A. McHard, and J. D. Winefordner, J. Agric. Food Chem., 1980, **28**, 1306.

[110] G. Cadet, Ph. D. Thesis, CUNY, 1987.

[111] J. Gilbert, M. J. Shepherd, M. A. Wallword, and R. G. Harris, J. Apic. Res., 1981, **20**, 125.

[112] W. O. Kwan, B. R. Kowalski, and R. K. Skogerboe, J. Agric. Food Chem., 1979, **27**, 1321.

[113] I. Frank and B. R. Kowalski, Anal. Chim. Acta, 1984, **162**, 241.

[114] A. Kabata-Pendias and H. Pendias, "Trace Elements in soils and Plants", CRC Press, Boca Raton, 1984, 51-55.

[115] R. Moseley, Phil. Mag., 1913, **26**, 1024.

[116] W. Bambynek *et al.*, Revs. Mod. Phys., 1972, **44**, 716.

[117] S. A. E. Johansson, Nucl. Instr. and Meth., 1984, **B3**, 1.

[118] G. S. Hall and M. Naumann, J. Radioanal. Nucl. Chem. Letters, 1984, **87**(5), 317.

[119] V. Valkovic, D. Rendic, E. K. Biegert, and E. Andrade, Environment International, 1979, **2**, 27.

[120] M. Nagj, J, Injuk, and V. Valkovic, Nucl. Instr. and Meth., 1987, **B22**, 465.

[121] S. Monaro and R. Lecomte, Int. J. Nucl. Medicine, 1981, **8**, 1.

[122] G. Basbas, W. Brandt, and R. Laubert, Phys. Rev., 1973, **A7**, 579.

[123] J. D. Garcia, Phys. Rev., 1970, **A1**, 280.

[124] S. E. Bauman, E. T. Williams, H. L. Finston, A. H. Bond, and P. M. S. Lesser, Nucl. Instr. and Meth., 1979, **165**, 57.

[125] G. Robaye, *et al.*, Nucl. Instr. and Meth., 1980, **172**, 533.

[126] S. A. E. Johansson and T. B. Johansson, Nucl. Instr. and Meth., 1976, **137**, 473.

[127] N. F. Mangelson, Nucl. Instr. and Meth., 1977, **142**, 133.

[128] S. H. Greenberg, E. T. Williams, B. Perley, and R. Eldred, and D. J. Shadoan, Nucl. Instr. and Meth., 1987, **B24/25**, 625.

[129] E. S. Gladney, B. T. O'Malley, I. Roelandts, and T. E. Gills, NBS Special Publication **260-111**, US Department of Commerce, National Institute of Standards and Technology, 1987.